STUDY OF LI-MG ALLOY AND SI POWDER ANODES FOR LI-ION BATTERIES: EXPERIMENTS, NEUTRON IMAGING AND MODELING

by

Yuxuan Zhang

A dissertation submitted to the faculty of
The University of Utah
in partial fulfillment of the requirements for the degree of

Doctor of Philosophy

Department of Metallurgical Engineering

The University of Utah

December 2016

The University of Utah Graduate School

STATEMENT OF DISSERTATION APPROVAL

The dissertation of Yuxuan Zhang

has been approved by the following supervisory committee members:

Ravi Chandran	, Chair	06/14/2016 Date Approved
Michael L. Free	, Member	06/15/2016 Date Approved
Anil Virkar	, Member	06/13/2016 Date Approved
Manoranjan Misra	, Member	06/14/2016 Date Approved
Hassina Z. Bilheux	, Member	04/21/2016 Date Approved

and by Manoranjan Misra , Chair/Dean of

the Department of Metallurgical Engineering

and by David B. Kieda, Dean of The Graduate School.

ABSTRACT

This dissertation can be divided into three parts: (1) the study of delithiation process of Li-Mg alloy as anode for Li-ion batteries by both experiments and theoretical modeling, (2) the investigation of the feasibility to study Li spatial distribution after different rates of charge/discharge, and (3) the preparation and electrochemical testing of Si powder anodes for high capacity Li-ion batteries.

In the first part of this work, Li-Mg alloys with two nominal compositions, Mg-50 wt.% Li and Mg-70 wt.% Li were synthesized by direct alloying. These obtained alloys are rolled, annealed and punched into electrodes for electrochemical delithiation. Neutron tomography is used to determine the concentration profiles inside the alloys with different extents of Li depletion. An analytical model to quantify such diffusion-controlled delithiation, accompanied with $\beta \rightarrow \alpha$ phase transition, $\alpha+\beta$ phase boundary movement and volume change, has been developed. The analytical scheme successfully predicted the Li concentration profiles which agreed well with the neutron tomographic data.

In the second part, neutron tomography is again used to investigate the Li spatial response under different charge/discharge rates inside the V_2O_5 cathode. The Li concentration trends observed are in agreement with the established diffusion theory. The capability of using neutron tomography to spatially investigate the Li behavior under different c-rates, has been demonstrated.

In the third part, nanosized Si powder electrodes prepared by simple slurry-casting method are obtained and characterized. Si electrodes with mass loading of 0.76 g/cm^2 showed high initial capacity ~2500 mAh/g and reversible lithiation/delithiation capacities greater than 1300 mAh/g even after 40 cycles, which is higher than the reported values in the literature for Si anodes with similar structure. The preparation approach used here is more economical compared to other nanofabrication methods. Additionally, an in-situ electrochemical cell has been designed and fabricated for neutron diffraction study of Si phase evolutions upon lithiation/delithiation.

TABLE OF CONTENTS

LIST OF TABLES

ACKNOWLEDGMENTS

I would like to express my most sincere gratitude to Prof. Ravi Chandran for providing me this opportunity to pursue my Ph.D. under his guidance. The numerous discussions we had over the course of my Ph.D. not only enabled me to better understand the fundamentals of electrochemistry and neutron scattering, but also contributed to shaping my scientific outlook.

I would like to acknowledge my supervisory committee, Dr. Hassina Bilheux, Prof. Anil Virkar, Prof. Michael Free and Prof. Manoranjan Misra for their valuable help and suggestions.

I would also like to thank Dr. Jean Bilheux, Dr. Kathrine Page, Dr. Louis Santodonato and Dr. Joan Siewenie for their help at national laboratories in both the measurements and the data analysis.

Special thanks to my colleagues: Dr. Madhusudan Jaggnathan, Bhaskar Vadlamani, Fei Cao, Pankaj Kumar, Jun Du for helping me out in the laboratory. This acknowledgment would not be complete without thanking Sara Wilson, Kay Argyle, Brenda Wicks and Evelyn Wells for their help with the administrative affairs in the department. I am also grateful to the DOE-Office of Basic Energy Sciences for providing the financial support for this work. Last but not the least, I am thankful to my family for their blessings and support.

CHAPTER 1

INTRODUCTION

1.1 Background

The quest for the ideal energy storage devices has intensified due to the increasing demand and the rapid development in portable electronics, electric vehicles and aerospace applications. In order to meet the needs in these applications, energy storage devices with higher operational potential, higher gravimetric and/or volumetric capacity, better cyclability and fewer safety issues are highly desired. Li-ion battery technology, which was first successfully marketed by Sony Corporation in 1991 [1, 2], is one of the most promising candidates in this field. It has drawn a lot of attention during these decades because of its high gravimetric and volumetric capacities compared to Ni-Cd and Ni-MH batteries [3], and the most negative potential of Li/Li^+ redox reaction (-3.04V vs. normal hydrogen electrode) among all possible anode materials [4].

For a secondary Li-ion battery, the choice of the material for either anode or cathode affects the overall electrochemical performance such as reversible capacity, cell potential, cycle life, charge/discharge rates, etc. This is mostly because of the different intercalation/storage mechanisms involved for certain materials and the difference in both thermodynamic and kinetic properties. Currently, the most widely used cathode material is $LiCoO_2$. Such transition metal-oxide electrodes have layered rocksalt structure and allow two-dimensional Li-ion motions in the octahedral sites of the oxides [5]. For the anode, graphite is commonly used because of the electrochemical reversibility of lithiation/delithiation process and the kinetic advantage offered by the layered structure [6]. This combination can provide very good electrochemical performance as an energy storage device in most cases. However, the reversible capacity is limited to ~140 mAh/g when the $LiCoO_2$ cathode is cycled between 3 and 4.2 V vs. Li/Li^+ [7].

1.2 Alloy Anode for Li-ion Battery

It is well known that pure metallic lithium is considered as a very promising anode material because of light weight, high theoretical specific capacity and the most negative electrode potential. But the safety issue caused by dendrite formation during charge/discharge greatly limits its application.

Recently, Li based alloy anodes have drawn a lot of attention in the field of Li-ion batteries because of the much higher theoretical capacity than traditional materials. Several metals are reported that can form intermetallic compounds or amorphous phases with Li, and they can be considered as possible anode materials. Metals such as Si, Sb, Sn, Al and Mg are some of the promising candidates because of abundance and low cost [8].

Li-Si anode has the highest theoretical capacity (4200 mAh/g when lithiated to $Li_{4.4}Si$) among these metals, but the cycling performance is poor due to volume expansion ($Li_{4.4}Si$: 323%) caused by Li insertion [9]. This volume expansion can lead to capacity loss and cell failure by the cracking of active material, new solid electrolyte interface (SEI) formation and delamination from the current collector. To alleviate such large volume change, various anode architectures, including thin film, amorphous/crystalline powders, nanorods and nanowires have been intensively evaluated in attempts to achieve better electrochemical performance.

Although considerable research has been performed to improve Si anode by nanostructuring, the preparation approaches are relatively expensive and cannot be extended to large scale production. Also, a clear understanding of the phase transitions associated with distinct electrochemical signatures in Si has not been obtained. Specifically, it is suspected that the increased performance as the size decreases from micron to

nanoscale regime is related to the peculiar structural changes and the proportion of crystalline/amorphous phases upon lithiation. An irreversible crystalline Si to amorphous phase transition is suspected to occur during the first lithiation cycle. It has been found that the crystalline Si gets amorphized along with Li insertion, and the resulting amorphous phase fails to be converted back to crystalline Si by the following delithiation [10]. However, it is unclear how such phase transition occurs and how Li diffuses and intercalates during the amorphization process.

Another promising alloy electrode is Li-Mg alloy. Although there is some volume change (~85% [11]), it is not as large as that in the lithiation of Si or Sn. The theoretical capacity is still high enough (3350 mAh/g for Li_3Mg) to meet various industrial demands while comparing with the most commonly used graphite electrode (375 mAh/g) [8]. Thus a high capacity cell is very likely to be designed and fabricated with the Li-Mg alloy as anode material. The high capacity of Li-Mg alloy is benefited from the large solid solution range of Li in Mg from 11 to 100 wt.% (30-100 at.%). This also enables such an alloy to cycle over a wide range of composition (about 70 at.% change in Li content) with no phase transformation [12]. Also the good ductility of Li-Mg alloy will prevent it from cracking during moderate volume expansion. However, because of the high reactivity of both Li and Mg, a homogeneous Li-Mg alloy is difficult to make, and the mechanisms of lithiation/delithiation of the Li-Mg solid-solution have not been intensively investigated before in the context of Li-ion batteries.

1.3 Research Objectivities

(1) To synthesize Li-Mg binary alloys with specific compositions, and to prepare electrodes by rolling and annealing. Using an electrochemical approach, samples with

different levels of delithiation will be achieved. Experimental Li concentration profile within bulk Li-Mg will be then obtained using computed neutron tomography at CG-1D, Oak Ridge National Laboratory.

(2) To develop a mathematical modeling framework to predict Li concentration profile in the bulk of Li-Mg alloy electrode and to evaluate the nature of phase transition and electrode thickness reduction. The objective is to see if the state of the electrode, after a certain amount of delithiation can be mathematically predicted, using analytical modeling of Li diffusion.

(3) To investigate the feasibility of studying the Li spatial distribution under different charge/discharge rates by neutron computed tomography.

(4) To prepare Si nanopowder by ball milling, and to fabricate Si anode with different particle sizes and different mass loadings on an electrochemically modified current collector. Electrochemical performance, upon lithiation and delithiation, to be assessed.

(5) To design an in situ electrochemical cell for neutron diffraction study of phase transitions of Si anode upon Li insertion/extraction. This enables future detailed study of the unclear local ordering crystalline/amorphous phase transition using various neutron diffraction techniques.

1.4 References

[1] K. Sekai, H. Azuma, A. Omaru, S. Fujita, H. Imoto, T. Endo, K. Yamaura, Y. Nishi, S. Mashiko, M. Yokogawa, Journal of Power Sources, 43 (1993) 241-244.

[2] T. Osaka, M. Datta, Energy Storage Systems in Electronics, CRC Press, 2000.

[3] M. Park, X. Zhang, M. Chung, G.B. Less, A.M. Sastry, Journal of Power Sources, 195 (2010) 7904-7929.

[4] J.M. Tarascon, M. Armand, Nature, 414 (2001) 359-367.

[5] K. Mizushima, P.C. Jones, P.J. Wiseman, J.B. Goodenough, Materials Research Bulletin, 15 (1980) 783-789.

[6] R. Yazami, P. Touzain, Journal of Power Sources, 9 (1983) 365-371.

[7] H. Xia, L. Lu, Y. Meng, G. Ceder, Journal of the Electrochemical Society, 154 (2007) A337-A342.

[8] W.-J. Zhang, Journal of Power Sources, 196 (2011) 13-24.

[9] C. Wang, A. John Appleby, F.E. Little, Journal of Power Sources, 93 (2001) 174-185.

[10] J. Li, J.R. Dahn, Journal of the Electrochemical Society, 154 (2007) A156.

[11] M. Jagannathan, K.S.R. Chandran, Journal of the Electrochemical Society, 160 (2013) A1922-A1926.

[12] A.A. Nayeb-Hashemi, J.B. Clark, A.D. Pelton, Bulletin of Alloy Phase Diagrams, 5 (1984) 365-374.

CHAPTER 2

LITERATURE REVIEW

2.1 Working Principle of Lithium-ion Batteries

A typical Li-ion battery is composed of separator to prevent short circuiting, cathode, anode and ion conducting electrolyte. Figure 2.1 is a schematic drawing to show the working principle of a Li-ion cell with two most commonly used electrode, a graphite anode and a $LiCoO_2$ cathode. It is important to note that, by definition, the negative electrode (graphite) becomes the anode during discharge and cathode during charge. However, by convention, the negative electrode is usually referred to as the anode for convenience.

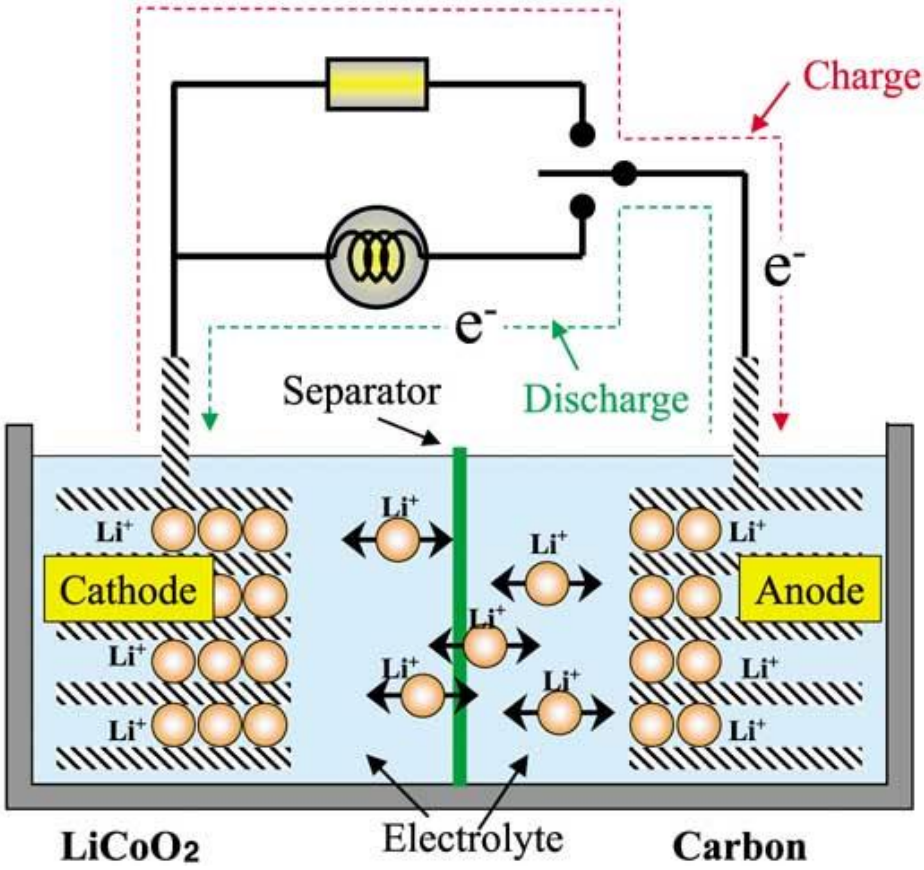

Figure 2.1 Schematic of the principle of LIB. Reprinted with permission from Y. Nishi, The development of lithium ion secondary batteries, The Chemical Record, 1 (2001) 406-413 [1]. Copyright 2001 John Wiley & Sons, Inc.

In Figure 2.1, during the charge cycle of the cell, Li^+ dissociates from $LiCoO_2$ and $Li_{0.5}CoO_2$ is left at the cathode. Li^+ transports through the ion conducting electrolyte to the anode and intercalates with graphite to form LiC_6 compound. These two reactions are reversible during the followed discharge cycle. This drawing in Figure 2.1 also demonstrates how the Li^+ transports from the layer-structured graphene of graphite anode to the layered $LiCoO_2$ cathode via the Li^+ ion-conducting electrolyte during discharge, and, in the opposite direction during charge [1]. It can be noted that how fast the Li^+ inserted and extracted reversibly determines the charge/discharge rates of the whole cell.

2.2 Anodes in Li-ion Batteries

2.2.1 Metallic Li Anodes

Metallic Li anode is a very promising anode material because of its high theoretical specific capacity (3862 mAh/g), the lightest weight of a metal and the most negative electrode potential (-3.04V vs. NHE) [2, 3]. However the dendritic formation of Li (see Figure 2.2) during the Li plating leads to some major safety issues [4, 5]. Most commercial applications require relatively high current rates, which will increase the possibility of the growth of Li dendrite. As these dendrites accumulate, the separator sandwiched between anode and cathode could be penetrated. This will lead to the short circuiting of the cell and a consequent explosion hazard [6]. In practical applications, fires due to the overcharging of Li-ion batteries have been reported [7, 8].

In addition to the above concerns, Li tends to react with electrolyte due to its high reactivity. For instance, for an electrolyte consisting of $LiPF_6$ salt in a solution of ethylene carbonate and dimethyl carbonate, the compounds formed include $LiCH_2CH_2OCO_2Li$, LiOH, Li_2O, Li_2CO_3, LiF, CH_3OCO_2Li, CH_3OLi, etc. [9]. Such reactions consume Li to

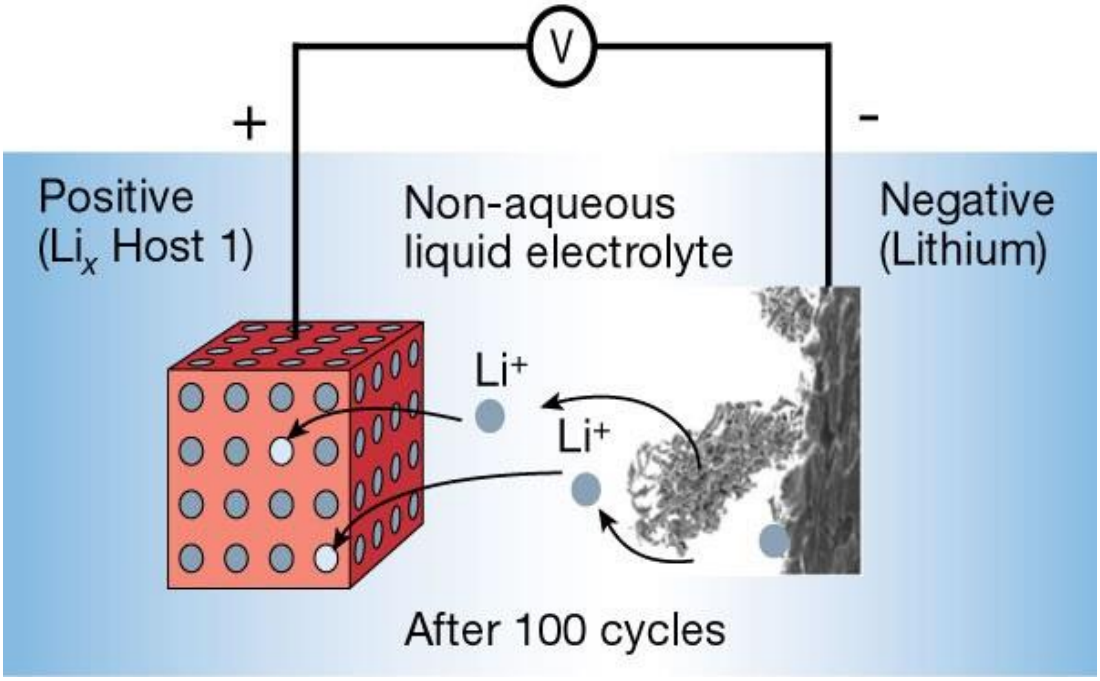

Figure 2.2 Dendrite formation at the Li surface during cycling. Reprinted with permission from J.M. Tarascon and M. Armand, Issues and challenges facing rechargeable lithium batteries, Nature 414(6861), 359, 2001 [5]. Copyright 2001 Macmillan Publishers Ltd.

form a solid electrolyte interface (SEI) layer. This can further impede the charge transfer and create a barrier for the following lithiation and delithiation processes [4, 9, 10]. Due to the reasons mentioned above, Li based alloys, on the other hand, are considered to be better alternatives.

2.2.2 Li-Mg Alloy Anodes

Li can form an intermetallic compound with most other metals, but the high degree of ionic bonding makes the compounds brittle [11, 12]. However, Li-Mg binary alloy is a stable solid solution with good ductility. Also, the reduced reactivity and large solid solution range at room temperature make the Li-rich Li-Mg alloy electrode a promising anode for Li-ion batteries [13].

In the Li-Mg system, the comparable radii of Li and Mg lead to the extended solubility at room temperature. The metallurgical phase diagram of the Li-Mg system is shown in Figure 2.3. It can be seen from the phase diagram that the Li-rich BCC β-phase is stable within the Li composition range between 11.5 wt.% to 100 wt.%. The Li-lean HCP α-phase is stable in the range from 0 wt.% to 5 wt.%. The volume change for insertion of 1 mole of Mg is estimated to be ~80% [14]. This is much less than the corresponding volume changes of Li-Sn (358%) and Li-Si alloy (323%) [15, 16].

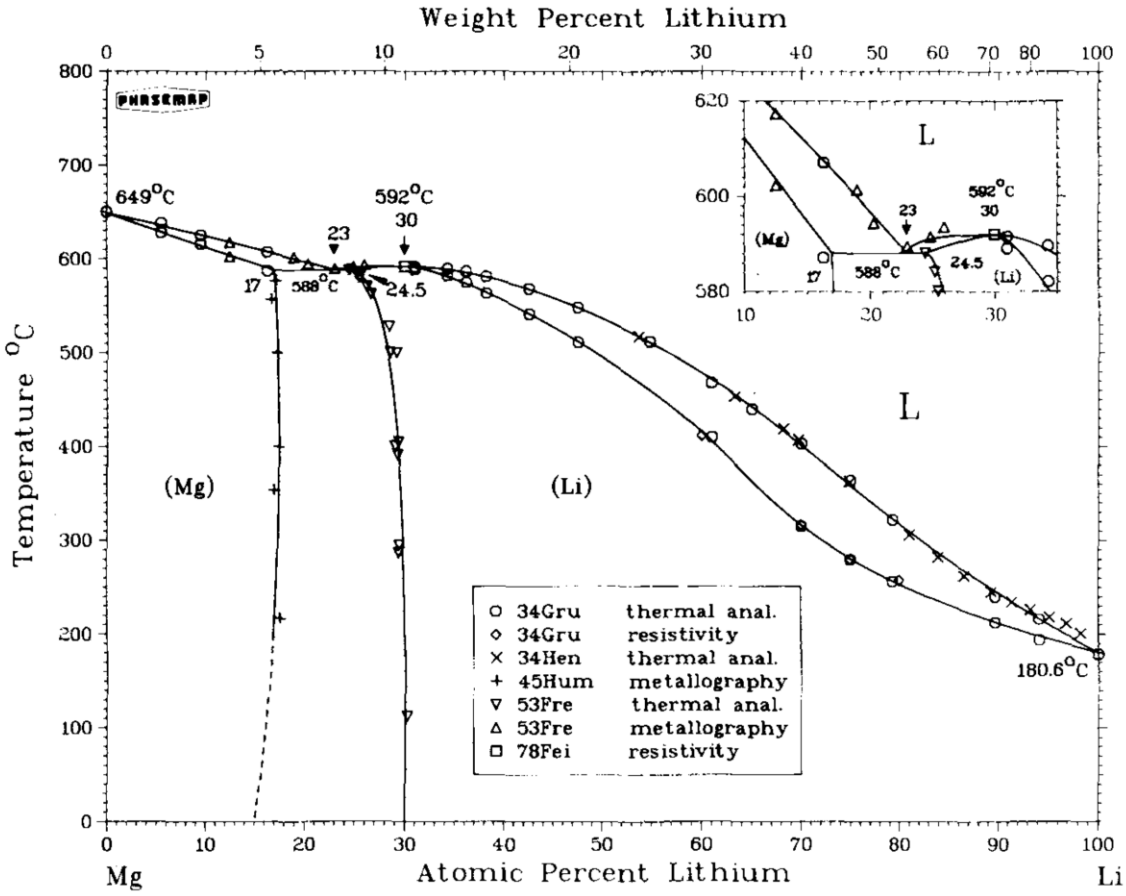

Figure 2.3 Li-Mg metallurgical phase diagram. Reprinted with permission from A.A. Nayeb-Hashemi, J.B. Clark, A.D. Pelton, The Li-Mg (Lithium-Magnesium) system, Bulletin of Alloy Phase Diagrams, 5 (1984) 365-374 [17]. Copyright 1984, Springer-Verlag.

The possibility of electrochemical Li-Mg alloy synthesis has been reported by Dey [18] and Nicholson [19]. The equilibrium alloying potential for the reactions of

$$x\mathrm{Li} + \mathrm{M} = \mathrm{Li}_x\mathrm{M} \tag{2.1}$$

can be calculated using the Nernst equation:

$$E = -\frac{\Delta G_\mathrm{f}}{nF} \tag{2.2}$$

where ΔG_f is the free energy change of formation of $\mathrm{Li}_x\mathrm{M}$, n is the number of electron transferred and F is the Faraday's constant.

The alloying of Li in Mg occurs at 0.03-0.05 V and dealloying occurs at 0.2-0.4 V with respect to $\mathrm{Li}^+/\mathrm{Li}$ [18, 20]. Thus the cell potential offered by using Li-Mg alloy is comparable to what metallic Li offers.

The diffusivity of Li^+ ion in β-phase Li-Mg, prepared by vapor deposition, has been determined with the Cottrell equation

$$I(t) = zFS(C^*_\mathrm{Li} - C_\mathrm{Li})\sqrt{\frac{D_\mathrm{Li}}{\pi t}} \tag{2.3}$$

where z is the charge number (1 for Li), F is the Faraday's constant, S is the surface area of the alloy electrode, D_Li is the diffusion coefficient of Li in the electrode, C_Li is the lithium concentration at the surface of the Li-Mg alloy electrode, and the C^*_Li is the initial uniform lithium concentration in the alloy.

The diffusion coefficient was determined to be ~10^{-8} cm^2/s by extrapolating the slope of I versus $t^{-1/2}$ plot as shown in Figure 2.4 [20, 21]. It is also reported that the diffusivity of Li in HCP α-phase is several magnitudes lower than in the β-phase [22].

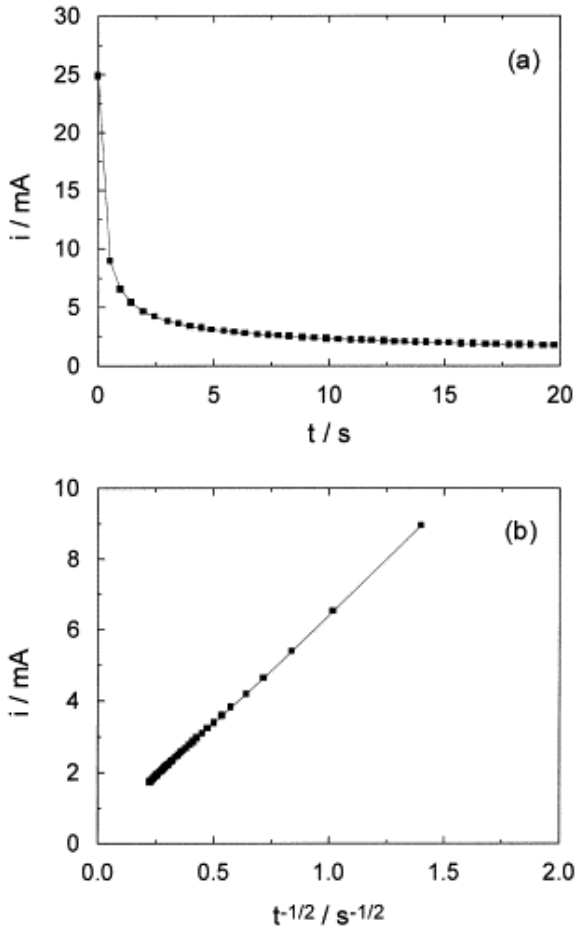

Figure 2.4 Chronoamperometry of Li_6Mg_4 alloy. (a) A typical chronoamperogram of an alloy electrode in 1 M $LiN(CF_3SO_2)_2$–EC/DMC (1:2 by vol.). The potential was stepped from OCV=0.026 to 0.65 V (vs. Li^+/Li), and kept at 0.65 V for 20 s; (b) Cottrell relationship, $I \sim t^{-1/2}$, based on the data shown in (a). Reprinted with permission from Z. Shi, Journal of Power Sources, 92 (2001) 70-80 [20], Copyright 2001, Elsevier.

For Li-Mg alloy, some degree of reversibility, which is highly encouraging, has been demonstrated in the recent work by Jagannathan et al. [14]. In their work, gradual β→α phase transition at the surface of Li-Mg electrodes, during delithiation, was observed using X-ray diffraction. This result shown in Figure 2.5 suggests that, during continuous Li depletion, the BCC β-phase gradually transforms into HCP α-phase at the surface of the electrode. This may hinder the further transport of from the bulk to the electrode/electrolyte interface, where the reaction takes place.

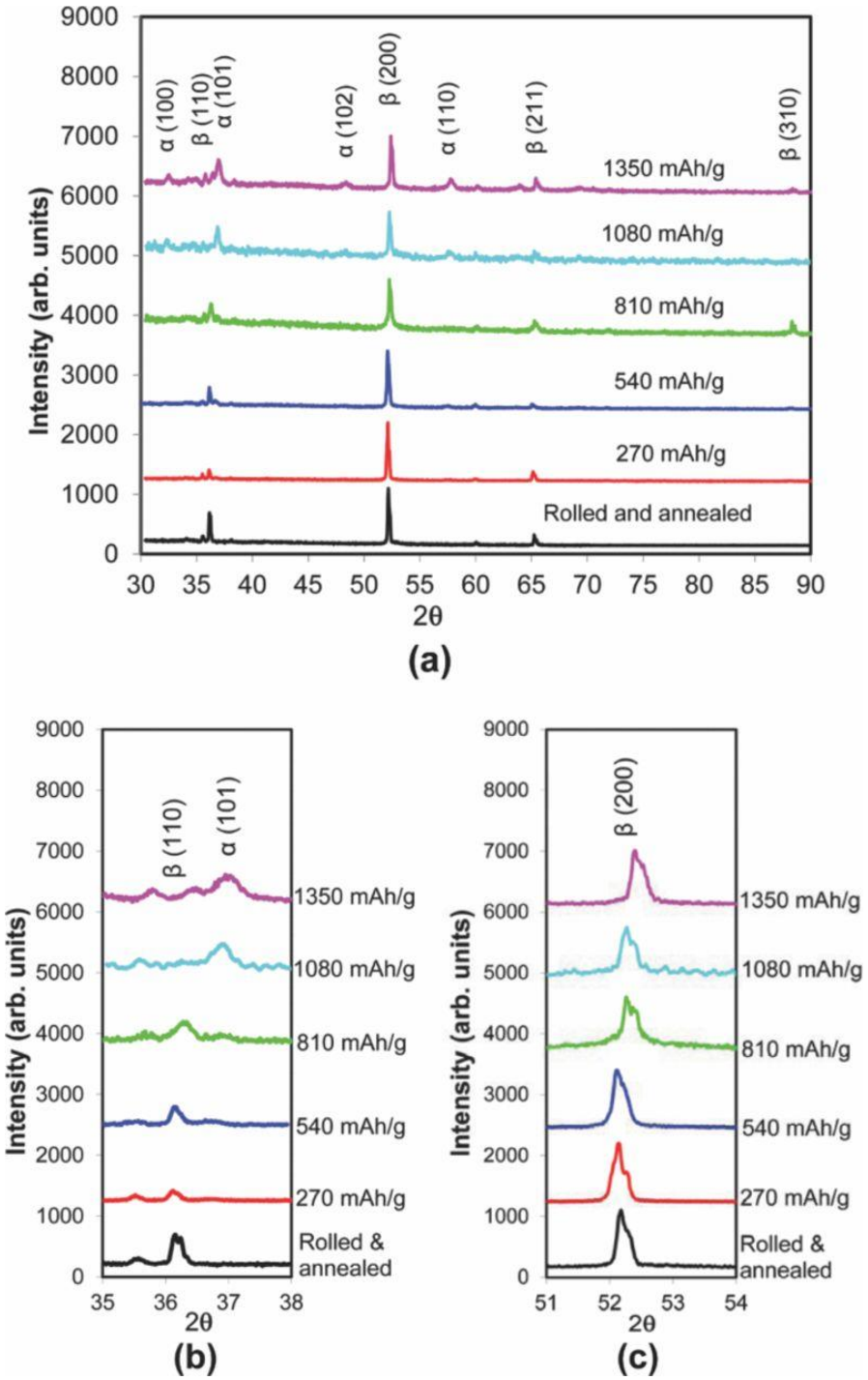

Figure 2.5 Diffraction patterns of Li-Mg alloy upon delithiation. (a) X-ray diffraction data for Li_8Mg alloy anodes with different states of discharge and magnified view of (b) β-phase (110) and α-phase (101) diffraction peaks, and (c) shifting of the (200) β-phase peak position. Reprinted with permission from Journal of the Electrochemical Society, 160 (2013) A1922-A1926 [14]. Copyright 2013, The Electrochemical Society.

However, due to the limited penetration depth of X-ray, the phase transition in the bulk electrode cannot be completely determined. It is of interest to see if the lithium distribution can be imaged, to determine how Li is spatially distributed at a given state of delithiation. Also, an analytical model to quantify the diffusion-controlled delithiation of Li-Mg alloy electrode, accompanied with phase transition and boundary movement, is needed for future battery design.

2.2.3 Li-Si Alloy Anodes

With a potential to offer the highest theoretical Li-storage capacity (4200 mAh/g), Si is another promising material for anodes in Li-ion batteries, but the ~300% volume change makes it really difficult to avoid cracking and delamination. Cyclic life is degraded by irreversible capacity loss and internal resistance increase [23-26].

A lot of effort has been made to accommodate such high volume change; nanosizing is one of the most effective ways. Arrays of wires in nanoscale dimensions can allow quick relaxation of stress, therefore the cracking of Si in bulk material can be avoided with nanostructured Si. Such anode can achieve ~3000 mAh/g after ~100 cycles at a relatively moderate cycling rate [26, 27]. Also, amorphous silicon has been found to have better performance than crystalline Si by avoiding the anisotropic volume expansion[28-33]. Amorphous thin film with thickness of 50 nm exhibits excellent reversibility and high capacity (200 cycles, ~3500 mAh/g) [34].

Although the high capacity and the good reversibility are obtained by various nanostructuring techniques, it is very difficult to extend such performance to larger scale. Therefore, a lot of research has been focused on powder or composite electrode studies, because it is easy to synthesize in large volume and relatively inexpensive [35-39].

Attempts have been made to maintain a two-phase microstructure of crystalline Si and amorphous a-Li_xSi during cycling (see Figure 2.6) to limit the volume expansion [40]. Based on the voltage plateaus of equilibrium titration in Li-Sn and Li-Si systems as shown in Figure 2.7, it is possible that this can be achieved by charging at a constant current to a fixed voltage (~170 mV) until the current decreases to a certain value (CCCV charging) [40] or constant capacity charge mode (CCC) [35, 41]. By avoiding further lithiation of crystalline Si core and controlling of the formation of final $Li_{15}Si_4$ crystalline phase, less volume expansion and good cycle life around 600-1200 mAh/g were realized. However, the high theoretical capacity of Si is not fully utilized.

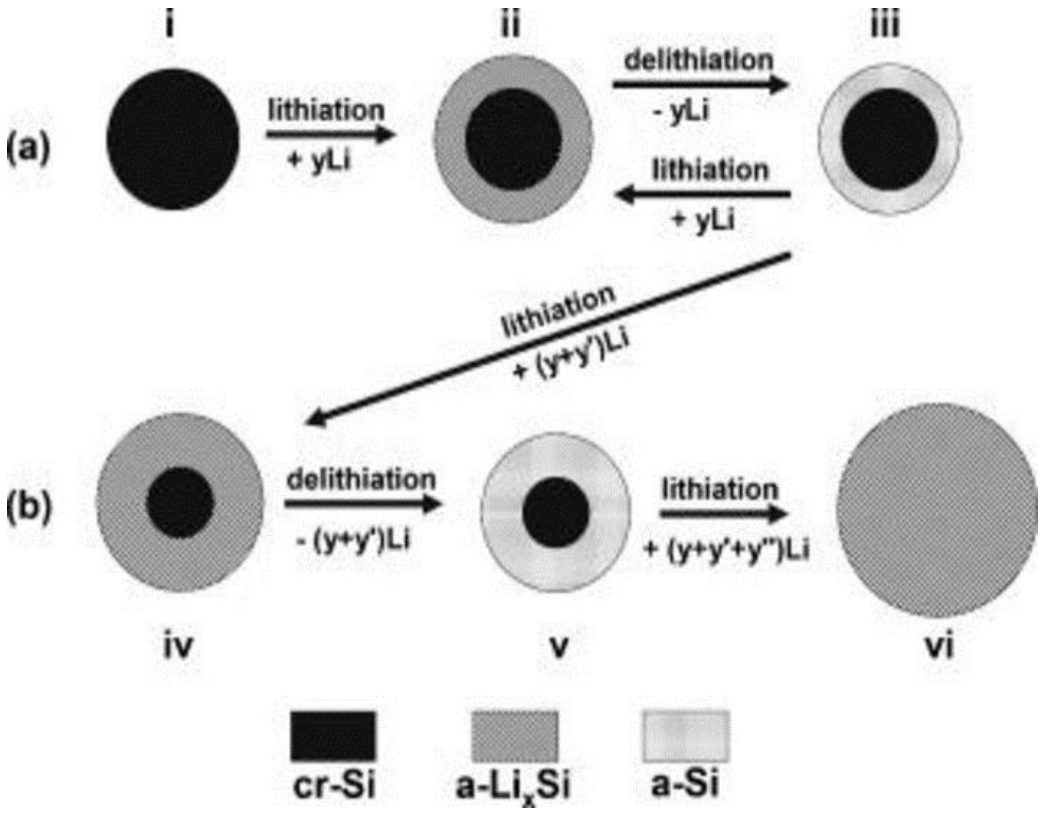

Figure 2.6 An illustration of how a single silicon particle changes its microstructure during cycling. Reprinted with permission from Journal of The Electrochemical Society, 154 (2007) A103 [40]. Copyright 2007, The Electrochemical Society.

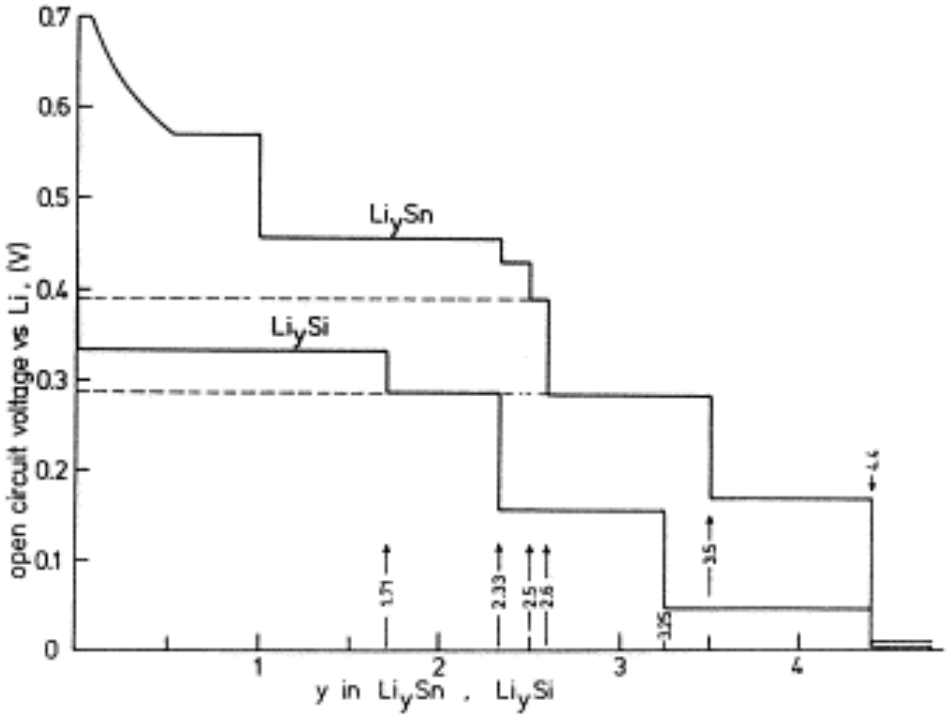

Figure 2.7 Voltage plateaus during equilibrium titration in Li-Sn and Li-Si systems [42]. Reprinted with permission from Journal of Power Sources, 81–82 (1999) 13-19, R. A. Huggins, Lithium alloy negative electrodes, Copyright 1999, Elsevier.

To achieve and to maintain the high theoretical capacity of Si over many charge/discharge cycles is quite challenging. It is reported that the performance of LIB, including both capacity and cycle life, increases with a decrease in the size of particle [43]. A critical size for cracking, above which Si fragmentation was seen, has been determined to be ~150 nm in the first lithiation cycle with in situ TEM [44]. Core-shell structure of Si nanopowder with carbon coating on Si core particles is developed to maintain a continuous path for electrons, stable SEI layer and to buffer internal stress [41, 45-47]. Binders and current collectors also play a very important role in affecting the capacity fading and reversibility of Si powder electrode. It is reported that in a buffered solution (pH=3) an ester-like Si-CH_3COO-R strong covalent bond will form. This results from the reaction of the carboxyl groups with the -OH groups at the surface of the thin SiO_2 layer surrounding

the Si particles [48-50]. Three-dimensional porous foam as current collector has been tried to provide continuous electron conducting path and to prevent cracking [51, 52]. Other modifications focusing on surface morphology of current collector have been done by the electrochemical method. By growing carbon or copper nanowires on the surface of the current collector, very good capacity (~2000 mAh/g) and cyclic life (>100 cycles) have been achieved [53, 54]. However, a low cost fabrication method has not yet developed for Si powder electrode with comparable performance.

The phase transitions of Si particle anodes, upon lithiation, was studied by Dahn et al. using in situ XRD [55]. An irreversible crystalline to amorphous phase transition was observed. Crystalline Si was found to become amorphous even during the first-cycle reaction with Li [40]. However, a clear understanding of the phase transitions associated with distinct electrochemical signatures has not been achieved. The signatures in fact suggest the possibility of existence of important phase transitions that are critical for successful Si anode performance. Specifically, it is suspected that the increased performance, as the size decreases from micron to nanoscale regime, is related to the peculiar structural changes and the proportion of crystalline/amorphous phases upon lithiation. To support this, there is some initial NMR evidence that the lithiation of Si occurs through various stages of local Li-Si atomic ordering and/or the formation of crystalline phases [56]. It is not well understood (i) how phase locally evolves during initial couple cycles, (ii) how particle size affects Si transformation into crystalline/amorphous phases and/or leading to the creation of peculiar structures and (iii) why such phases in nanosized particles provide superior cyclic capacity retention upon electrochemical Li insertion/removal.

2.3 Neutron Characterization Techniques

Neutron was firstly discovered by Chadwick in 1932 [57]. And the diffraction technique of neutrons was firstly demonstrated by Halban and Preiswerk [58], and also by Mithchell and Powers [59] in 1936. Because of the wave-particle duality of neutrons, similar to X-rays, various neutron techniques have been developed and become more and more crucial in numerous research areas over the years.

As we know, X-rays interact with the electrons. Therefore, the cross-sections of certain elements are highly dependent on the atomic number (*Z*). So, it is difficult to accurately determine the phase transitions which involve some light elements, such as Li and H in energy storage field (Li-ion batteries and fuel cells). However, the neutrons interact with nuclei instead of electrons; a comparison of scattering cross-section of neutron and X-ray is shown in Figure 2.8. In many studies, neutron techniques have shown their advantages, such as isotopic sensitivity, large penetration depth for elements with a high Z number, dramatically different coherent scattering cross-sections for light elements, sensitivity to bulk and buried structure, etc. [60-68].

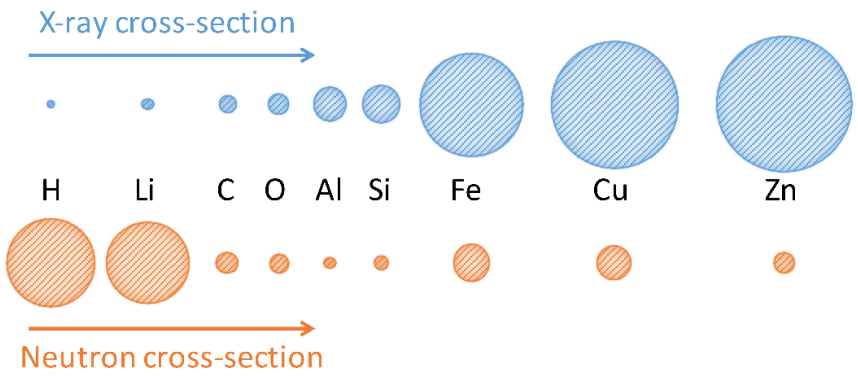

Figure 2.8 Comparison of neutron and X-ray total cross-sections for different elements. The area of each circle represents the total cross-section in barns (10^{-24} cm^2). Neutron data were taken from Neutron News, 3 (1992) 29-37 [64]. X-ray data were taken from NIST Standard Reference Database, 8 (1998) 3587-3597 [69].

2.3.1 Neutron Computed Tomography

Computed tomography is a powerful technique greatly developed in recent years because of the dramatically increased computational power. As we know, Li is a very light element and has a very small X-ray scattering cross-section. However, the neutron cross-section of Li is large. Also, due to the higher penetration depth of neutron compared with X-ray, it is possible to study the Li-containing electrodes such as Li-ion battery electrodes.

Figure 2.9 shows a schematic drawing of the instrument setup at CG-1D, Oak Ridge National Laboratory. It illustrates that the moderated and collimated neutrons are used as incident beams to interact with the mounted sample. After absorbing and scattering neutrons, a gray-scale 2D projection based on neutron transmission intensity is recorded [70, 71]. After recording over a thousand projections while rotating the sample, computed neutron tomography can be obtained.

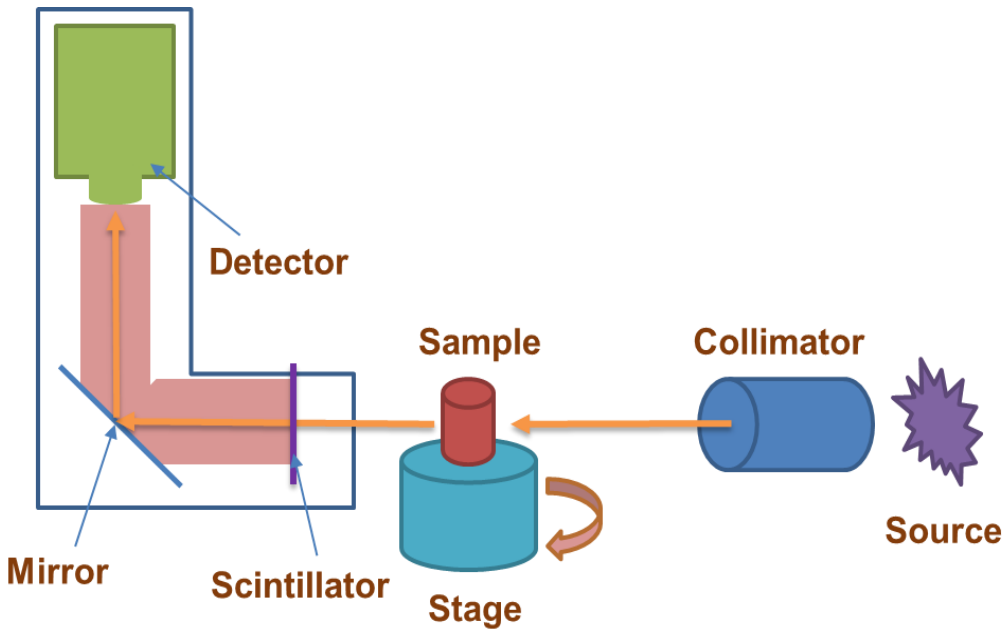

Figure 2.9 Schematic drawing of CG-1D neutron imaging setup.

In recent studies, neutron tomographic technique was successfully used to study qualitative Li spatial distribution in battery electrodes [72-76]. Figure 2.10 shows how the spatial distribution of Li in a carbon foam was mapped by Nanda et al. [72]. The imaging contrast comes from the differences in attenuation coefficient of the elements involved. The neutron attenuation can be described by Beer-Lambert law, $I = I_0 e^{-\mu x}$, where I_0 and I are the incident and transmitted intensity for a given neutron wavelength, respectively, and μ is the attenuation coefficient for a given wavelength, and x is the sample's thickness.

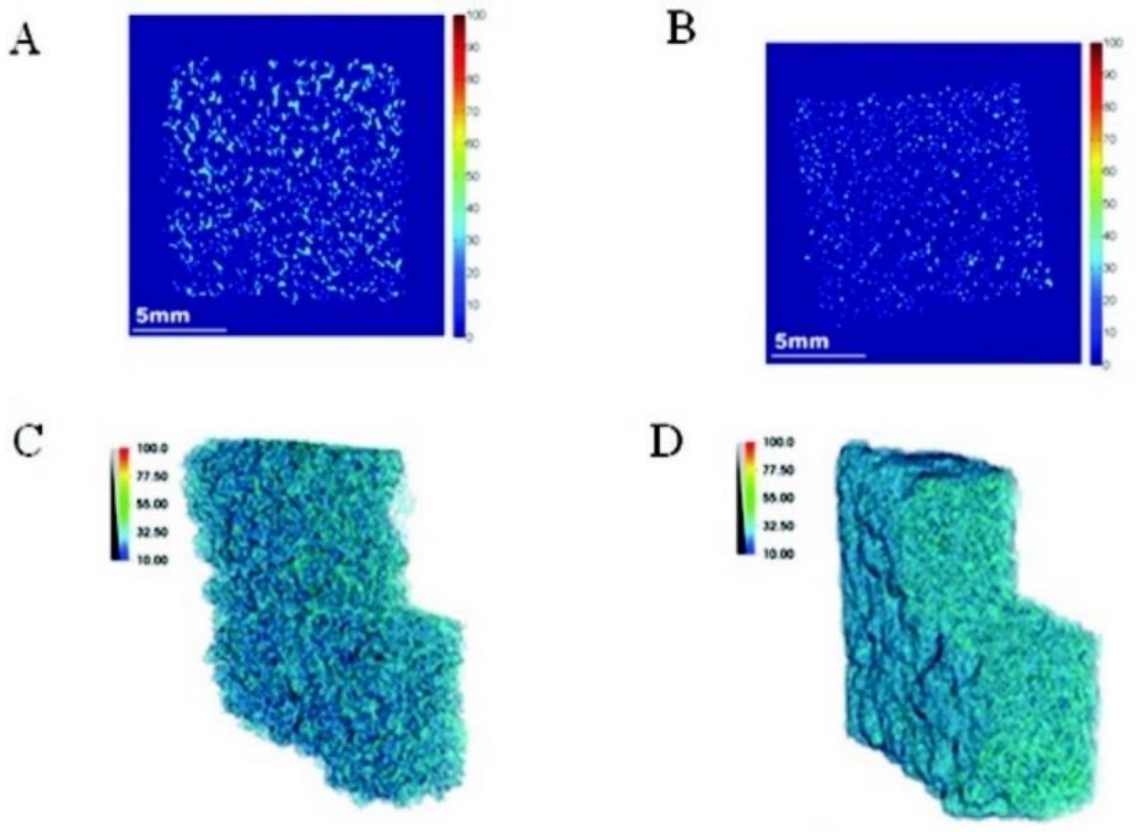

Figure 2.10 Normalized two-dimensional reconstructed slices of lithium peroxide-coated carbon foams: (A) 45 pores per inch (PPI) foam, (B) 100 PPI carbon foam, (C) reconstructed 3D tomography image of 45 PPI Li_2O_2-coated carbon foam, (D) reconstructed 3D tomography image of 100 PPI Li_2O_2-coated carbon foam. Reprinted with permission from The Journal of Physical Chemistry C, 116 (2012) 8401-8408 [72]. Copyright (2012) American Chemical Society.

The attenuation coefficient μ can be further written as

$$\mu = \sigma_{\text{tot}} N_{\text{A}} \rho / M \tag{2.4}$$

where σ_{tot} is the total cross-section for neutrons, N_A is Avogadro's number, ρ is the material's density and M is molecular weight [72, 77]. This can also be rewritten in another format as

$$\mu = \sigma_{\text{tot}} N_{\text{A}} c \tag{2.5}$$

where c is the molar concentration.

This greatly supported the feasibility of the quantitative mapping of Li bulk concentrations in Li containing electrodes. Furthermore, such quantitative information obtained is very useful for validating the analytical diffusion model developed for the bulk electrode.

2.4 Diffusion Modeling of Li-ion Batteries

An analytical model is extremely helpful in the regime of Li-ion battery study. In particular, for Li alloy electrodes, because of the possible phase transitions and the volume change associated with delithiation/lithiation, it is important to develop an analytical model to better understand the electrochemical behavior during charge/discharge. It can provide valuable insights for future battery design.

In the work by Doyle et al., a model to predict the cell voltages during galvanostatic charge/discharge of a Li-ion cell was first developed. The simulation data obtained by their model agreed with the experimental results [78]. In the later studies by Song et al. [79] and Thomas et al. [80], energy balance was introduced to this model in order to account for the

temperature changes during charge-discharge. In these models, the transport through electrolyte is addressed using the concentrated solution theory and the porous electrode theory.

A Nernst-Planck approach [81, 82] was used to model the behavior of all solid-state thin film batteries comprised of Li metal anode and $LiCoO_2$ cathode by considering the charge transfer kinetics at the electrode/electrolyte interface. The diffusion and migration of Li^+ ions through the solid electrolyte have been successfully modeled by applying boundary conditions of constant flux on one side and zero flux on the other side to solve the diffusional mass transport within $LiCoO_2$ thin film cathode. Another model for amorphous Si thin film was developed by Jagannathan et al. [83]. By solving Fick's law with certain boundary conditions, concentration profiles were obtained and used to obtained the overpotentials at the electrode/electrolyte interface. The simulated potential curve agreed reasonably with the experimental data. However, both models were not able to consider the phase transitions, which lead to associated boundary movements and volume expansion.

Without the consideration of phase transitions, phase boundary movement and volume change, the model of electrochemical process, regarding Li based alloy anode, cannot be valid. Thus, the objective of this research is to provide a comprehensive mathematical model that can more precisely describe the Li transport inside bulk electrode during charge/discharge. This model will be more direct, intuitive and can be adopted to simulate the delithiation/lithiation behavior of other alloy based electrodes.

2.5 References

[1] Y. Nishi, The Chemical Record, 1 (2001) 406-413.

[2] W.-J. Zhang, Journal of Power Sources, 196 (2011) 13-24.

[3] M. Hagen, E. Quiroga-González, S. Dörfler, G. Fahrer, J. Tübke, M.J. Hoffmann, H. Althues, R. Speck, M. Krampfert, S. Kaskel, H. Föll, Journal of Power Sources, 248 (2014) 1058-1066.

[4] D. Fauteux, R. Koksbang, Journal of Applied Electrochemistry, 23 (1993) 1-10.

[5] J.M. Tarascon, M. Armand, Nature, 414 (2001) 359-367.

[6] Y. Takeda, O. Yamamoto, N. Imanishi, Electrochemistry, 84 (2016) 210-218.

[7] Q. Wang, P. Ping, X. Zhao, G. Chu, J. Sun, C. Chen, Journal of Power Sources, 208 (2012) 210-224.

[8] D. Lisbona, T. Snee, Process Safety and Environmental Protection, 89 (2011) 434-442.

[9] D. Aurbach, E. Zinigrad, Y. Cohen, H. Teller, Solid State Ionics, 148 (2002) 405-416.

[10] D. Aurbach, Journal of the Electrochemical Society, 136 (1989) 906-913.

[11] R. Nesper, Progress in Solid State Chemistry, 20 (1990) 1-45.

[12] R. Nesper, Angewandte Chemie International Edition in English, 30 (1991) 789-817.

[13] S. Liu, J. Yang, L. Yin, Z. Li, J. Wang, Y. Nuli, Electrochimica Acta, 56 (2011) 8900-8905.

[14] M. Jagannathan, K.S.R. Chandran, Journal of the Electrochemical Society, 160 (2013) A1922-A1926.

[15] C. Wang, A. John Appleby, F.E. Little, Journal of Power Sources, 93 (2001) 174-185.

[16] M. Winter, J.O. Besenhard, Electrochimica Acta, 45 (1999) 31-50.

[17] A.A. Nayeb-Hashemi, J.B. Clark, A.D. Pelton, Bulletin of Alloy Phase Diagrams, 5 (1984) 365-374.

[18] A. Dey, Journal of The Electrochemical Society, 118 (1971) 1547-1549.

[19] M. Nicholson, Journal of The Electrochemical Society, 121 (1974) 734-738.

[20] Z. Shi, M. Liu, D. Naik, J.L. Gole, Journal of Power Sources, 92 (2001) 70-80.

[21] W.-J. Zhang, Journal of Power Sources, 196 (2011) 877-885.

[22] Y. Iwadate, M. Lassouani, F. Lantelme, M. Chemla, Journal of Applied Electrochemistry, 17 (1987) 385-397.

[23] X.-W. Zhang, P.K. Patil, C. Wang, A.J. Appleby, F.E. Little, D.L. Cocke, Journal of Power Sources, 125 (2004) 206-213.

[24] R.A. Huggins, Lithium alloy anodes, in: Handbook of Battery Materials, Wiley-VCH Verlag GmbH, 2007, pp. 359-381.

[25] J.O. Besenhard, J. Yang, M. Winter, Journal of Power Sources, 68 (1997) 87-90.

[26] C.K. Chan, H. Peng, G. Liu, K. McIlwrath, X.F. Zhang, R.A. Huggins, Y. Cui, Nature Nanotechnology, 3 (2008) 31-35.

[27] T. Song, J. Xia, J.-H. Lee, D.H. Lee, M.-S. Kwon, J.-M. Choi, J. Wu, S.K. Doo, H. Chang, W.I. Park, D.S. Zang, H. Kim, Y. Huang, K.-C. Hwang, J.A. Rogers, U. Paik, Nano Letters, 10 (2010) 1710-1716.

[28] S. Bourderau, T. Brousse, D.M. Schleich, Journal of Power Sources, 81–82 (1999) 233-236.

[29] P. Limthongkul, Y.-I. Jang, N.J. Dudney, Y.-M. Chiang, Journal of Power Sources, 119–121 (2003) 604-609.

[30] P. Limthongkul, Y.-I. Jang, N.J. Dudney, Y.-M. Chiang, Acta Materialia, 51 (2003) 1103-1113.

[31] H. Jung, M. Park, Y.-G. Yoon, G.-B. Kim, S.-K. Joo, Journal of Power Sources, 115 (2003) 346-351.

[32] V. Baranchugov, E. Markevich, E. Pollak, G. Salitra, D. Aurbach, Electrochemistry Communications, 9 (2007) 796-800.

[33] T.L. Kulova, A.M. Skundin, Y.V. Pleskov, E.I. Terukov, O.I. Kon'kov, Journal of Electroanalytical Chemistry, 600 (2007) 217-225.

[34] S. Ohara, J. Suzuki, K. Sekine, T. Takamura, Journal of Power Sources, 136 (2004) 303-306.

[35] N. Dimov, S. Kugino, M. Yoshio, Journal of Power Sources, 136 (2004) 108-114.

[36] H. Li, X. Huang, L. Chen, Z. Wu, Y. Liang, Electrochemical and Solid-State Letters, 2 (1999) 547-549.

[37] N. Hochgatterer, M. Schweiger, S. Koller, P. Raimann, T. Wöhrle, C. Wurm, M. Winter, Electrochemical and Solid-State Letters, 11 (2008) A76-A80.

[38] D. Mazouzi, B. Lestriez, L. Roué, D. Guyomard, Electrochemical and Solid-State Letters, 12 (2009) A215-A218.

[39] M. Gauthier, D. Mazouzi, D. Reyter, B. Lestriez, P. Moreau, D. Guyomard, L. Roué, Energy & Environmental Science, 6 (2013) 2145-2155.

[40] M.N. Obrovac, L.J. Krause, Journal of the Electrochemical Society, 154 (2007) A103-A108.

[41] M. Yoshio, H. Wang, K. Fukuda, T. Umeno, N. Dimov, Z. Ogumi, Journal of the Electrochemical Society, 149 (2002) A1598.

[42] R.A. Huggins, Journal of Power Sources, 81–82 (1999) 13-19.

[43] W.-R. Liu, Z.-Z. Guo, W.-S. Young, D.-T. Shieh, H.-C. Wu, M.-H. Yang, N.-L. Wu, Journal of Power Sources, 140 (2005) 139-144.

[44] X.H. Liu, L. Zhong, S. Huang, S.X. Mao, T. Zhu, J.Y. Huang, ACS Nano, 6 (2012) 1522-1531.

[45] H.-Y. Lee, S.-M. Lee, Electrochemistry Communications, 6 (2004) 465-469.

[46] Z. Luo, D. Fan, X. Liu, H. Mao, C. Yao, Z. Deng, Journal of Power Sources, 189 (2009) 16-21.

[47] Q. Si, K. Hanai, N. Imanishi, M. Kubo, A. Hirano, Y. Takeda, O. Yamamoto, Journal of Power Sources, 189 (2009) 761-765.

[48] J.S. Bridel, T. Azaïs, M. Morcrette, J.M. Tarascon, D. Larcher, Chemistry of Materials, 22 (2010) 1229-1241.

[49] N. Delpuech, D. Mazouzi, N. Dupré, P. Moreau, M. Cerbelaud, J.S. Bridel, J.C. Badot, E. De Vito, D. Guyomard, B. Lestriez, B. Humbert, The Journal of Physical Chemistry C, 118 (2014) 17318-17331.

[50] D. Mazouzi, Z. Karkar, C. Reale Hernandez, P. Jimenez Manero, D. Guyomard, L. Roué, B. Lestriez, Journal of Power Sources, 280 (2015) 533-549.

[51] T. Jiang, S. Zhang, X. Qiu, W. Zhu, L. Chen, Electrochemistry Communications, 9 (2007) 930-934.

[52] H.C. Shin, M. Liu, Advanced Functional Materials, 15 (2005) 582-586.

[53] D. Reyter, S. Rousselot, D. Mazouzi, M. Gauthier, P. Moreau, B. Lestriez, D. Guyomard, L. Roué, Journal of Power Sources, 239 (2013) 308-314.

[54] Z. Du, S. Zhang, T. Jiang, R. Lin, J. Zhao, Electrochimica Acta, 74 (2012) 222-226.

[55] J. Li, J.R. Dahn, Journal of the Electrochemical Society, 154 (2007) A156.

[56] B. Key, M. Morcrette, J.-M. Tarascon, C.P. Grey, Journal of the American Chemical Society, 133 (2011) 503-512.

[57] J. Chadwick, Nature, 129 (1932) 312.

[58] H. Von Halban, P. Preiswerk, Comptes Rendus de l'Académie des Sciences, 203 (1936) 73.

[59] D.P. Mitchell, P.N. Powers, Physical Review, 50 (1936) 486-487.

[60] R. Pynn, Physical Review B, 45 (1992) 602.

[61] G.L. Squires, Introduction to the theory of thermal neutron scattering, Cambridge University Press, 2012.

[62] V.F. Sears, Canadian Journal of Physics, 44 (1966) 1299-1311.

[63] J.S. Higgins, H. Benoît, Polymers and neutron scattering, Clarendon Press Oxford, 1994.

[64] V.F. Sears, Neutron News, 3 (1992) 26-37.

[65] K. Ibel, H. Stuhrmann, Journal of Molecular Biology, 93 (1975) 255-265.

[66] R. Birgeneau, H. Guggenheim, G. Shirane, Physical Review B, 1 (1970) 2211.

[67] W. Marshall, S.W. Lovesey, Theory of thermal neutron scattering: the use of neutrons for the investigation of condensed matter, Clarendon Press, 1971.

[68] P.M. Chaikin, T.C. Lubensky, Principles of condensed matter physics, Cambridge University Press, 2000.

[69] M.J. Berger, J. Hubbell, S. Seltzer, J. Chang, J. Coursey, R. Sukumar, D. Zucker, K. Olsen, NIST Standard Reference Database, 8 (1998) 3587-3597.

[70] L. Santodonato, H. Bilheux, B. Bailey, J. Bilheux, P. Nguyen, A. Tremsin, D. Selby, L. Walker, Physics Procedia, 69 (2015) 104-108.

[71] L. Crow, L. Robertson, H. Bilheux, M. Fleenor, E. Iverson, X. Tong, D. Stoica, W.T. Lee, Nuclear Instruments and Methods in Physics Research Section A: Accelerators, Spectrometers, Detectors and Associated Equipment, 634 (2011) S71-S74.

[72] J. Nanda, H. Bilheux, S. Voisin, G.M. Veith, R. Archibald, L. Walker, S. Allu, N.J. Dudney, S. Pannala, The Journal of Physical Chemistry C, 116 (2012) 8401-8408.

[73] J.B. Siegel, X. Lin, A.G. Stefanopoulou, D. Gorsich, in: American Control Conference (ACC), 2011, IEEE, 2011, pp. 376-381.

[74] L.G. Butler, B. Schillinger, K. Ham, T.A. Dobbins, P. Liu, J.J. Vajo, Nuclear Instruments and Methods in Physics Research Section A: Accelerators, Spectrometers, Detectors and Associated Equipment, 651 (2011) 320-328.

[75] G.V. Riley, D.S. Hussey, D. Jacobson, ECS Transactions, 25 (2010) 75-83.

[76] D. Goers, M. Holzapfel, W. Scheifele, E. Lehmann, P. Vontobel, P. Novák, Journal of Power Sources, 130 (2004) 221-226.

[77] D.F. Swinehart, Journal of Chemical Education, 39 (1962) 333.

[78] M. Doyle, T.F. Fuller, J. Newman, Journal of the Electrochemical Society, 140 (1993) 1526-1533.

[79] L. Song, J.W. Evans, Journal of the Electrochemical Society, 147 (2000) 2086-2095.

[80] K.E. Thomas-Alyea, J. Newman, G. Chen, T.J. Richardson, Journal of the Electrochemical Society, 151 (2004) A509-A521.

[81] D. Danilov, P.H.L. Notten, Electrochimica Acta, 53 (2008) 5569-5578.

[82] D. Danilov, R.A.H. Niessen, P.H.L. Notten, Journal of the Electrochemical Society, 158 (2011) A215-A222.

[83] M. Jagannathan, K.S.R. Chandran, Journal of Power Sources, 247 (2014) 667-675.

CHAPTER 3

THE NATURE OF ELECTROCHEMICAL DELITHIATION OF LI-MG ALLOY ELECTRODES: NEUTRON COMPUTED TOMOGRAPHY AND MODELING OF DELITHIATION PHENOMENON

(Manuscript submitted)

3.1 Introduction

The evolution of small portable electronic devices and the development of rechargeable plug-in electric vehicles are pushing for Li-ion batteries with higher energy capacity and power density than what is available today. It is well known that lithium metal is a promising anode material because of its high theoretical specific capacity (3829 mAh g^{-1}) and its large negative electrode potential (-3.04V vs. normal hydrogen electrode). But the high reactivity of Li and the possibility of ignition due to dendrite formation make any rechargeable cell with Li metal as anode an unlikely prospect. On the other hand, Li-rich Li-Mg alloy is an interesting alternate anode material [1]. Li-Mg alloy is advantageous because of the generally lower reactivity of Li (or relatively low Li activity), the large solid solution range, the mechanical integrity of Mg framework and a relatively large diffusion coefficient of Li (~10^{-7} cm^2 s^{-1} for the Li-Mg alloy produced by vapor deposition) [2, 3]. The energy storage capacities of Li-Mg alloys are relatively high, and can be adjusted easily by varying the Li content. For example, the theoretical capacity is 2690 mAh g^{-1} for the Mg-70 wt.% Li alloy. However, the mechanism of electrochemical delithiation in Li-Mg alloy electrodes has not been investigated before. In the first detailed work using this alloy, Jagannathan et al. [4] observed the gradual phase transitions at the surface of Li-Mg electrodes, during delithiation, using X-ray diffraction. However, the distribution of Li in the bulk of the electrode cannot be determined using X-rays due to limits to its depth of penetration and the limited sensitivity to light elements as Li.

Recently, neutron computed tomography was successfully used to determine the spatial distribution of Li in bulk battery electrodes [5-8]. In neutron tomography, transmitted neutrons are captured by a scintillator and recorded as a gray scale radiograph called a

projection (or shadow) radiograph. The imaging contrast comes from the differences in attenuation coefficients of the elements involved in the sample. The interactions of neutrons and elements can be described by Beer-Lambert law, $I = I_0 \exp(-\Sigma \mu_i x_i)$, where I_0 and I are the incident and the transmitted intensity, respectively, and μ_i is the total attenuation coefficient (including absorption and scattering) of element, i, and x_i is the effective thickness of the element on the neutron path. The attenuation coefficient μ_i is given by $\mu_i = \sigma_{\text{tot},i} N_A c_i$, where $\sigma_{\text{tot},i}$ is the total neutron cross-section for the element, N_A is Avogadro's number, c_i is the molar concentration [5].

Table 3.1 lists the thermal neutron scattering and absorption cross-sections from NIST (National Institute of Standard and Technology) [9] for the elements involved in this study. The neutron scattering cross-section is the sum of coherent and incoherent cross-sections. The sum of scattering and absorption cross-sections gives the total cross-section ($\sigma_{\text{tot},i}$). From Table 3.1, it can be seen that the total cross-section of Mg (3.773 barns) is significantly less than that of natural Li (71.87 barns). This leads to the large difference in neutron attenuation coefficient of Li with respect to Mg and makes it possible to spatially map the distribution of Li in Li-Mg alloy electrode.

Table 3.1 Neutron scattering and absorption cross-sections in barns (10^{-24} cm^2)

Element	Coherent cross-section $\sigma_{\text{coh}}(\lambda)$	Incoherent cross-section $\sigma_{\text{inc}}(\lambda)$	Scattering cross-section $\sigma_{\text{scatt}}(\lambda)$	Absorption cross-section $\sigma_{\text{abs}}(\lambda)$	Total cross-section $\sigma_{\text{tot}}(\lambda)$
Li	0.454	0.92	1.37	70.5	71.87
Mg	3.631	0.08	3.71	0.063	3.773
Al	1.495	0.0082	1.503	0.231	1.734
Ar	0.458	0.225	0.683	0.675	1.358

In this work, three-dimensional (3D) neutron computed tomography has been used to map Li distribution in delithiated Li-Mg electrodes. The Li concentration profiles at different levels of delithiation were extracted from the neutron imaging data. To achieve a quantitative understanding of the delithiation process in Li-Mg alloy, a diffusion-based analytical modeling methodology was developed. This was used to mathematically calculate Li concentration profiles at different levels of Li depletion. It is shown that the experimental Li concentration distributions across the electrode can be correlated with the calculations from diffusion modeling. The analysis and interpretation of mechanisms regarding mass transport, phase transition and boundary movement has provided an improved understanding of the mechanisms of delithiation in Li-Mg alloy electrodes.

3.2 Materials and Experimental Procedure

3.2.1 Li-Mg Alloy Preparation

Li-Mg alloys were prepared by firstly melting Li rods (99.9%, ESPI metals, Ashland, OR) in a stainless steel crucible inside an argon filled glove box. Mg chips (99.98%, Sigma-Aldrich) were gradually added to the melt. The weight of both Li rods and Mg chips was controlled to obtain the alloy with targeted compositions. Based on the targeted composition, the temperature was controlled according to the Li-Mg phase diagram [10] as shown in Figure 3.1. The melt was kept stirring throughout this process to obtain the compositional homogeneity.

In this work, two alloys of compositions Mg-70 wt.% Li and Mg-50 wt.% Li were made. The compositional homogeneity of the cast Li-Mg alloy ingots was verified by ICP-AES analysis. The results, shown in Table 3.2, indicate that the alloys were homogenous within ±3 wt.% of Li.

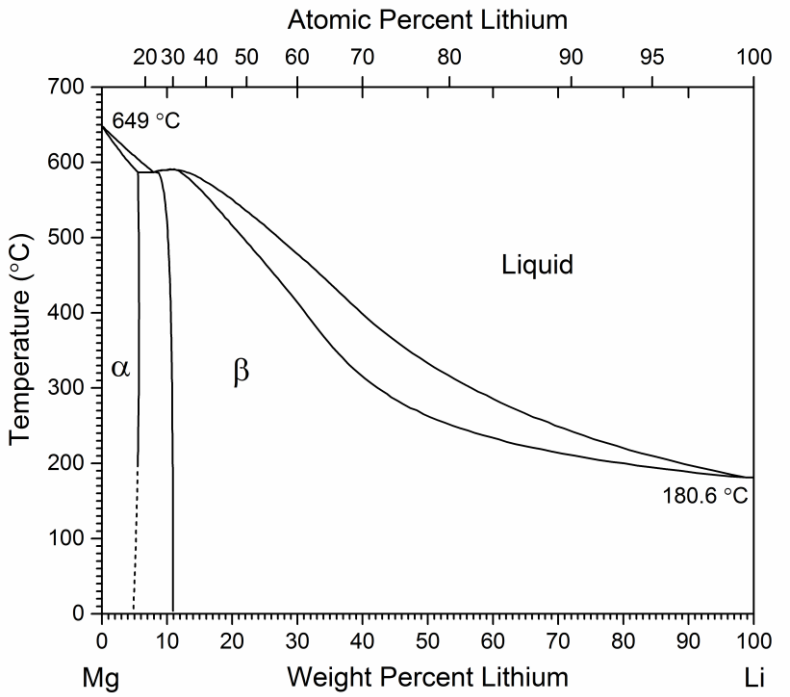

Figure 3.1 Equilibrium phase diagram for Mg-Li system [10].

Table 3.2 Compositions of the two Li-Mg alloys as determined by ICP-AES analysis

ICP Sample Number	Li wt.% from ICP for Mg-70 wt.% Li	Li wt.% from ICP for Mg-50 wt.% Li
1	69.37	52.30
2	73.41	51.14
3	70.35	51.27

In order to prepare the Li-Mg alloy electrodes for electrochemical cycling, Li-Mg alloy strips, cut from the alloy ingots, were cold rolled into ~1.0 mm thick foils at room temperature. The foils were then annealed in Ar atmosphere for 24 hours at 140℃ to recrystallize the material and to eliminate the rolling texture. Li-Mg alloy disk electrodes having the diameter of 3.97 mm and the thickness of ~1 mm were made by punching the annealed foil.

3.2.2 Preparation of Delithiated Samples

The Li-Mg alloy electrodes used for neutron imaging experiments were prepared by delithiating them to known depths of Li depletion. Metallic Li foils (99.9%, Alfa Aesar) with 0.75 mm in thickness and 6.35 mm in diameter were first used as cathode to delithiate the Li-Mg alloy. After some trials, delithiation of Li-Mg alloy was successfully achieved, but the formation of Li dendrites caused shorting, which limited the delithiation capacity to 2~3 mAh. To alleviate this problem in preparing the heavily delithiated samples, porous MnO_2 disks with 0.5 mm in thickness and 6.35 mm in diameter were used. Swagelok cells with Li-Mg alloy anode, the separator (Celgard 2400) and the cathode (MnO_2 disk or Li foil) were assembled inside a glove box. The electrolyte containing 1M $LiPF_6$ solution (MTI Corp. Richmond, CA) in 1:1:1 ratio of EC (ethylene carbonate): DMC (dimethyl carbonate): DEC (diethyl carbonate) was used. The delithiation was performed using either Keithley 2401 source-meter or Gamry Reference 3000 potentiostat with constant current density of 0.51 mA cm^{-2}.

By controlling the duration of delithiation process, Li-Mg electrodes with different depths of delithiation (around 10%, 20%, 30% and 40% Li depletion by at.%) were prepared. The delithiated samples were then assembled and sealed in an aluminum canister inside a glove box. In order to minimize the scattering interference from adjacent samples during neutron experiments, aluminum rings with 1 mm in thickness and 3.97 mm in outer diameter were placed between electrodes.

3.2.3 Neutron Computed Tomography (CT) and Data Visualization

Neutron CT was performed at the CG-1D Neutron Imaging Facility at the High Flux Isotope Reactor (HFIR), Oak Ridge National Laboratory, USA. Figure 3.2(a) is the

schematic of the instrument setup at the beamline and Figure 3.2(b) shows the sample arrangement inside the aluminum sample holder.

At the HFIR, neutrons are generated by fission reaction in the 85 MW reactor core. Thermal neutrons scatter from the beryllium reflector and reach a supercritical hydrogen moderator with a temperature of 17 K. This provides a source of cold neutrons with increased flux between 4 and 12 Å. The CG-1D imaging beamline sits at the end of the cold guide 1 neutron guide system and provides neutrons with wavelengths between 0.8 and ~ 6 Å, with a peak around 2.6 Å, for measurement.

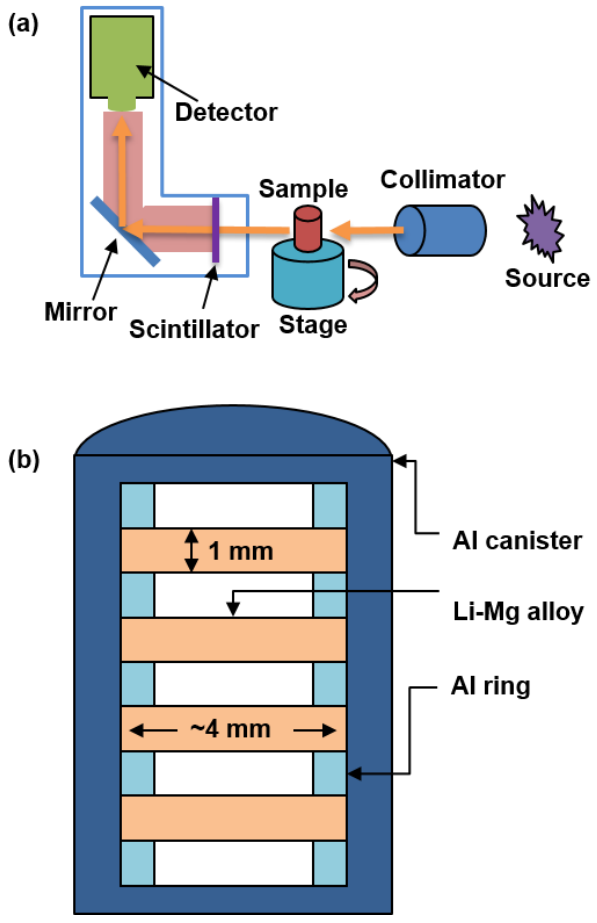

Figure 3.2. Schematic drawings of (a) CG-1D neutron imaging set up and (b) cross-sectional view of sample arrangement inside Al canister.

After flying through a pinhole, neutrons are collimated using a series of beam scrapers. A 50 μm ^{6}LiF/ZnS scintillator converts the transmitted neutron into light that is recorded by a charge-coupled device (CCD) camera. A gray-scale 2D projection based on neutron transmission intensity is saved as raw data [11, 12]. For volume reconstruction, the sample is mounted on a rotation stage which rotates through 180° to collect over a thousand of radiographs. In this work, each projection was taken in rotation steps of ~0.1° with 60 s exposure time. Postprocessing of the raw data was completed using *ImageJ* [13] to correct for background noise. From the recorded projections data, the electrode volume was successfully reconstructed by filtered-back-projection (FBP) method using *Octopus* [14]. The 3D visualization of the image and data analysis was a done using *ImageJ* and *VG Studio*. *VG Studio* is a 3-dimensional visualization software developed by Volume Graphics GmbH, located in Heidelberg, Germany.

3.3 Results and Discussion

3.3.1 Delithiation Behavior of Li-Mg Electrodes

Figure 3.3(a) and (b) show the capacity versus voltage profiles (vs. Li/Li^{+}) during the delithiation of Li-Mg alloy using Li and MnO_2 as cathode, respectively. Due to the large Li content of Li-Mg alloy (~22 mAh total for Mg-70 wt.% Li alloy sample weighing 0.008g), multiple delithiation steps (indicated as I, II and III in Figure 3.3) were needed to obtain heavily delithiated electrodes. After each delithiation stage, the delithiation was stopped and a new cathode was used for further delithiation.

In the experiments, the measured open circuit voltage (OCV) of Mg-70 wt.% Li is ~0.01 V against Li foil and it is -3.07 V against MnO_2. Because two different cathodes were used during the delithiation process, the voltage vs. capacity plot with MnO_2 cathode

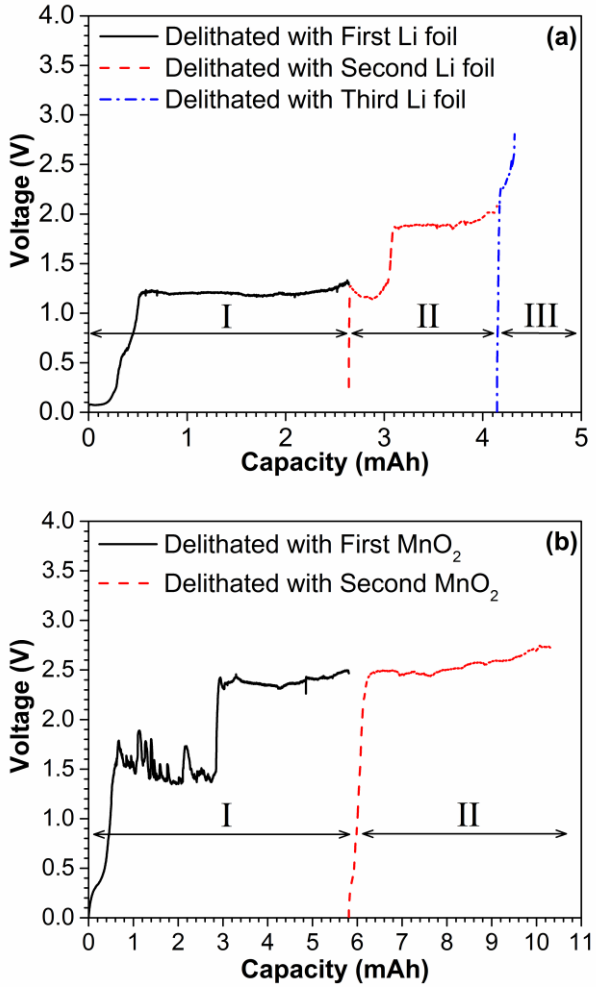

Figure 3.3. Voltage vs. capacity curves during the delithiation of Li-Mg. (a) Delithiation curve of Mg-70 wt.% Li using Li foil, with ~18% Li depleted at the end of all stages. (b) Delithiation curve of Mg-70 wt.% Li using MnO_2 disk, with ~41% Li depleted after two stages.

has been approximately converted to Li/Li^+ redox potentials based on their OCV values. The converted data are shown in Figure 3.3(b). In Figure 3.3(a), two voltage plateaus, ~1.2 V and ~1.9 V, can be observed with Li as cathode. In Figure 3.3(b), two voltage plateaus, ~1.4 V and ~2.35 V, can also be observed with MnO_2 as cathode. The respective potential differences of 0.2 V and 0.45 V may be explained on the basis of different conductivities in metallic Li and porous MnO_2.

In this work, the maximum amount of Li extracted by a single Li foil (0.75 mm in thickness, 6.35 mm in diameter) is about 2~3 mAh. However, the maximum extraction capacity of MnO_2 cathode (0.5 mm in thickness and 6.35 mm in diameter) can reach as high as 7~9 mAh. This difference is possibly due to the different storage mechanisms of Li, that is, deposition on Li versus intercalation in MnO_2, respectively. While using MnO_2 to delithiate Li-Mg alloy, the depleted Li is stored by intercalation and the tendency of Li plating on the surface of MnO_2 is much less than the one of metallic Li foil. Also, in porous MnO_2, there is almost no diffusion limitation for Li to transport to the inner bulk. Therefore, its capacity for Li depletion from Li-Mg is higher than what Li foil could offer.

The Li deposit on Li foil was further studied using SEM (Figure 3.4). In Figure 3.4(a), at the right-most, the region which was not faced by the alloy anode throughout the delithiation process is labeled as Li foil. And the regions labeled as I and II are the deposit of Li formed on the top of the metallic Li foil. There is an imaginary outline of the Li-Mg anode (dotted line on the right of Region I) to indicate where the Li-Mg alloy is supposed to be placed in the assembled cell. Two different morphologies of Li deposition were observed. In the circular area of Li-Mg anode, Li is deposited as layers of small islands due to the restricted interelectrode space (25 μm, the thickness of separator) between cathode and anode. But outside this region (area from edge to outward), large dendritic Li deposits were observed. This indicates that although the depleted Li can deposit within the electrode area, it also tended to deposit at the peripheral regions. The outer deposits formed as the dendritic/porous structure as shown in Figure 3.4(b) and (c). After a certain amount of Li depletion, this dendritic structure grew through the separator and caused electrical shorting. This limited the delithiation capacity to about 2-3 mAh.

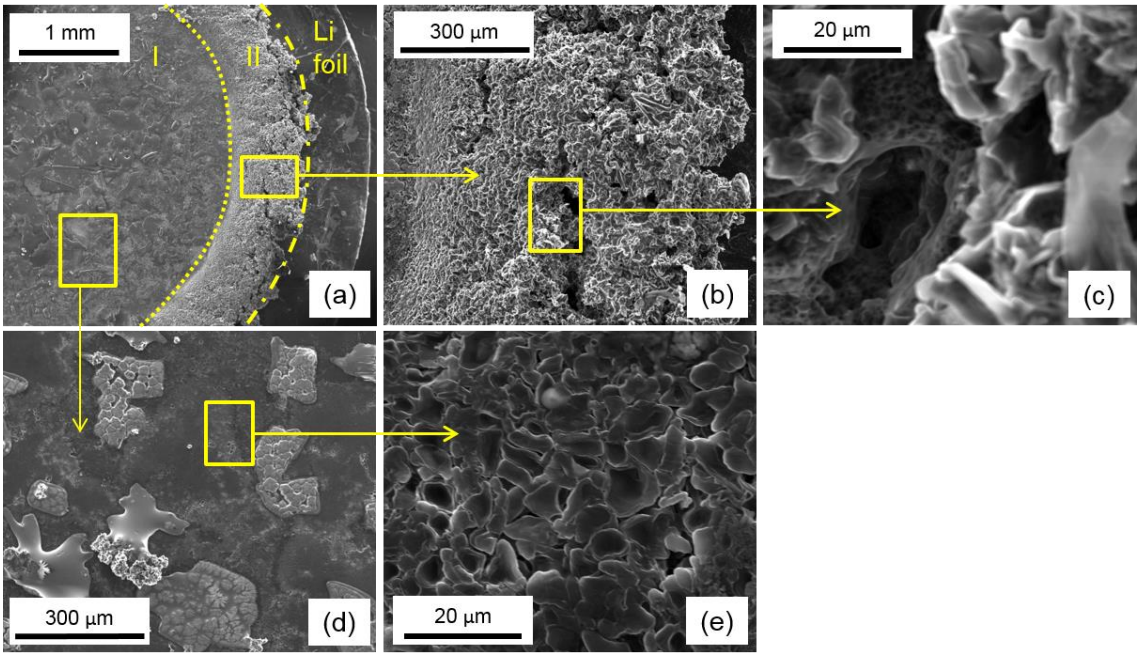

Figure 3.4. SEM photographs of Li deposit on Li cathode. (a) Overview of Li deposition on Li foil. (b) Magnified Li deposition where adjacent Li-Mg was placed. (c) Further magnified region from (b). (d) Magnified Li deposition where Li-Mg was placed. (e) Further magnified region from (d).

3.3.2 Correlation with X-ray Diffraction

In the previous study of Jagannathan et al. [4], the voltage plateau of delithiation in Li-Mg alloy was seen at about 2 V with MnO_2 as cathode. Base on the measured OCV (3.25 V) in their work, this voltage plateau can be converted to ~1.25 V vs. Li/Li^+, which is consistent with the first voltage plateau (~1.2 V) observed in our study (Figure 3.3(a)). The potential difference of ~0.05 V may be explained by the increased resistance resulting from the larger thickness of Li-Mg sample, which is required for neutron imaging. However, unexpected second voltage plateaus (~1.9 V vs. Li/Li^+ while using Li cathode and ~2.35 V vs. Li/Li^+ while using MnO_2 cathode) were observed, and existed through the delithiation in stage II in both Figure 3.3(a) and (b). To confirm the phases present at the active surface, X-ray diffraction (XRD) was performed on two Li-Mg alloy anodes, which were

delithiated to the extents (~1.5 mAh and ~4.5 mAh) marked by red crosses in Figure 3.5(a). The diffraction patterns are shown in Figure 3.5(b), and the enlarged views are shown in Figure 3.5(c) and (d). It can be seen that the α-phase has formed on the surfaces of both delithiated samples. It is important to note that the phase transition from β-phase to α-phase could occur even with a relatively low level of total Li depletion (~1.5 mAh). Also, it can be seen (Figure 3.5(c)) that the strength of the α peak increased with delithiation. This indicates that the Li depletion leads to the formation of α+β phase region at the active surface of the electrode. Because of the significantly lower RT diffusivity of Li in α phase [4], a larger electrochemical driving force will be needed. Therefore, an elevated plateau voltage, which is seen in Figure 3.3(a) and (b), can be explained. Additionally, the large sample thickness (which is required here for neutron imaging) could also provide a kinetic barrier for Li transport from the deeper region of the electrode. A higher potential may be needed in such a case. More studies will need to be performed to understand the effects of the kinetic barriers.

With such a high electrochemical driving force (~1.9 V vs. Li/Li^+) during the second voltage plateau (Figure 3.3(a)), Mg depletion might be suspected to occur, because the reported oxidation potential for Mg in Li-Mg alloy is around 1.35V vs. Li/Li^+ [2]. To investigate this, the Li foil cathode, which was used for delithiation of ~15% Li, was examined. The composition of Li deposit including both the regions shown in Figure 3.4 was analyzed by energy dispersive analysis of X-rays (EDAX). The analysis revealed the composition to be (in at.%): 40.44% C, 28.70% O, 25.56% F, 4.46% P and 0.84% Mg. The C, O, F and P most likely come from crystallized electrolyte (composed of $LiPF_6$, EC, EMC and DEC). Since Li cannot be analyzed using the EDAX technique, the ratio of Li

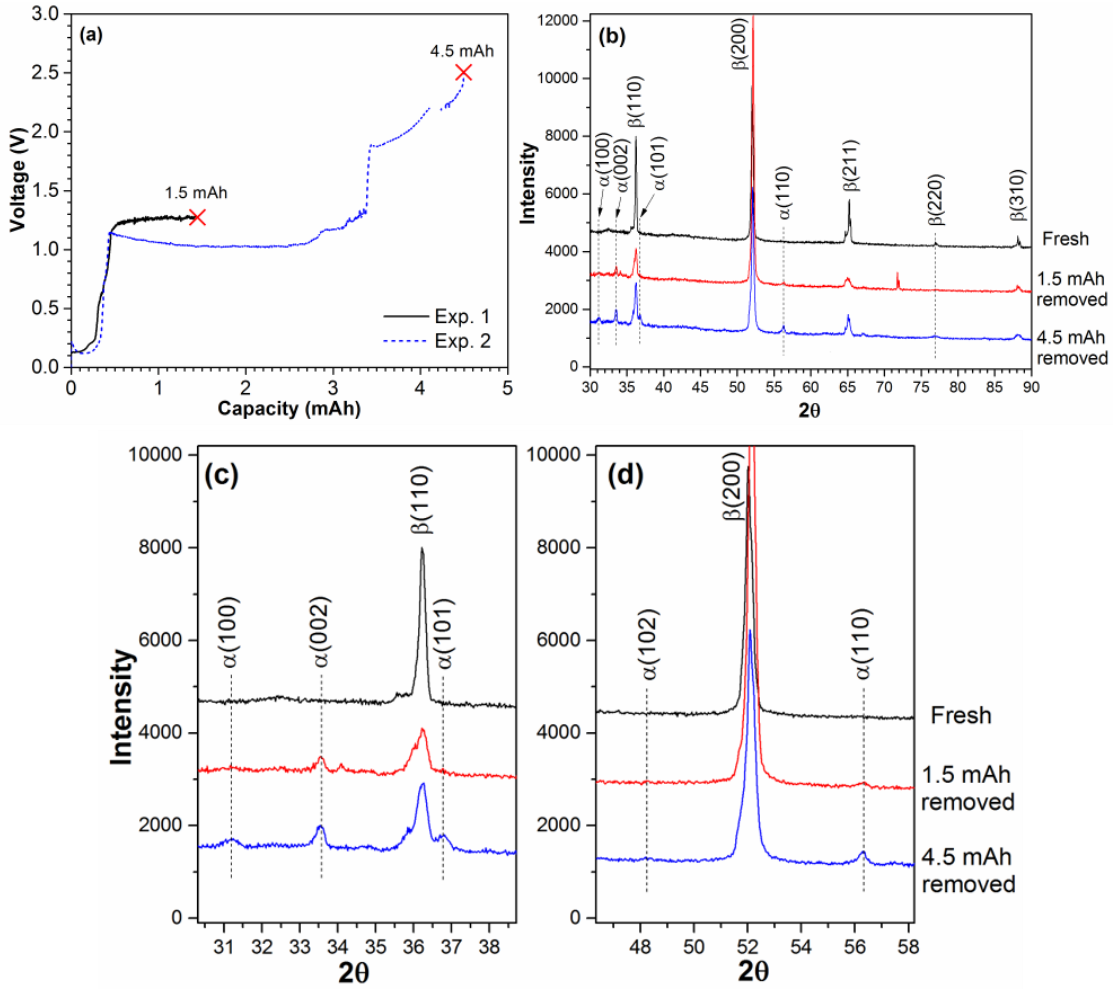

Figure 3.5. Cycling curves and the XRD results. (a) Voltage vs. capacity curves for the samples used for XRD. (b) X-ray diffraction data for Mg-70 wt.% Li samples. (c) and (d) The enlarged peaks from (b).

and Mg content could not be directly determined, but the content of Mg can be indirectly estimated by the overall mass balance in the residual electrolyte. The atomic percentage of Mg is estimated to be 0.84% on the basis of the bulk composition of the crystallized electrolyte. This amount of Mg clearly came from Li-Mg alloy under the high electrochemical driving force. However, it is negligible compared to the volume of Li deposit. Based on this, it can be concluded that the delithiation of Li-Mg alloy largely involved the depletion of Li and not Mg.

3.3.3 Neutron Imaging of Li Bulk Distribution

After the 3D reconstruction of neutron imaging data, the cross-sectional views at the center of each Li-Mg electrode, on the basis of neutron attenuation coefficients, are shown in Figure 3.6 and Figure 3.7 for Mg-70 wt.% Li and Mg-50 wt.% Li alloys, respectively. In these figures the active side, where Li was depleted from, is on the right side of each electrode. The color scale bar on the left scales the attenuation values of the neutron beam. A higher attenuation intensity value represents a relatively higher Li concentration in that region.

In Figure 3.6 and Figure 3.7, the fresh electrodes (far left) show relatively uniform Li concentrations across the thickness as expected. However, the edges of the samples show lower neutron attenuation, indicating a lower concentration of Li. In the electrode without depletion of Li, this edge effect is very symmetrical around the electrode as illustrated in Figure 3.6 and Figure 3.7. This is likely due to the undersampling of neutron signal recorded by CCD camera and some sample surface refraction [15]. This symmetrical effect disappears when Li has been depleted from the electrode (see Figure 3.6 and Figure 3.7). The asymmetry is observed on the Li depleted side (right side) and is more pronounced as a function of Li depletion, as expected. A noticeable decrease in attenuation from top and bottom toward the center of the cell may be due to beam hardening effect [16, 17] and the difficulty of neutrons transmitting through the thicker part of the cell. However, in this work, the depth of the region with the edge effect was determined from the imaging data of fresh Li-Mg sample. And this was used to locate the depth of edge effect on the delithiated side of the other samples. This location is used in Section 3.3.4.3 to highlight the Li depletion as a function of time.

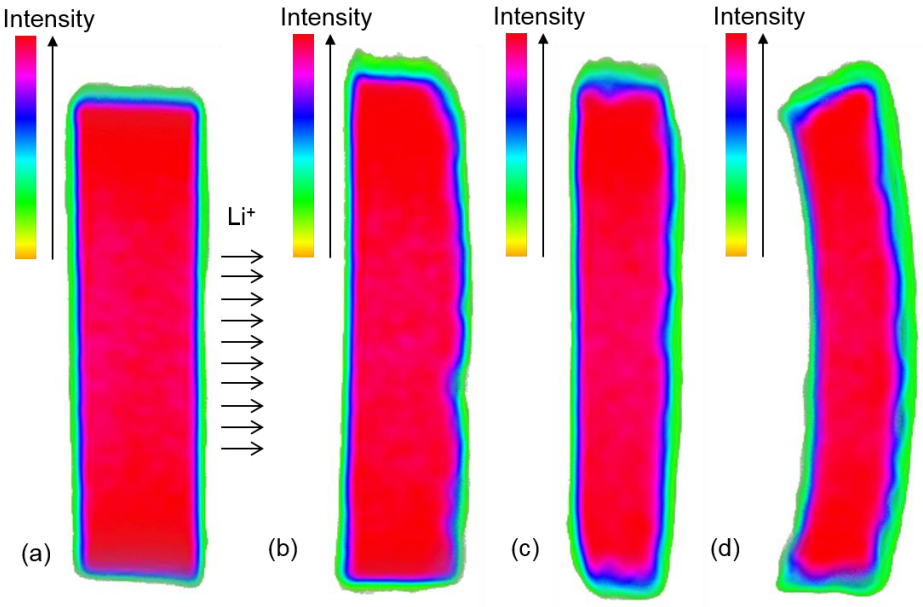

Figure 3.6. Cross-sectional views of reconstructed pseudo-color volume for Mg-70 wt.% Li alloys: (a) fresh electrode with no Li depletion, (b) with 17.78% Li depletion, (c) with 32.3% Li depletion and (d) with 41% Li depletion. Colors are assigned according to different attenuation intensities.

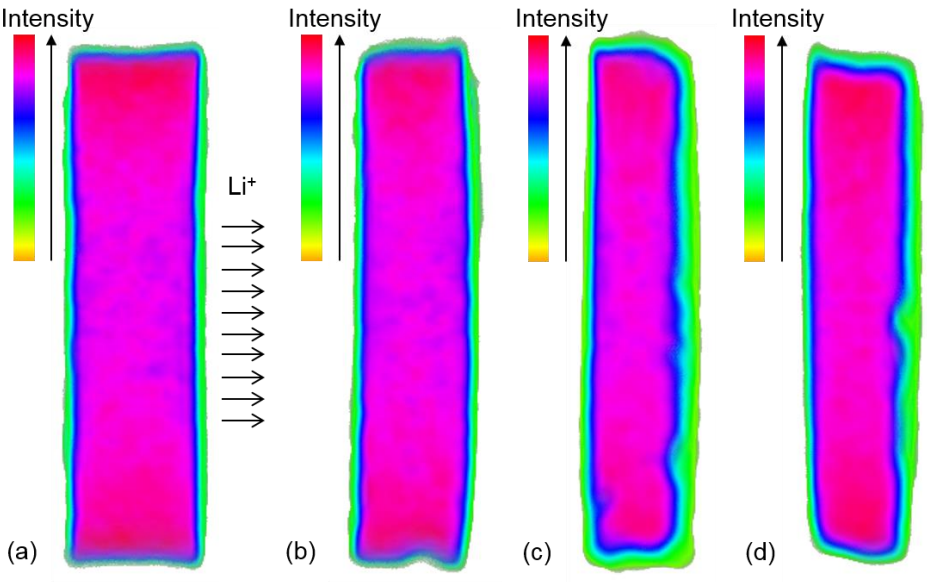

Figure 3.7. Cross-sectional views of reconstructed pseudo-color volume for Mg-50 wt.% Li alloys: (a) fresh electrode with no Li depletion, (b) with 9.72% Li depletion, (c) with 39.37% Li depletion and (d) with 42.73% Li depletion. Colors are assigned according to different attenuation intensities.

In Figure 3.6(b-d) and Figure 3.7(b-d), the regions that are colored as diffused green, blue and light purple show the combined result of the edge effect and the variation of Li concentration in that region. At the centers of samples, the Li distribution, as determined by imaging, is uniform. From Figure 3.6 and Figure 3.7, the qualitative variation of Li concentration profiles created by the delithiation steps can be clearly observed across the thickness. The Li concentration is relatively constant at the center, and starts to decrease after a certain point while approaching the active side. As Li depletion proceeds, the regions close to the active side, colored as green, blue and light purple are getting relatively thicker. This indicates that the Li concentration decreases in the region close to the active surface during the delithiation process.

In addition, thickness reduction along with Li depletion can be observed in both Figure 3.6 and Figure 3.7. In this case, the pseudo-color plots as shown are meant to demonstrate the general composition trends. Therefore the amount of thickness reduction is not showing precisely in this cross-sectional view. During the delithiation process, the alloy is getting thinned because the molar volume of the alloy decreases with a decrease in Li composition of the alloy. After each experiment, thickness measurements were made on delithiated samples to verify the electrode thinning evident in the imaging data. The average thickness values are listed in Table 3.3 to give an idea of how the amount of Li depleted affects the thickness of the electrode. These measurements were then used to find a thickness function for the variation of electrode thickness as a function of the time of delithiation. Figure 3.8 shows the thickness reduction data and the fitted lines. This thickness function will be used in the mathematical modeling of Li diffusion discussed in Section 3.3.4. A quantitative analysis of neutron imaging data will be discussed in Section 3.3.4.3.

Table 3.3 Thickness of Mg-70 wt.% Li sample before and after delithiation

Li depletion	Starting thickness (mm)	Final thickness (mm)
~10%	1.04	0.92
~20%	1.04	0.86
~30%	1.04	0.83
~40%	1.06	0.79

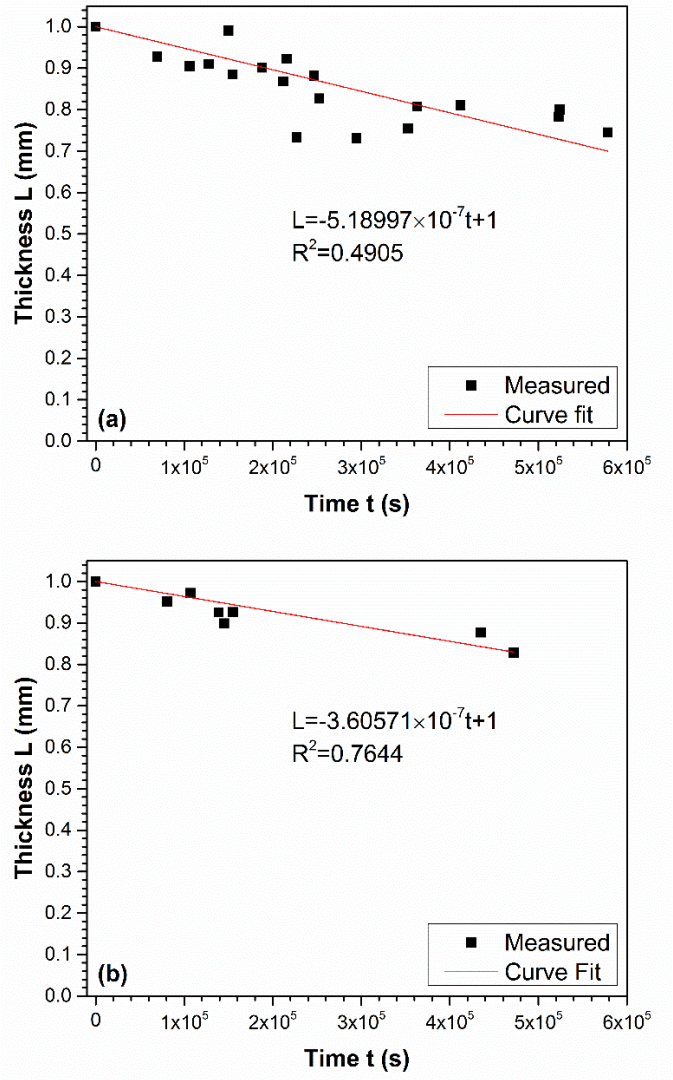

Figure 3.8. Curve fitting of thickness function for (a) Mg-70 wt.% Li alloy, (b) Mg-50 wt.% Li alloy.

3.3.4 Kinetic Model of Delithiation Process in Solid Li-Mg Electrodes

For Li-Mg alloy, the phase diagram (Figure 3.1) shows that at room temperature, a single phase BCC solid solution (β phase) exists over 11.5–100 wt.% Li in Li-Mg. At Li compositions <6 wt.%, HCP α phase is stable. Hence, when the Li gets depleted below 11.5 wt.% at the active surface, the β→α phase transition will occur. Such gradual β to α phase transitions has been investigated by Jagannathan et al., using XRD, recently [4]. Based on these, a diffusion controlled delithiation model has been developed here. The schematic drawing of how Li concentration changes along with the delithiation process is shown in Figure 3.9.

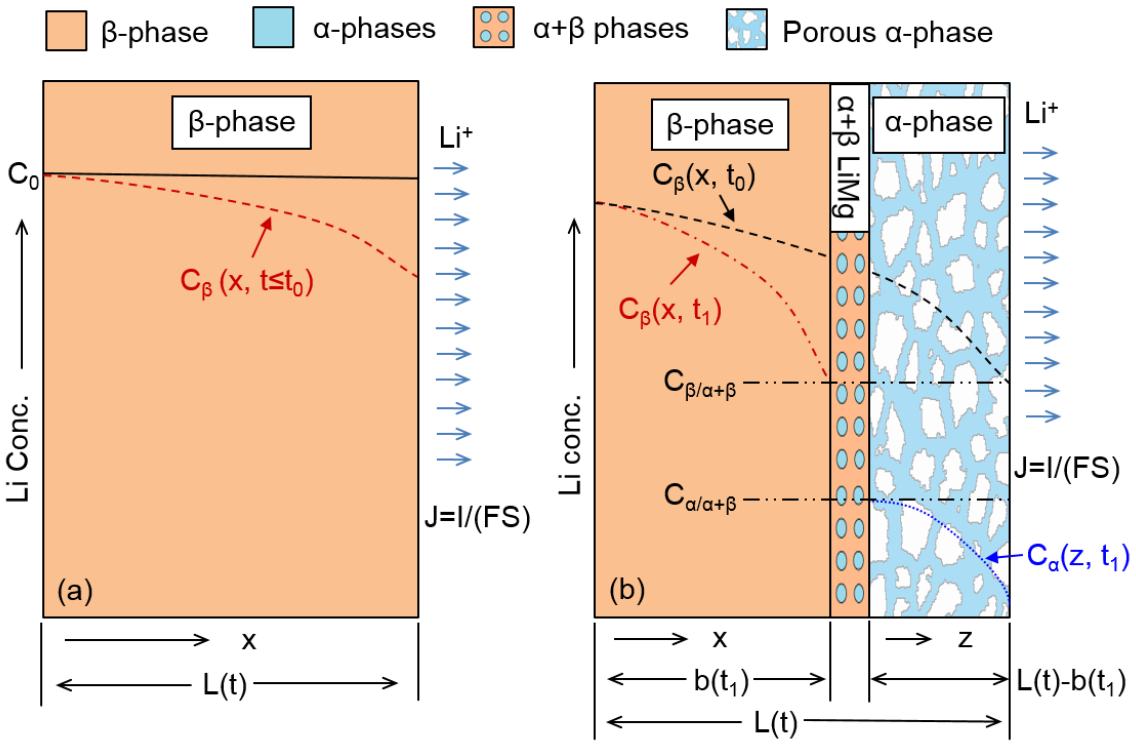

Figure 3.9. Schematic drawing of phase evolution and Li concentration profiles upon delithiation. (a) Li concentration profile (red dashed line) before Li surface concentration reaches $C_{\beta/\alpha+\beta}$. (b) Li concentration profile (red dash-dotted line and blue dotted line) after Li surface concentration drops below $C_{\beta/\alpha+\beta}$ leading to the presence of two-phase boundaries during the late parts of delithiation.

In Figure 3.9, the background colors are used to distinguish the three regions: β-phase region, α+β two-phase region and porous α-phase region. The Li concentration for the initial state, or before delithiation, is C_0, which is the alloy composition. The distance from the nonactive side is labeled as x, and it can vary from 0 to $L(t)$ (the thickness of electrode as a function of time as determined from thickness function in Figure 3.8). $C_{\alpha/\alpha+\beta}$ is the maximum possible concentration of Li in α-phase and $C_{\beta/\alpha+\beta}$ is the minimum possible concentration of Li in β-phase. J is the Li flux driven by the constant current applied at the active surface.

The nature of the phase transition and the boundary movement in Li-Mg alloy electrode can be described as follows. Before any Li depletion, only Li-rich β-phase will be present throughout the alloy electrode. After the Li depletion starts, the Li concentration at the surface continuously decreases with time. The dashed line in Figure 3.9(a) shows the schematic Li concentration profile within β-phase $C_\beta(x, t \leq t_0)$ after an arbitrary amount of Li depletion. With further delithiation, the Li concentration at the surface reaches the β→α phase transition point, $C_{\beta/\alpha+\beta}$, at time t_0. When further delithiation brings the Li concentration of the active surface below $C_{\beta/\alpha+\beta}$, the Li-most-lean β-phase (11.5 wt.%) and the Li-most-rich α-phase (6 wt.%) will coexist in a two-phase region at the active surface. However, because of the narrowness of the composition range (6-11.5 wt.%) in this two-phase region, and a relatively lower Li diffusivity in α-phase, the Li-most-lean β-phase will be consumed very quickly during delithiation and only α-phase will be left as a porous structure at the active side as shown in Figure 3.9(b). Thus the α+β two-phase region will be pushed away from the active surface rapidly and moves into the bulk during delithiation (shown as α+β region in Figure 3.9(b)).

In the following modeling section, this α+β region is treated as a phase boundary layer with zero thickness to simplify the calculation procedure. This is not expected to affect the results because the two-phase region moves to the left and will disappear after complete delithiation. As delithiation proceeds, the time-dependent Li concentrations in β and α phases are expressed as $C_\beta(x, t_1)$, where $t_1 = t\text{-}t_0$, and $C_\alpha(z, t_1)$, respectively. Here the variable z is the distance within the α phase. As the delithiation proceeds, the α+β phase boundary will move toward the nonactive side and this is described by the time-dependent position of boundary, $b(t_1)$. Depending how fast the Li is depleted from the bulk of the electrode, the thickness of α-phase region, $L(t)$-$b(t_1)$, on the active side, will vary. It is to be noted that the thickness, $L(t)$, is the function obtained from the curve fitting as shown in Figure 3.8. In the following discussion, L and b are used instead of $L(t)$ and $b(t_1)$ to simplify the writing of equations.

Based on the delithiation process described above, the transient Li concentration profiles as a function of delithiation time can be determined by solving Fick's second law with appropriate initial and boundary conditions [18]. Because of the complexity of phase transition, the solution needs to be divided into two segments, that is, before and after the β→α phase transition.

3.3.4.1 Li concentration profile before β→α phase transition

The schematic of transient Li concentration profile within β-phase of Li-Mg, during an arbitrary delithiation step, is illustrated in Figure 3.9(a). At any time, the concentration profile should satisfy Fick's second law

$$\frac{\partial C_\beta(x,t)}{\partial t} = D_\beta \frac{\partial^2 C_\beta(x,t)}{\partial x^2} \tag{3.1}$$

where x is the distance from nonactive side, D_β is the diffusivity of Li in β-phase and $C_\beta(x, t \le t_0)$ is the Li concentration in β-phase at x at time t ($t \le t_0$). The boundary and initial conditions are: (i) zero Li flux at the nonactive electrode surface, (ii) steady-state Li flux at the electrolyte/electrode interface under current I, and (iii) initial Li concentration is C_0 through the thickness of Li-Mg electrode. These conditions are specified by equations (3.2) -(3.4).

$$-D_\beta \left.\frac{\partial C_\beta}{\partial x}\right|_{x=0} = 0 \tag{3.2}$$

$$-D_\beta \left.\frac{\partial C_\beta}{\partial x}\right|_{x=L} = \frac{I}{FS} \tag{3.3}$$

$$C_\beta(x, t=0) = C_0 \tag{3.4}$$

where I is the current applied, F is Faraday's constant, S is the active surface area, L is the thickness of the electrode and C_0 is the initial concentration of this specific alloy. As we have discussed before (Section 3.3.3), the thickness of the electrode here decreases as a function of time due to Li depletion. Therefore, the time-dependent changes in electrode thickness, as shown in Figure 3.8, need to be included as well.

Equation (3.2) and (3.3) can be rewritten as

$$\left.\frac{\partial C_\beta}{\partial x}\right|_{x=0} = 0 \tag{3.5}$$

$$\left.\frac{\partial C_\beta}{\partial x}\right|_{x=L} = \frac{-I}{D_\beta FS} \tag{3.6}$$

For problems with complex boundary conditions such as the present one, solutions can be obtained using the method of separation of variables [19]. The general solution can be written as

$$C_\beta(x,t) = [A\cos(\lambda x) + B\sin(\lambda x)]\exp(-\lambda^2 D_\beta t) \tag{3.7}$$

where λ, A and B are to be determined using the conditions (3.4)-(3.6).

First, using the boundary condition (3.6) in Equation (3.7):

$$\left.\frac{\partial C_\beta}{\partial x}\right|_{x=L} = -A\lambda\sin(\lambda L)\exp(-\lambda^2 D_\beta t) = \frac{-I}{D_\beta FS} \tag{3.8}$$

Equation (3.8) is a flux boundary condition and can only be satisfied if $A\lambda\sin(\lambda L)=0$. In order to satisfy the boundary condition (3.6), an auxiliary function, $u(x, t)$, needs to be introduced in Equation (3.7), as

$$C_\beta(x,t) = [A\cos(\lambda x) + B\sin(\lambda x)]\exp(-\lambda^2 D_\beta t) + u(x,t) \tag{3.9}$$

Then the modification of Equation (3.8), in light of Equation (3.9), is

$$\left.\frac{\partial C_\beta}{\partial x}\right|_{x=L} = -A\lambda\sin(\lambda L)\exp(-\lambda^2 D_\beta t) + \left.\frac{\partial u}{\partial x}\right|_{x=L} = \frac{-I}{D_\beta FS} \tag{3.10}$$

The above equation can be satisfied when

$$\lambda = \frac{n\pi}{L} \tag{3.11}$$

and

$$\left.\frac{\partial u}{\partial x}\right|_{x=L} = \frac{-I}{D_\beta FS} \tag{3.12}$$

Using another boundary condition (3.5) in the modified general solution, Equation (3.9),

$$\left.\frac{\partial C_\beta}{\partial x}\right|_{x=0} = B\lambda \exp(-\lambda^2 D_\beta t) + \left.\frac{\partial u}{\partial x}\right|_{x=0} = 0 \tag{3.13}$$

This boundary condition can be satisfied simply when $B = 0$ and

$$\left.\frac{\partial u}{\partial x}\right|_{x=0} = 0 \tag{3.14}$$

The auxiliary function, $u(x, t)$, should also satisfy Fick's law as

$$\frac{\partial u}{\partial t} = D_\beta \frac{\partial^2 u}{\partial x^2} \tag{3.15}$$

Using the equations (3.12), (3.14) and (3.15), the function $u(x, t)$ is obtained as

$$u(x,t) = \frac{-I}{2D_\beta FSL} x^2 - \frac{I}{FSL} t \tag{3.16}$$

Substituting Equation (3.11), (3.16), and $B = 0$ into Equation (3.9), the obtained general form of $C_\beta(x, t)$ is

$$C_\beta(x,t) = \sum_{n=0}^{\infty} A_n \cos(\frac{n\pi}{L} x) \exp(-\frac{n^2\pi^2}{L^2} D_\beta t) - \frac{I}{2D_\beta FSL} x^2 - \frac{I}{FSL} t \tag{3.17}$$

In the above equation, the values of the coefficients A_n (n = 0, 1, 2…) can be derived from the initial condition (3.4), through Fourier series expansion. The final solution for Li concentration profile in single β-phase, thus obtained as:

$$C_\beta(x,t) = C_0 + \frac{IL}{6D_\beta FS} - \frac{I}{FSL}t - \frac{I}{2D_\beta FSL}x^2 + \frac{2IL}{D_\beta FS\pi^2}\sum_{n=1}^{\infty}\frac{(-1)^n}{n}\cos(\frac{n\pi}{L}x)\exp(-\frac{n^2\pi^2}{L^2}D_\beta t) \quad (3.18)$$

Equation (3.18) describes the Li concentration profile within β phase when Li is depleted under constant flux at the active side of the electrode.

3.3.4.2 Li concentration profile after β→α phase transition

3.3.4.2.1 Concentration profile in β-phase

The schematic of transient Li concentration profiles within the α and β phases, during an arbitrary delithiation step, during the later stages of delithiation, are illustrated in Figure 3.9(b). At any time, the concentration profile in β-phase should satisfy Fick's second law

$$\frac{\partial C_\beta(x,t_1)}{\partial t_1} = D_\beta \frac{\partial^2 C_\beta(x,t_1)}{\partial x^2} \quad (3.19)$$

with

$$t_1 = t - t_0 \quad (3.20)$$

where t_0 is the time when the surface Li concentration reaches $C_{\beta/\alpha+\beta}$. The boundary and initial conditions are: (i) zero Li flux at the nonactive electrode surface, (ii) fixed Li concentration in the Li-most-lean β phase at the β/α+β phase interface (x=b) is $C_{\beta/\alpha+\beta}$, and

(iii) initial Li concentration is $C_\beta(x,\ t=t_0)$, which is determined by previous step (Eqn. (3.18)). These conditions are specified as equations (3.21)-(3.23).

$$-D_\beta \left.\frac{\partial C_\beta}{\partial x}\right|_{x=0} = 0 \tag{3.21}$$

$$C_\beta(x=b, t_1) = C_{\beta/\alpha+\beta} \tag{3.22}$$

$$C_\beta(x, t_1=0) = C_\beta(x, t=t_0) \tag{3.23}$$

Using the variable separation method, solution for this problem should be in the form of

$$C_\beta(x,t_1) = [G\sin(\lambda_m x) + H\cos(\lambda_m x)]\exp(-\lambda_m{}^2 D_\beta t_1) + v(x,t_1) \tag{3.24}$$

where $v(x,\ t_1)$ is an auxiliary function introduced in advance.

Using the boundary condition (3.21) in Eqn. (3.24)

$$\left.\frac{\partial C_\beta}{\partial x}\right|_{x=0} = G\lambda_m \exp(-\lambda_m{}^2 D_\beta t_1) + \left.\frac{\partial v}{\partial x}\right|_{x=0} = 0 \tag{3.25}$$

This can be satisfied when $G = 0$ and

$$\left.\frac{\partial v}{\partial x}\right|_{x=0} = 0 \tag{3.26}$$

Thus, the general solution, Equation (3.24) can be rewritten as

$$C_\beta(x,t_1) = H\cos(\lambda_m x)\exp(-\lambda_m{}^2 D_\beta t_1) + v(x,t_1) \tag{3.27}$$

Using the other boundary condition (3.22) in Equation (3.27)

$$C_{\beta}(x=b,t_1) = H\cos(\lambda_m b)\exp(-\lambda_m{}^2 D_{\beta} t_1) + v(x=b,t_1) = C_{\beta/\alpha+\beta} \tag{3.28}$$

This can be satisfied when

$$\lambda_m = \frac{(2m+1)\pi}{2b} \tag{3.29}$$

and

$$v(x=b,t_1) = C_{\beta/\alpha+\beta} \tag{3.30}$$

The auxiliary function $v(x, t_1)$ should also satisfy Fick's law as

$$\frac{\partial v}{\partial t_1} = D_{\beta}\frac{\partial^2 v}{\partial x^2} \tag{3.31}$$

Using the equations (3.26), (3.30) and (3.31), $v(x, t_1)$ can be determined as

$$v(x,t_1) = C_{\beta/\alpha+\beta} \tag{3.32}$$

Substituting this in Equation (3.27), the general form of $C_{\beta}(x, t_1)$ is

$$C_{\beta}(x,t_1) = \sum_{m=0}^{\infty} H_m \cos(\lambda_m x)\exp(-\lambda_m{}^2 D_{\beta} t_1) + C_{\beta/\alpha+\beta} \tag{3.33}$$

The values of the coefficients H_m (m = 0, 1, 2…) can be derived from the initial condition (3.23), through Fourier series expansion. The final solution for the concentration profile in β-phase is thus obtained as

$$C_{\beta}(x,t_1)=\sum_{m=0}^{\infty}(H_{m1}-H_{m2}+H_{m3})\cos(\lambda_m x)\exp(-\lambda_m{}^2 D_{\beta}t_1)+C_{\beta/\alpha+\beta} \tag{3.34}$$

with

$$H_{m1}=\frac{2}{b}(C_0-C_{\beta/\alpha+\beta}+\frac{IL}{6D_{\beta}FS}-\frac{It_0}{FSL})[\frac{(-1)^m}{\lambda_m}] \tag{3.35}$$

$$H_{m2}=\frac{I}{bD_{\beta}FSL}[\frac{b^2(-1)^m}{\lambda_m}-\frac{2(-1)^m}{\lambda_m{}^3}] \tag{3.36}$$

$$H_{m3}=\frac{2IL}{6D_{\beta}FS\pi^2}\sum_{n=1}^{\infty}\frac{(-1)^n}{n^2}\exp(-\lambda_n{}^2 D_{\beta}t_0)\{\frac{\sin[(\lambda_n+\lambda_m)b]}{\lambda_n+\lambda_m}+\frac{\sin[(\lambda_n-\lambda_m)b]}{\lambda_n-\lambda_m}\} \tag{3.37}$$

$$\lambda_m=\frac{(2m+1)\pi}{2b} \tag{3.38}$$

$$\lambda_n=\frac{n\pi}{L} \tag{3.39}$$

Equation (3.34) describes the Li concentration profiles in the β phase layer after Li is depleted below $C_{\beta/\alpha+\beta}$ at the active surface. Thus, the solution represents the Li concentration profile in the β phase during the β/α+β phase boundary movement toward the nonactive side.

3.3.4.2.2 Concentration profile in α-phase

At a much later stage of delithiation, the relative location of β/α+β and α/α+β phase boundaries are as illustrated in Figure 3.9(b). In the actual modeling, to simplify the calculations, these two-phase boundaries are treated as a single phase boundary, with appropriate concentration limits, $C_{\beta/\alpha+\beta}$ and $C_{\alpha/\alpha+\beta}$. Now the task is to determine the

concentration profile in the α-phase. Using the same approach, the governing equation from Fick's law can be written as

$$\frac{\partial C_{\alpha}(z,t_1)}{\partial t_1} = D_{\alpha}\frac{\partial^2 C_{\alpha}(z,t_1)}{\partial z^2} \tag{3.40}$$

with

$$z = x - b \tag{3.41}$$

where b is the thickness of β-phase and z is the thickness of α-phase. As discussed in Section 3.3.3, b is a function of t_1. The boundary and initial conditions are: (i) constant Li concentration $C_{\alpha/\alpha+\beta}$ at the α/α+β phase interface, (ii) fixed Li flux at the electrolyte/electrode interface under current I, and (iii) initial Li concentration $C_{\alpha/\alpha+\beta}$ at t_1=0. These conditions are specified by equations (3.42)-(3.44).

$$C_{\alpha}(z=0,t_1) = C_{\alpha/\alpha+\beta} \tag{3.42}$$

$$-D_{\alpha}\left.\frac{\partial C_{\alpha}}{\partial z}\right|_{z=L-b} = \frac{I}{FS} \tag{3.43}$$

$$C_{\alpha}(z,t_1=0) = C_{\alpha/\alpha+\beta} \tag{3.44}$$

Using the variable separation method, the Li concentration function should be in the form of

$$C_{\alpha}(z,t_1) = [P\cos(\lambda_j z) + Q\sin(\lambda_j z)]\exp(-\lambda_j{}^2 D_{\alpha} t_1) + w(z,t_1) \tag{3.45}$$

where $w(z, t_1)$ is an auxiliary function introduced.

Using the boundary condition (3.42) in Equation (3.45),

$$C_{\alpha}(z=0,t_1) = P\exp(-\lambda_j{}^2 D_{\alpha} t_1) + w(z=0,t_1) = C_{\alpha/\alpha+\beta} \tag{3.46}$$

The above equation is satisfied when $P = 0$ and

$$w(z=0,t_1) = C_{\alpha/\alpha+\beta} \tag{3.47}$$

Using the other boundary condition (3.43) in Equation (3.45),

$$\left.\frac{\partial C_{\alpha}}{\partial z}\right|_{z=L-b} = Q\lambda_j \cos[\lambda_j (L-b)]\exp(-\lambda_j{}^2 D_{\alpha} t_1) + \left.\frac{\partial w}{\partial z}\right|_{z=L-b} = \frac{-I}{D_{\alpha} FS} \tag{3.48}$$

The above equation can be satisfied when

$$\lambda_j = \frac{(2j+1)\pi}{2(L-b)} \tag{3.49}$$

and

$$\left.\frac{\partial w}{\partial z}\right|_{z=L-b} = \frac{-I}{D_{\alpha} FS} \tag{3.50}$$

The auxiliary function $w(z, t_1)$ should also satisfy Fick's law as

$$\frac{\partial w}{\partial t_1} = D_{\alpha} \frac{\partial^2 w}{\partial z^2} \tag{3.51}$$

Thus, using the equations (3.47), (3.50) and (3.51), $w(z, t_1)$ can be determined as

$$w(z,t_1) = \frac{-I}{D_{\alpha} FS} z + C_{\alpha/\alpha+\beta} \tag{3.52}$$

Substituting this in Equation (3.45), the general form of $C_\alpha(z, t_1)$ can be written as

$$C_\alpha(z,t_1) = \sum_{j=0}^{\infty} Q_j \sin(\lambda_j z) \exp(-\lambda_j{}^2 D_\alpha t_1) - \frac{I}{D_\alpha FS} z + C_{\alpha/\alpha+\beta} \tag{3.53}$$

The values of the coefficients Q_j (j = 0, 1, 2…) can be derived from the initial condition (3.44), through Fourier series expansion. The final solution for the Li concentration profile in α-phase, thus obtained as

$$C_\alpha(z,t_1) = C_{\alpha/\alpha+\beta} - \frac{I}{D_\alpha FS} z + \frac{8(L-b)I}{D_\alpha FS\pi^2} \sum_{j=0}^{\infty} \frac{(-1)^j}{(2j+1)^2} \sin(\lambda_j z) \exp(-\lambda_j{}^2 D_\alpha t_1) \tag{3.54}$$

with

$$\lambda_j = \frac{(2j+1)\pi}{2(L-b)} \tag{3.55}$$

Equation (3.54) describes the Li concentration profiles in the α phase layer after Li is depleted below $C_{\alpha/\alpha+\beta}$ at the active surface.

Equation (3.34) and (3.54) give the Li concentration profiles in β and α phases, respectively. Thus, they provide the complete Li concentration profile across the electrode after β→α phase transition.

3.3.4.2.3 Determination of phase boundary position

As the delithiation proceeds, an infinitesimally thin α+β phase layer acts as phase boundary and moves toward the nonactive side of the electrode. The phase boundary movement can be determined from the flux balance at the phase boundary as

$$\frac{J_{\beta/\alpha+\beta} - J_{\alpha/\alpha+\beta}}{C_{\beta/\alpha+\beta} - C_{\alpha/\alpha+\beta}} = \frac{\Delta b}{\Delta t} = \frac{db}{dt} \tag{3.56}$$

with

$$J_{\beta/\alpha+\beta} = -D_{\beta} \left. \frac{\partial C_{\beta}}{\partial x} \right|_{x=b} \tag{3.57}$$

and

$$J_{\alpha/\alpha+\beta} = -D_{\alpha} \left. \frac{\partial C_{\alpha}}{\partial x} \right|_{z=0} \tag{3.58}$$

where $J_{\beta/\alpha+\beta}$ is the flux that leaves β-phase and $J_{\alpha/\alpha+\beta}$ is the flux that goes into α-phase and Δt is the time interval. In the calculations of concentration profiles, starting from the time (t_0) when Li depleted below $C_{\beta/\alpha+\beta}$ at the active surface, the boundary location $b(t)$ is determined and updated after each time step. The instantaneous value of $b(t)$ is used in Equation (3.34) and (3.54) to determine the concentration profiles in both β and α phase of any time during delithiation.

Similarly, L, as a function of t (see Section 3.3.3), is determined and updated after each time step using the same approach in the calculation of Li concentration profiles.

3.3.4.3 Simulation assessment

Figure 3.10(a) shows the cross-sectional SEM photograph of one Mg-70 wt.% Li alloy with ~30% Li depletion. The depletion of Li under electrochemical driving force resulted the porous structure observed. The porous structure originates from the active surface of the electrode and partly through the thickness of the electrode. The formation of such a structure could provide additional electrical path and ion transport path due to the increased

surface area which is in contact with electrolyte. This will significantly change the effective fraction of active surface area. It needs to be noted that the increased surface area should also be a function of time. However, approximation was made here to simplify the solution. In the concentration modeling part, which concerns mostly the heavily delithiated alloys (>15%), the surface region was assumed to be fully occupied by Li-most-lean α phase. Thus, the porosity at the active surface can be considered as constant approximately. Therefore, the effective flux density of Li depletion was modified accordingly. Figure 3.10(b) shows an illustration of how the porous structure will modify the effective area of the active surface. The porous structure as shown on the right can significantly increase the effective surface area. Since a constant current is applied, the effective Li depletion flux density will be lower. After adjusting the effective surface area with the assumption of 50% porosity, simulated Li concentration profiles were obtained with parameters listed in Table 3.4 for both Mg-70 wt.% Li and Mg-50 wt.% Li alloy electrodes.

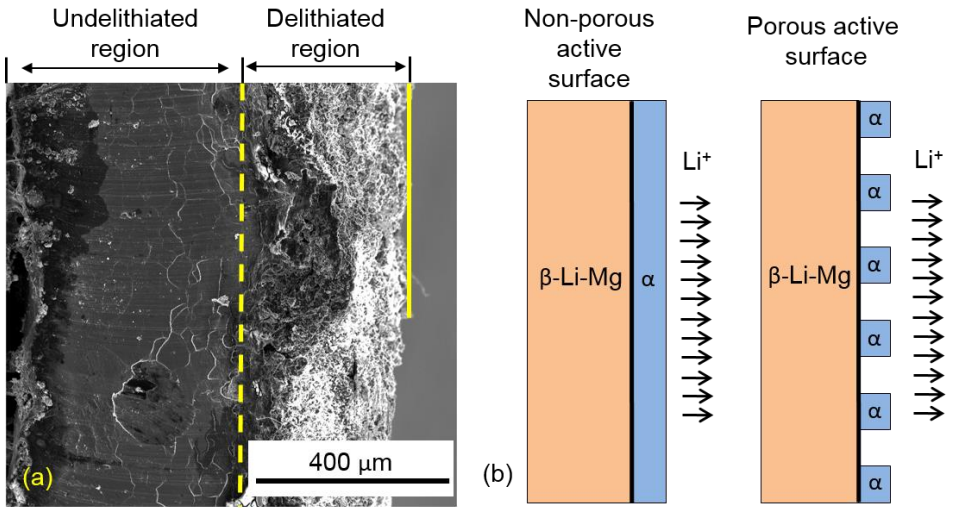

Figure 3.10. Porous structure formed upon delithiation. (a) SEM of a cross-sectioned Mg-70 wt.% Li alloy electrode with 32.3% Li depletion, the interface of the porous region and the nonporous electrode bulk is highlighted by a dashed line. (b) Schematic drawing of how porous structure will modify the active surface area, relative to a nonporous structure.

Table 3.4 List of parameters and their value used in the modeling

Parameters	Value
D_β, Li diffusion coefficient in β-phase	6×10^{-11} cm^2 s^{-1}
D_α, Li diffusion coefficient in α-phase	1×10^{-12} cm^2 s^{-1}
C_0(I), initial Li conc. in Mg-70 wt.% Li	0.0695 mol cm^{-3}
C_0(II), initial Li conc. in Mg-50 wt.% Li	0.0574 mol cm^{-3}
$C_{\beta/\alpha+\beta}$, Li conc. at β/α+β interface in β phase	0.0234 mol cm^{-3}
$C_{\alpha/\alpha+\beta}$, Li conc. at β/α+β interface in α+β phase	0.01125 mol cm^{-3}
I, constant current applied	0.064 mA
S, effective surface area	0.373 cm^2

The simulated Li concentration profiles and the experimental data from neutron tomography are shown in Figure 3.11 and Figure 3.12 for Mg-70 wt.% Li and Mg-50 wt.% Li alloys, respectively. The depth of edge effect in neutron imaging is estimated to be ~0.25 mm from the experimental Li concentration profiles at the nonactive side of the electrodes. In order to better visualize and compare the simulated and the experimental data, the regions affected by the edge effect are colored as blue in Figure 3.11 and Figure 3.12.

It can be seen that, for heavily delithiated samples (>15% Li depletion), the simulated Li concentration profiles agree very well with the imaging data as shown in Figure 3.11 and Figure 3.12. The predicted location of delithiated/undelithiated boundary (dashed line, ~325 μm away from the active surface) is in agreement with the observed boundary location as shown in Figure 3.10(a).

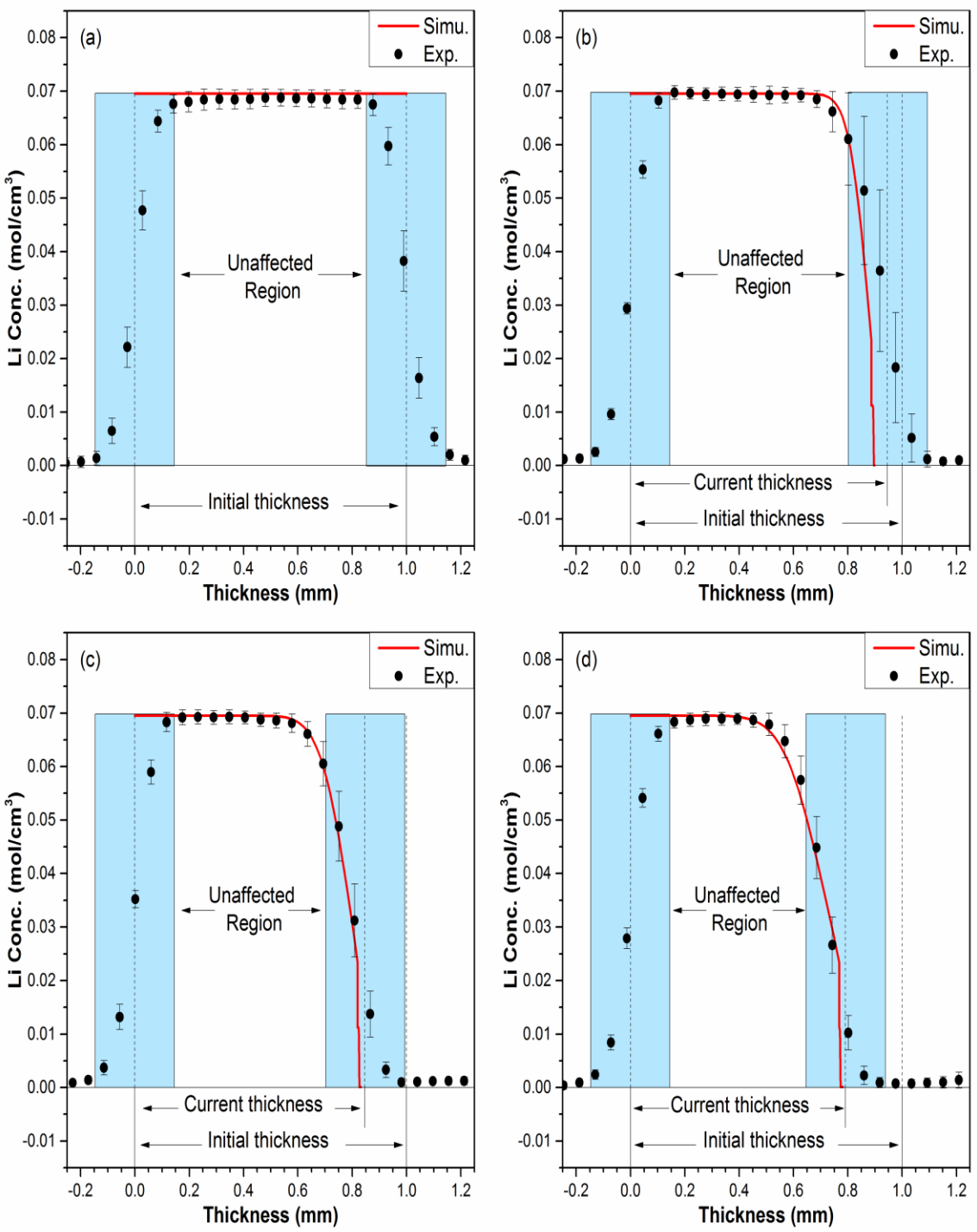

Figure 3.11. Simulation vs. experimental data for Mg-70 wt.% Li with, (a) 0% Li depletion, (b) 17.78% Li depletion, (c) 32.34% Li depletion and (d) 41% Li depletion (1.0 mm is the initial electrode/electrolyte interface where delithiation occurs). The regions that are affected by edge artifacts are colored in blue and the unaffected regions are marked.

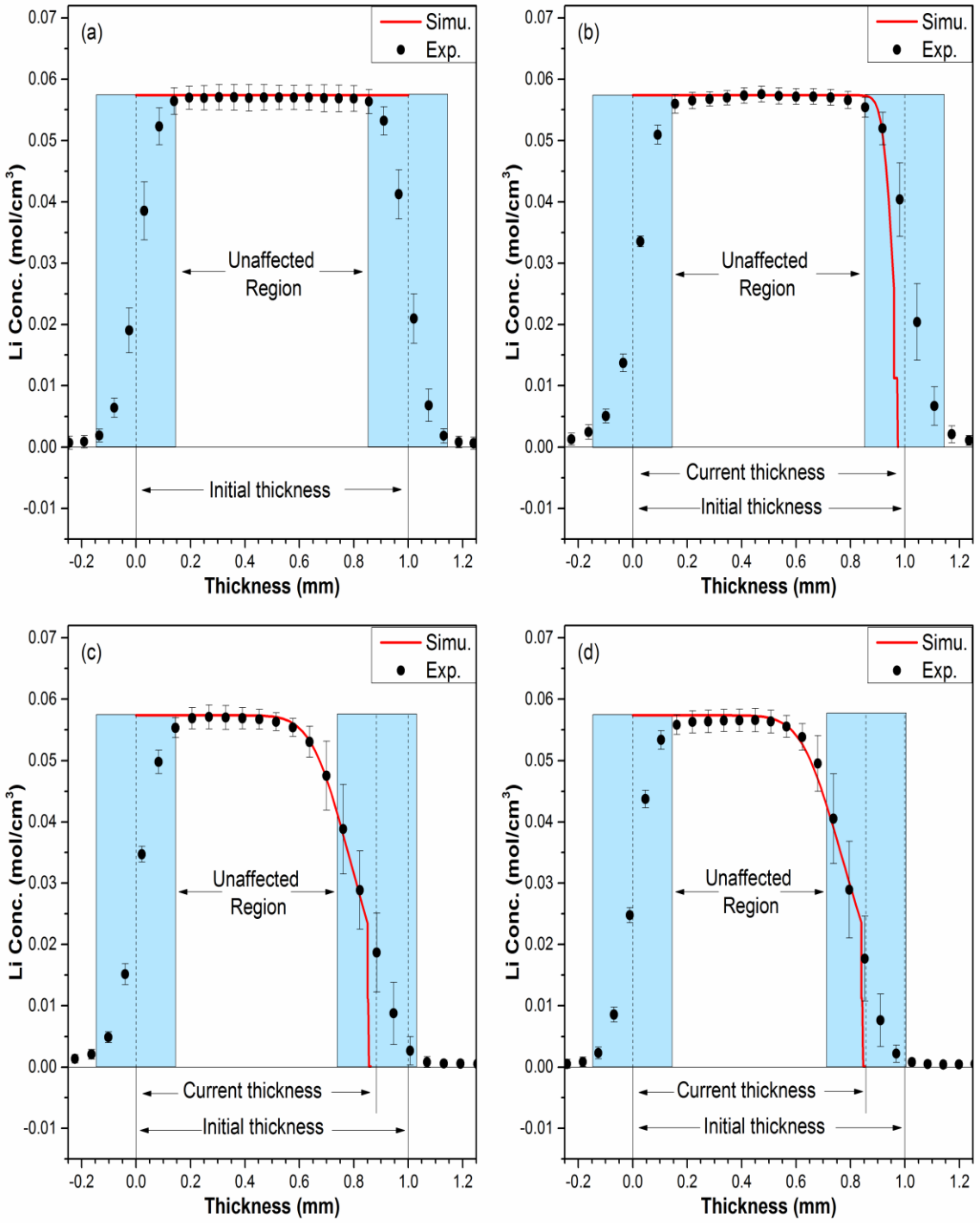

Figure 3.12. Simulation vs. experimental data for Mg-50 wt.% Li with, (a) 0% Li depletion, (b) 9.22% Li depletion, (c) 39.37% Li depletion and (d) 42.73% Li depletion (1.0 mm is the initial electrode/electrolyte interface where delithiation occurs). The regions that are affected by edge artifacts are colored in blue and the unaffected regions are marked.

In order to justify the values of Li diffusivities that were used in the model, chronoamperometry was performed on a cell composed of Li-Mg alloy, separator and metallic Li foil by applying a constant voltage (0.65 V vs. Li/Li^+). The current as a function of time was then recorded for further analysis. For simple redox reaction, such as Li/Li^+ couple, under a constant electrochemical driving force (controlled voltage), the current measured depends on the rate at which the Li^+ diffuses. Then the diffusivity of the interested species can be obtained with the help of the Cottrell equation [20]

$$I = \frac{qFS'C_0}{\pi^{1/2}t^{1/2}} D^{1/2} \tag{3.59}$$

where I is the measured current, q is the charge transfer number of the electroactive species (Li), F is the Faraday's constant, S' is the active surface area, C_0 is the initial concentration of Li in the alloy, D is the diffusion coefficient of Li in the Li-Mg alloy and t is time. S' here is the actual flat surface area with no modification for porosity because of the limited Li depletion during the short period of the measurement.

It is important to note that the diffusivity obtained from the Cottrell equation is contributed by both the transport of Li^+ in Li-Mg alloy and the transport of Li^+ in the electrolyte. Since the diffusivity of Li^+ in the liquid is normally several magnitudes higher than the one in the solid, the obtained diffusivity can be considered mainly contributed by the diffusion of Li^+ in the alloy. Thus, from the slope of the I vs. $t^{-1/2}$ plot (Figure 3.13), the diffusion coefficient of Li^+ in β phase of solid Mg-70 wt.% Li alloy is estimated to be about 2×10^{-10} cm^2 s^{-1}. This is very close to the Li diffusivity value used in the modeling, which is 6×10^{-11} cm^2 s^{-1}.

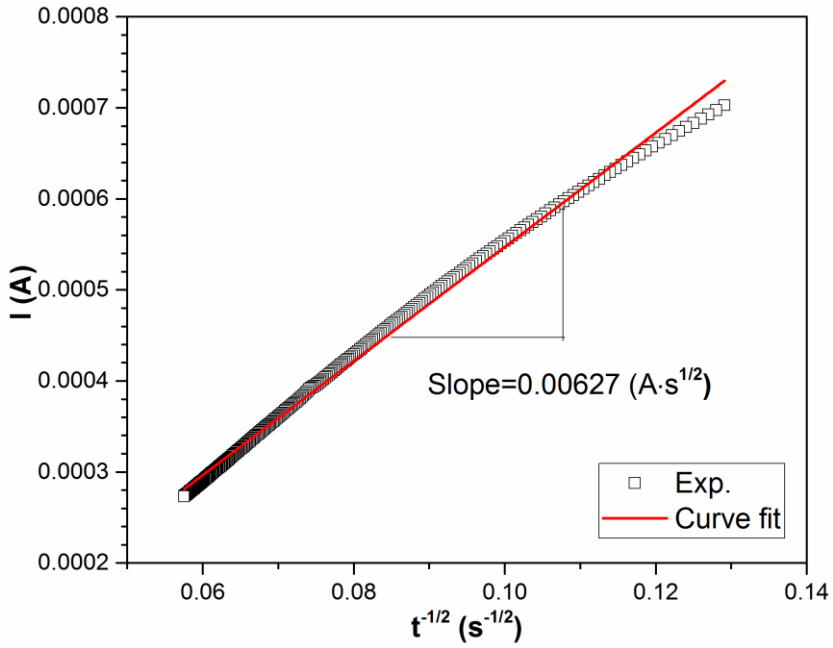

Figure 3.13. Cottrell plot of the data obtained from chronoamperometric test for Mg-70 wt.% Li alloy.

3.4 Summaries

(1) Li-Mg alloy electrodes with two different compositions were successfully prepared in the laboratory. The delithiation process was successfully controlled to achieve electrodes with different depths of Li for neutron imaging.

(2) Using computed neutron tomography, Li spatial distributions in the bulk Li-Mg alloy electrodes with different depths of delithiation were determined. The variations in Li concentration profiles along the direction of delithiation have been successfully captured. This technique has been proven to be a very powerful tool to noninvasively and quantitatively study bulk distribution of elements that are highly interactive with neutrons, such as Li in Li-ion batteries and H in fuel cells.

(3) An analytical diffusion model for the delithiation of Li-Mg alloy, including the β→α phase transition, has been developed. It considers exactly the β-phase and porous α-

phase structure before and after phase transition using appropriate initial and boundary conditions as well as flux-controlled boundary movement. The simulated Li concentration profiles are consistent with the concentration profiles determined from imaging data. And the agreement is good within the region where edge effects are not present.

(4) The Li diffusivity (6×10^{-11} cm^2 s^{-1}) that was used in modeling is very close to the value determined by an independent chronoamperometry experiment ($\sim2\times10^{-10}$ cm^2 s^{-1}).

3.5 References

[1] S. Liu, J. Yang, L. Yin, Z. Li, J. Wang, Y. Nuli, Electrochimica Acta, 56 (2011) 8900-8905.

[2] Z. Shi, M. Liu, D. Naik, J.L. Gole, Journal of Power Sources, 92 (2001) 70-80.

[3] W.-J. Zhang, Journal of Power Sources, 196 (2011) 877-885.

[4] M. Jagannathan, K.S.R. Chandran, Journal of the Electrochemical Society, 160 (2013) A1922-A1926.

[5] J. Nanda, H. Bilheux, S. Voisin, G.M. Veith, R. Archibald, L. Walker, S. Allu, N.J. Dudney, S. Pannala, The Journal of Physical Chemistry C, 116 (2012) 8401-8408.

[6] J.B. Siegel, X. Lin, A.G. Stefanopoulou, D. Gorsich, in: American Control Conference (ACC), 2011, IEEE, 2011, pp. 376-381.

[7] L.G. Butler, B. Schillinger, K. Ham, T.A. Dobbins, P. Liu, J.J. Vajo, Nuclear Instruments and Methods in Physics Research Section A: Accelerators, Spectrometers, Detectors and Associated Equipment, 651 (2011) 320-328.

[8] G.V. Riley, D.S. Hussey, D. Jacobson, ECS Transactions, 25 (2010) 75-83.

[9] V.F. Sears, Neutron News, 3 (1992) 26-37.

[10] A.A. Nayeb-Hashemi, J.B. Clark, A.D. Pelton, Bulletin of Alloy Phase Diagrams, 5 (1984) 365-374.

[11] L. Santodonato, H. Bilheux, B. Bailey, J. Bilheux, P. Nguyen, A. Tremsin, D. Selby, L. Walker, Physics Procedia, 69 (2015) 104-108.

[12] L. Crow, L. Robertson, H. Bilheux, M. Fleenor, E. Iverson, X. Tong, D. Stoica, W.T. Lee, Nuclear Instruments and Methods in Physics Research Section A: Accelerators, Spectrometers, Detectors and Associated Equipment, 634 (2011) S71-S74.

[13] M.D. Abràmoff, P.J. Magalhães, S.J. Ram, Biophotonics International, 11 (2004) 36-43.

[14] M. Dierick, B. Masschaele, L.V. Hoorebeke, Measurement Science and Technology, 15 (2004) 1366-1370.

[15] A.S. Tremsin, E.H. Lehmann, N. Kardjilov, M. Strobl, I. Manke, J.B. McPhate, J.V. Vallerga, O.H.W. Siegmund, W.B. Feller, Journal of Instrumentation, 7 (2012) C02047.

[16] J. Jakubek, Nuclear Instruments and Methods in Physics Research, Section A: Accelerators, Spectrometers, Detectors and Associated Equipment, 576 (2007) 223-234.

[17] M. Kang, H.Z. Bilheux, S. Voisin, C.L. Cheng, E. Perfect, J. Horita, J.M. Warren, Nuclear Instruments and Methods in Physics Research Section A: Accelerators, Spectrometers, Detectors and Associated Equipment, 708 (2013) 24-31.

[18] M. Jagannathan, K.S.R. Chandran, Journal of Power Sources, 247 (2014) 667-675.

[19] H.S. Carslaw, J.C. Jaeger, Conduction of heat in solids, Oxford University Press Inc., New York, 1986.

[20] C.M.A. Brett, A.M.O. Brett, Electrochemistry: principles, methods, and applications, Oxford University Press Inc., New York, 1993.

CHAPTER 4

STUDY OF THE LI SPATIAL DISTRIBUTION IN V2O5 CATHODE UNDER DIFFERENT C-RATES BY COMPUTED NEUTRON TOMOGRAPHY

(Manuscript in preparation)

4.1 Introduction

The transition metal oxides are very widely used as cathode material for secondary lithium-ion batteries. Vanadium pentoxide (V_2O_5) is one of them that has been intensively studied in recent years. It is advantageous because of its stability, relative safety, low cost, ease of synthesis and high theoretical capacity (440 mAh g^{-1}) compared with typical commercial cathode materials (273 mAh g^{-1} for $LiCoO_2$) [1-5]. However, the intrinsic low-diffusion coefficient of lithium ions (~10^{-12} cm^2 s^{-1}) [6] and poor electronic conductivity (10^{-2} to 10^{-3} S cm^{-1}) [7] in crystalline vanadium oxide (V_2O_5) greatly limited the performance in some practical applications which require charge/discharge in short time. It is widely known that the high charge/discharge rate will lead to capacity fading of a battery [8]. However it is not quite clear how these Li ions will distribute spatially in a bulk cathode and lead to capacity loss.

Computed tomography and various image process techniques are very powerful techniques to study the spatial features noninvasively. Because of the small scattering length of Li with X-rays, neutron tomography comes into our sight because of the high absorption cross-section for natural Li. Recently, neutron computed tomography was successfully used to map Li spatial distribution [9-12] in bulk battery electrodes. Gray scale radiographs called projections are captured and recorded by a scintillator based on the transmitted neutron counts. The gray scale value recorded can be described by Beer-Lambert law, $I = I_0 \exp(-\Sigma \mu_i x_i)$, where I_0 and I are the incident and the transmitted intensity for a given neutron wavelength, respectively, and μ_i is the total attenuation coefficient (including absorption and scattering) of element, i, and x_i is the effective thickness of the element on the neutron path. The attenuation coefficient μ_i is given by $\mu_i = \sigma_{\mathrm{tot,i}} N_A c_i$, where

$\sigma_{tot,i}$ is the total neutron cross-section for the element, N_A is Avogadro's number, c_i is the molar concentration [9]. Thus, the difference in attenuation intensity can provide the information of how concentration varies for certain element involved.

Table 4.1 lists the thermal neutron scattering and absorption cross-section data from NIST (National Institute of Standard and Technology) [13] for the elements involved in this study. The neutron scattering cross-section is the sum of coherent and incoherent cross-section. The sum of scattering and absorption cross-sections contributes to the total cross-section, $\sigma_{tot,i}$. From Table 4.1, it can be seen that the total cross-section of V (10.18 barns), O (4.23219 barns), Al (1.734 barns) and Ar (1.358 barns) are significantly less than that of natural Li (71.87 barns). This leads to the large difference in neutron attenuation coefficient of Li with respect to other elements and makes the spatial mapping of Li mapping feasible.

In this work, three-dimensional (3D) neutron computed tomography has been used to map the Li distribution in bulk V_2O_5 after charge/discharge the commercially available cells, VL621, under different c-rates. For each cell, the plot of attenuation intensity along the thickness direction also has been obtained from the imaging data for further analysis.

Table 4.1 Neutron scattering and absorption cross-sections in barns (10^{-24} cm^2)

Element	Coherent cross-section $\sigma_{coh}(\lambda)$	Incoherent cross-section $\sigma_{inc}(\lambda)$	Scattering cross-section $\sigma_{scatt}(\lambda)$	Absorption cross-section $\sigma_{abs}(\lambda)$	Total cross-section $\sigma_{tot}(\lambda)$
Li	0.454	0.92	1.37	70.5	71.87
V	0.0184	5.08	5.1	5.08	10.18
O	4.232	0.0008	4.232	0.00019	4.23219
Al	1.495	0.0082	1.503	0.231	1.734
Ar	0.458	0.225	0.683	0.675	1.358

4.2 Materials and Experimental Procedure

4.2.1 Sample Preparation

In this work, VL621 coin cells purchased from Panasonic were used to study Li spatial response to different charge/discharge rates. The technical specifics of this type of coin cells are listed in Table 4.2. The huge difference between charge and discharge current (200 μA and 10 μA) needs to be noted. After receiving the coin cells, charging (delithiation of V_2O_5) was first performed on each cell to eliminate the self-discharge effect on Li spatial distribution during storage. In this charging process, 100 μA was chosen as current, and the cut-off voltage was set to 3.45 V. In the followed sample preparation, two c-rates, C/5 (300 μA, which can fully discharge a cell in 5 hours) and C/10 (150 μA, which can fully discharge a cell in 10 hours) were used to obtain the samples listed in Table 4.3. The electrochemical cycling was performed using Keithley 2401 source-meter.

Table 4.2 Specifics of VL621 coin cell

Cathode	V_2O_5
Anode	Li-Al alloy
Capacity	1.5 mAh
Discharge rate	10 μA
Standard charge current	200 μA
Size/dimension	6.8 mm (dia.) × 2.2 mm (thickness)

Table 4.3 Cycling conditions for coin cell

Sample number	Discharge	Charge
C/10	C/10	–
C/5	C/5	–
C/10_C/10	C/10	C/10
C/5_C/5	C/5	C/5

4.2.2 Neutron Computed Tomography (CT) and Data Visualization

Neutron CT was performed at the CG-1D Neutron Imaging Facility at the High Flux Isotope Reactor (HFIR), Oak Ridge National Laboratory, USA. Figure 4.1(a) is the schematic of the instrument setup at the beamline and Figure 4.1(b) shows how the samples were mounted on the stage for neutron characterization.

Neutrons are generated by fission reaction in the 85 MW reactor core. Thermal neutrons scatter from the beryllium reflector and reach a supercritical hydrogen moderator with a temperature of 17 K. This provides a source of cold neutrons with increased flux between 4 and 12 Å. The CG-1D imaging beamline sits at the end of the cold guide 1 neutron guide system and provides neutrons with wavelengths between 0.8 and ~ 6 Å, with a peak around 2.6 Å.

After flying through a pinhole, neutrons are collimated using a series of beam scrapers. A 50 μm ^{6}LiF/ZnS scintillator converts the transmitted neutron into light that is recorded by a charge-coupled device (CCD) camera [14, 15]. A gray-scale 2D projection based on neutron transmission intensity is saved as raw data. For volume reconstruction, the sample is mounted on a rotation stage which rotates through 180° (an extra 3° angle coverage is normally needed for filtered-back projection reconstruction), collecting over a thousand radiographs. In this work, each projection was taken in rotation steps of 0.2° with 90 s exposure time. Postprocessing of the raw data was completed using *ImageJ* [16] to correct high/low gray scale pixels and background noise. From the recorded projections data, the electrode volume was successfully reconstructed by filtered-back-projection (FBP) method using *Octopus* [17]. The 3D visualization of the image and data analysis was done using *VisIt* [18].

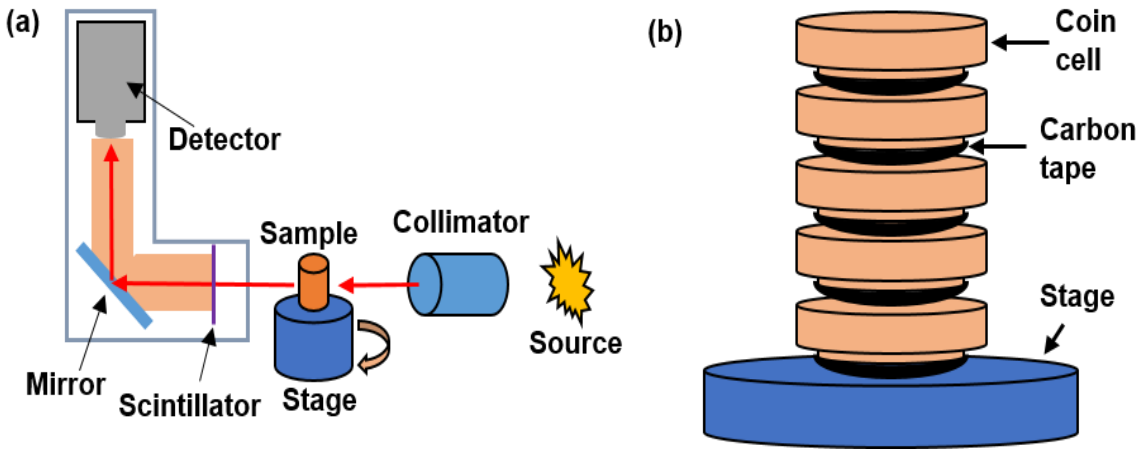

Figure 4.1. Schematic drawings of (a) neutron imaging set up at CG-1D and (b) how sample was mounted during characterization.

4.3 Results and Discussion

The potential vs. capacity profiles during charging/discharging of coin cells under selected c-rates (C/5 and C/10) are shown in Figure 4.2. It can be seen that, in the discharge cycle, the same amount of Li has intercalated with V_2O_5 under both C/10 and C/5. In the following charge cycle, the higher c-rate results in about 0.2 mAh capacity loss. It can be explained that, under higher c-rate or higher current density, the higher extraction flux leads to the lower Li concentration at electrode surface, and thus the cell potential would decrease and reach cut-off voltage faster than the one with lower c-rate.

In order to locate the V_2O_5 cathode inside each cell in the computed neutron tomography, a coin cell was disassembled and the dimensions of components were measured. A schematic drawing of the cross-sectional view of the coin cell is shown in Figure 4.3(a). The dimensions for each component are also marked in this graph. Further, the V_2O_5 region has been divided into three regions as shown in Figure 4.3(b) for convenience in data analysis and discussion.

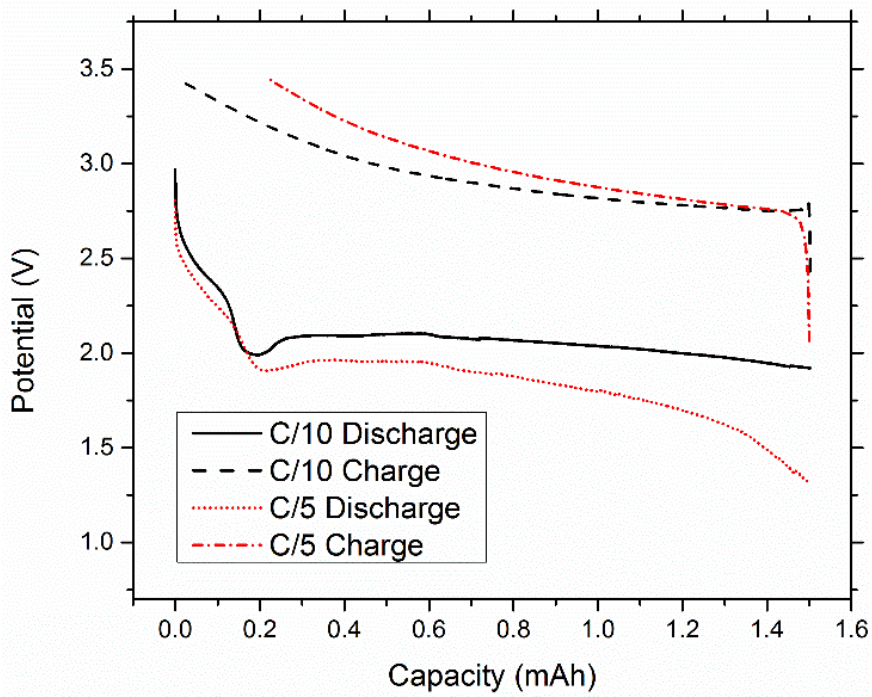

Figure 4.2. Potential vs. capacity curves of the charge and discharge cycle at C/5 and C/10 (the current for C/5 is 300 μA).

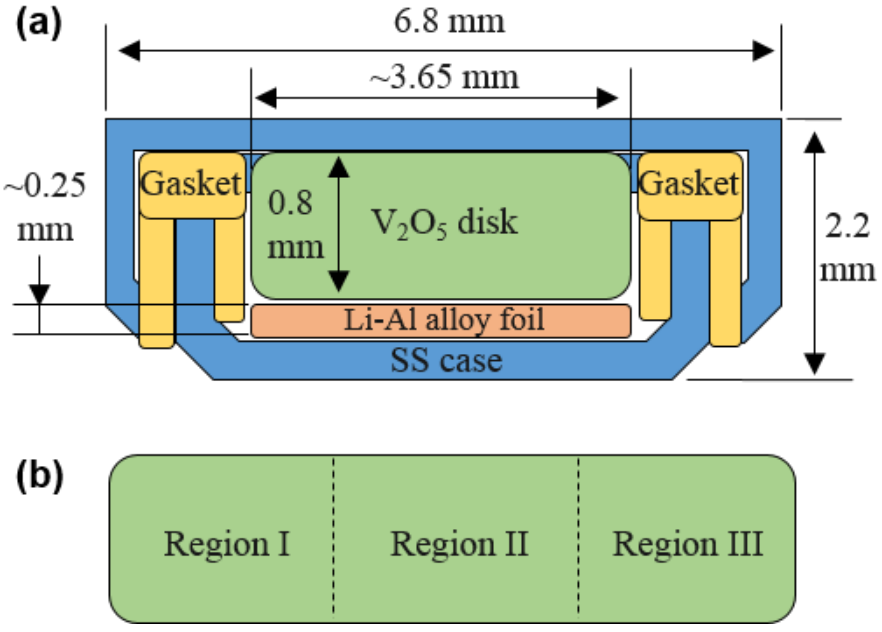

Figure 4.3. Schematic drawings of VL621 cell. (a) Cell components and their dimensions in a cross-sectional view and (b) the location of three selected regions inside the V_2O_5 cathode for further analysis.

Figure 4.4(a-d) shows the cross-sectional views at the center of each sample from computed neutron tomography. In these figures, the region of V_2O_5 cathodes can be located with help from Figure 4.3(a). The color scale bar on the left (Figure 4.4) scales the attenuated intensity of neutron beam, which represents the Li concentration from low to high in the V_2O_5 region. In these pseudo-color plots, the color contrast has been adjusted to better visualize the difference in Li concentration (shown as yellow color).

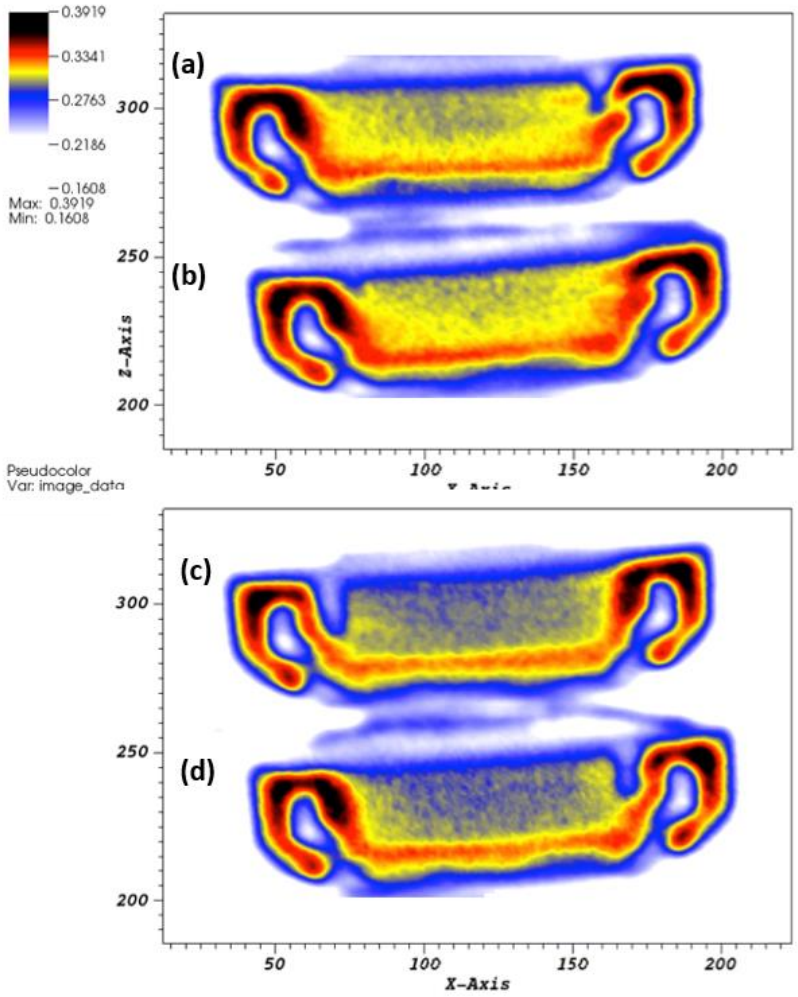

Figure 4.4. Cross-sectional pseudo-color plots obtained at the center location of the cell (a) discharged at C/5, (b) discharged at C/10, (c) discharged and charged at C/5 and (d) discharged and charged at C/10.

It can be seen that, after discharging (lithiation of V_2O_5), Li bulk distribution is more uniform under C/10 (Figure 4.4(a)) than the one under C/5 (Figure 4.4(b)). Additionally, in the cell discharged under C/5 (Figure 4.4(a)), the center top location of V_2O_5 clearly shows less Li concentration than the cell discharged under C/10 (Figure 4.4(b)). The cells after followed charging (delithiation of V_2O_5) are shown in Figure 4.4(c) and (d). In these two cells, the Li bulk distributions are relatively uniform in both cathodes. But it can still be noted that slightly less Li contents reside in V_2O_5 after cycling under C/10, as expected.

In order to better understand the rate effect on Li spatial distribution, the plots of attenuation intensity versus thickness for regions I, II and III are shown in Figure 4.5. The cell components have been highlighted (blue for SS casing, green for V_2O_5 cathode and light orange for Li-Al anode) based on the dimensions obtained from the disassembled coin cell and the locations determined by finding the reflection point in the second derivative of intensity plot. In this work, the intensity plot of the region where Li-Al anode sits was ignored due to the small thickness of Li-Al anode and the high neutron scattering from the adjacent polymer separator. In Figure 4.5(a) and (b), it can be seen that the Li concentration is higher in V_2O_5 cathode which is discharged at lower c-rate (C/10) than the one discharged at higher c-rate (C/5). It is consistent with the previous observation of pseudo-color plot as shown in Figure 4.4(a) and (b). We also noticed that, in the region close to the electrolyte/cathode interface, there is not much concentration difference, but in the bulk, which is away from the active surface, lower Li concentration can be seen in the one discharged under C/5. This suggests that, lithiation of V_2O_5 firstly occurs at the interface and Li starts to diffuse towards the other side due to the Li concentration gradient. Because of the relatively short distance for Li transport at the region close to the electrolyte/cathode

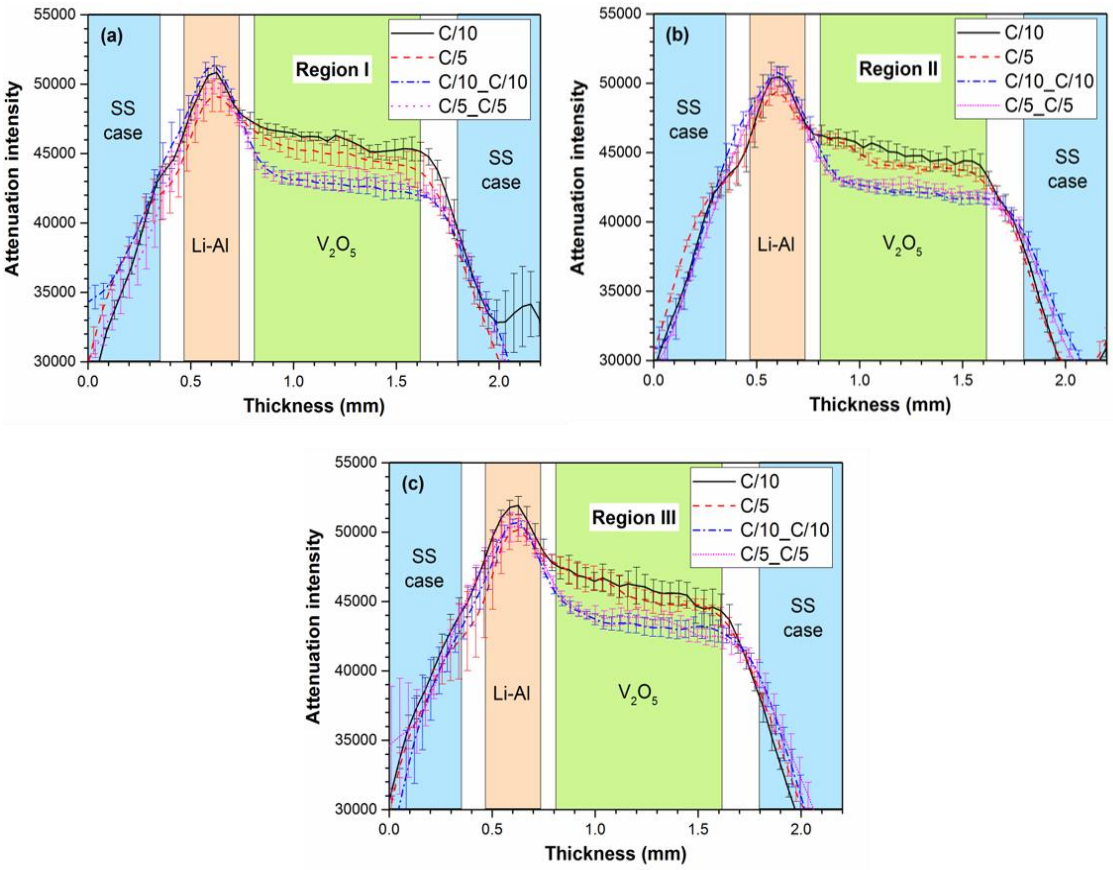

Figure 4.5. Attenuation intensity vs. thickness plots of the cells cycled at C/5 and C/10 in (a) Region I, (b) Region II and (c) Region III.

interface, the difference in Li concentration is small. However, at the region away from the interface, the transport of Li from the surface to the inner bulk requires more time. If the transport rate of Li from the surface to the inner bulk was not fast enough, the Li contents will accumulate in the region close to active surface. Therefore, the sites where Li^+ can reside at the surface of V_2O_5 becomes limited and the rate of Li^+ intercalation slows down. Under the fixed Li insertion flux (fixed current, C/5), the transport rate of Li^+ ions exceed the rate that Li^+ can be intercalated, dendrite formation and other side reaction may occur. This can explain why the Li concentration is lower in the bulk V_2O_5 after being lithiated

under C/5. However, due to the limited spatial resolution of neutron tomography, the Li dendrites were not observed.

In Figure 4.5(c) and (d), it can be seen that at the region close to the electrolyte/cathode interface, the Li concentrations are very close for both cells cycled under C/10 and C/5. However, the Li concentration at the inner bulk of V_2O_5 cathode, which is cycled under C/5, is higher than the one lithiated at lower c-rate (C/10). It is consistent with the previous observation of pseudo-color plot as shown in Figure 4.4(c) and (d). This can also be explained by the limitation of Li transport. Because of the relatively short distance for Li transport at the region close to the electrolyte/cathode interface, the delithiation of V_2O_5 in both cells occurs similarly and the final difference in Li concentration is small. However, at the region away from the interface, the transport of Li from the inner bulk to the surface requires more time. If the transport rate of Li to the surface was not fast enough to match the extraction flux, the Li concentration in the region close to the active surface will decrease and the potential will quickly reach the cut-off voltage even through some of Li still reside in the bulk. And the amount of Li remained is proportional to the c-rate applied.

4.4 Summaries

Qualitative Li spatial distribution in the bulk V_2O_5 cathodes, which are charged/discharged under two different c-rates (C/5 and C/10), has been successfully mapped by computed neutron tomography. The attenuation intensity vs. thickness plots obtained from CT data clearly show the effect of applied c-rate on the Li distribution at different location inside V_2O_5 cathodes. It can be seen that, with a faster c-rate applied during the lithiation of V_2O_5, less Li inserted the cathode and the Li concentration in the bulk is significantly lower than the one lithiated at slower c-rate. During the delithiation of

V_2O_5, with faster c-rate applied, the amount of Li extracted is less and the bulk Li concentration is higher than the one delithiated at slower c-rate. Non-uniform distribution of Li from the active surface to the bulk of cathode has also been due to the relatively low diffusivity of Li in V_2O_5 (10^{-12}-10^{-13} cm^2 s^{-1}) [19]. Thus, computed neutron tomography has proved to be a very powerful tool to noninvasively study bulk distribution of element that is highly interactive with neutrons, such as Li in Li-ion batteries.

4.5 References

[1] A. Pan, J.-G. Zhang, Z. Nie, G. Cao, B.W. Arey, G. Li, S.-q. Liang, J. Liu, Journal of Materials Chemistry, 20 (2010) 9193-9199.

[2] E.A. Olivetti, K.C. Avery, I. Taniguchi, D.R. Sadoway, A.M. Mayes, Journal of the Electrochemical Society, 155 (2008) A488-A493.

[3] S.-L. Chou, J.-Z. Wang, J.-Z. Sun, D. Wexler, M. Forsyth, H.-K. Liu, D.R. MacFarlane, S.-X. Dou, Chemistry of Materials, 20 (2008) 7044-7051.

[4] M.S. Whittingham, Y. Song, S. Lutta, P.Y. Zavalij, N.A. Chernova, Journal of Materials Chemistry, 15 (2005) 3362-3379.

[5] S.H. Lee, P. Liu, C.E. Tracy, D.K. Benson, Electrochemical and Solid-State Letters, 2 (1999) 425-427.

[6] T. Watanabe, Y. Ikeda, T. Ono, M. Hibino, M. Hosoda, K. Sakai, T. Kudo, Solid State Ionics, 151 (2002) 313-320.

[7] J. Muster, G.T. Kim, V. Krstić, J.G. Park, Y.W. Park, S. Roth, M. Burghard, Advanced Materials, 12 (2000) 420-424.

[8] J. Li, E. Murphy, J. Winnick, P.A. Kohl, Journal of Power Sources, 102 (2001) 294-301.

[9] J. Nanda, H. Bilheux, S. Voisin, G.M. Veith, R. Archibald, L. Walker, S. Allu, N.J. Dudney, S. Pannala, The Journal of Physical Chemistry C, 116 (2012) 8401-8408.

[10] J.B. Siegel, X. Lin, A.G. Stefanopoulou, D. Gorsich, in: American Control Conference (ACC), 2011, IEEE, 2011, pp. 376-381.

[11] L.G. Butler, B. Schillinger, K. Ham, T.A. Dobbins, P. Liu, J.J. Vajo, Nuclear Instruments and Methods in Physics Research Section A: Accelerators, Spectrometers, Detectors and Associated Equipment, 651 (2011) 320-328.

[12] G.V. Riley, D.S. Hussey, D. Jacobson, ECS Transactions, 25 (2010) 75-83.

[13] V.F. Sears, Neutron News, 3 (1992) 26-37.

[14] L. Santodonato, H. Bilheux, B. Bailey, J. Bilheux, P. Nguyen, A. Tremsin, D. Selby, L. Walker, Physics Procedia, 69 (2015) 104-108.

[15] L. Crow, L. Robertson, H. Bilheux, M. Fleenor, E. Iverson, X. Tong, D. Stoica, W.T. Lee, Nuclear Instruments and Methods in Physics Research Section A: Accelerators, Spectrometers, Detectors and Associated Equipment, 634 (2011) S71-S74.

[16] M.D. Abràmoff, P.J. Magalhães, S.J. Ram, Biophotonics International, 11 (2004) 36-43.

[17] M. Dierick, B. Masschaele, L.V. Hoorebeke, Measurement Science and Technology, 15 (2004) 1366-1370.

[18] H. Childs, E. Brugger, B.J. Whitlock, J.S. Meredith, S. Ahern, K. Bonnell, M. Miller, G.H. Weber, C. Harrison, D. Pugmire, T. Fogal, C. Garth, A. Sanderson, E.W. Bethel, M. Durant, D. Camp, J.M. Favre, O. Rubel, P. Navratil, M. Wheeler, P. Selby, VisIt: An End-User Tool For Visualizing and Analyzing Very Large Data, in: High Performance Visualization: Enabling Extreme-Scale Scientific Insight, Chapman and Hall/CRC, 2012, pp. 357-372.

[19] F. Lantelme, A. Mantoux, H. Groult, D. Lincot, Journal of the Electrochemical Society, 150 (2003) A1202-A1208.

CHAPTER 5

PREPARATION AND EVALUATION OF SI POWDER ANODE AND DESIGN OF IN SITU ELECTROCHEMICAL CELL FOR NEUTRON STUDY

5.1 Introduction

With the potential to offer the highest theoretical Li-storage capacity (4200 mAh/g), Si is one of the most promising material for anodes of Li-ion batteries. But the ~300% volume change makes it really difficult to avoid the cracking and delamination, which occur along with the lithiation of Si. This could greatly facilitate the degradation of a cell because of the irreversible capacity loss and the internal resistance increase[1-4].

A lot of effort has been made to accommodate such high volume change, nanosizing is one of the most effective ways. Arrays of wires in nanoscale dimensions can allow quick relaxation of stress. Therefore, the cracking of Si in bulk material can be avoided with appropriately nanostructured Si. Such anode can achieve as high as ~3000 mAh/g after ~100 cycles under a relatively moderate cycling rate [4, 5]. Also, amorphous silicon has been found to have better performance than crystalline Si by avoiding the anisotropic volume expansion[6-11]. Amorphous thin film with thickness of 50 nm exhibits excellent reversibility and high capacity (200 cycles, ~3500 mAh/g) [12]. Although high capacity and good reversibility have been obtained by various nanostructuring techniques, it is very difficult to extend such performance to larger scale. Therefore, a lot of research has focused on the studies of powder or composite electrode, due to the simplicity of synthesis and the relatively low cost [13-17].

In this work, nanosized Si powder electrodes with relatively high capacity and good cyclic performance were focused to fabricate by electrochemically roughening Cu substrate, adjusting the mass loading, current density and milling process. The findings from this work can offer insights as to how to obtain Si powder electrode with relatively high capacity and good cyclability in the context of Li-ion batteries. An in situ neutron

diffraction cell has been designed and fabricated and is promising to be used to characterize the unclear phase transitions during the initial lithiation/delitathiation cycles of Si powder electrode. Such understanding of Si crystalline/amorphous phase transitions upon lithiation could help the future electrode structuring and battery design.

5.2 Experimental Procedure

5.2.1 Nanosized Powder Preparation

Raw Si powder (purity >99%) with particle size in the range from 1 to 5 μm was purchased from Atlantic Equipment Engineers. A unique high energy dual-drive planetary mill (HE-DPM) was operated at 12 G to prepare nanosized Si powder. The milling jar is shown in Figure 5.1.

Figure 5.1 Stainless steel canister for high energy ball milling.

In the milling process, two sizes of chrome steel balls purchased from Glen Mills Inc. were used. The size of small balls is 5.56 mm (7/32 inches) in diameter and the size of big balls is 9.525 mm (3/8 inches) in diameter. Small balls weighing about 440 g and big balls weighing about 440 g were mixed and used as milling media. About 40 g of purchased Si powder was loaded into the milling jar inside an argon filled glovebox with <0.1 ppm O_2 and <0.1 ppm H_2O. The milling time was controlled to 30 min. The milling jar, which has an inner volume of ~160 mL, was sealed by a Vito-type O-ring, which kept the inside atmosphere inert during the milling process.

5.2.2 Electrode Preparation

A powder mixture containing nanosized Si powder, carbon black (CB) and sodium carboxymethyl cellulose (CMC binder) in the weight ratio of 80:12:8, was introduced into a Pyrex vial inside an argon-filled glove box. After transferring the vial out of the glove box, eight WC balls (4 balls with 5.56 mm in diameter and 4 balls with 9.525 mm in diameter) and buffer solution (1 mL of 0.173 M citric acid + 0.074 M KOH at pH = 3) were introduced with minimum exposure to air. The mixture was then milled using a roller at 70 rpm for 2 h to get a well dispersed slurry. The obtained slurry was then cast onto a copper substrate (current collector) using a doctor blade. These substrates were dried for 2 hours under argon at room temperature, and then for 12 hours under vacuum at 120 °C. Electrodes with 9.525 mm in diameter (~0.96 cm^2) were obtained by punching the substrate.

5.2.3 Substrate Preparation

In the initial lithiation/delithiation trials of these electrodes, which were cast on the unmodified Cu substrate, delamination of Si from the current collector was observed even

after the first cycle. To solve this issue, an electrochemical method was introduced to roughen the surface of the Cu substrates. A three-electrode one-compartment electrochemical cell (schematic drawing of the set-up is shown in Figure 5.2) was used for the roughening process. It contains a rectangular copper substrate (50 µm thick, ~15 cm^2) as the working electrode, a stainless steel grid (SS316, 30 mesh, ~15 cm^2) as the counter electrode and a saturated calomel electrode (SCE) as the reference electrode. In the solution of 1M NaOH, the copper substrate was cycled 3000 times at 10 V/s between -1.75 and 1V vs. Hg_2Cl_2. After such electrochemical treatment, the modified Cu substrate was rinsed with deionized water and transferred into a furnace for the reduction process. The furnace was kept at 300 °C for 3 hours while the gas mixture of Ar/5% H_2 (1 atm) flowed. The morphological characterization and composition analysis of the electrochemically treated Cu substrate were performed using Hitachi S-4800 scanning electron microscope (SEM).

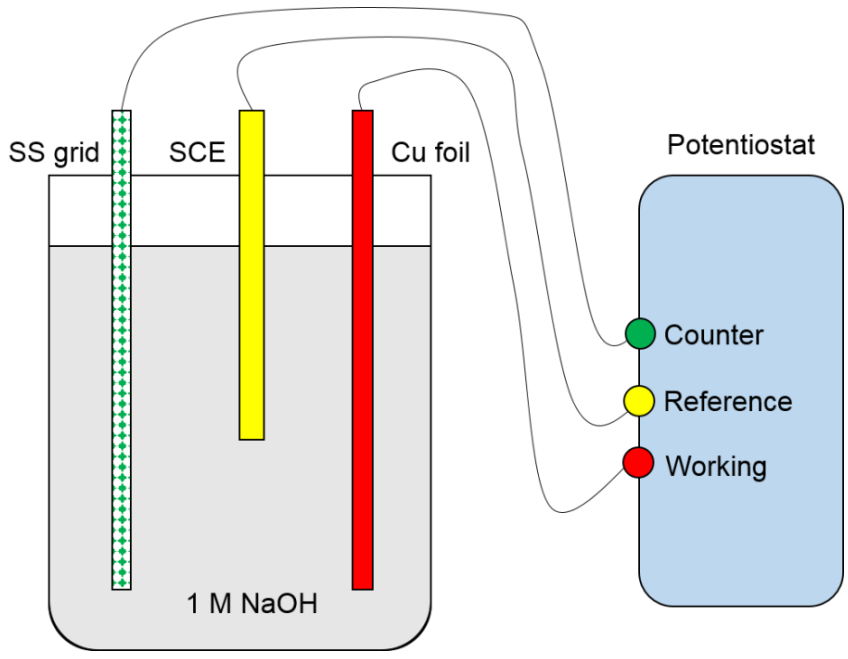

Figure 5.2 Schematic drawing of the set-up for electrochemical roughening.

5.2.4 Lithiation/Delithiation Cycling of Si Powder Electrodes

Circular electrodes with 9.525 mm in diameter (~0.96 cm^2) obtained by punching were used in the lithiation/delithiation experiments. Disks punched from metallic Li foil (99.9%, Alfa Aesar) with 0.75 mm in thickness and 12.7 mm in diameter were used as both counter electrode and reference electrode. The electrolyte containing 1M $LiPF_6$ solution (MTI Corp. Richmond, CA) in 1:1:1 ratio of EC (ethylene carbonate): DMC (dimethyl carbonate): DEC (diethyl carbonate) was used. A Si powder electrode, a Celgard 2400 polypropylene separator (soaked with electrolyte) and a Li foil were sandwiched into a two-electrode Swagelok cell inside an argon-filled glove box. The details of each sample including the mass loading and the cycling parameters are listed in Table 5.1. The cell cycling was performed using a Keithley 2401 source-meter with a voltage window of 0.005-1 V (vs. Li/Li^+). It is noted that the current densities listed in Table 5.1 can also be converted in the terms of c-rate (~C/24 for the current density of 150 mA/g), which is commonly used in battery research to describe how many hours it takes for charging/discharging the specific capacity. And the specific capacity, C, here is calculated on the basis of the mass of active material using the following equation:

$$C = 3580\ (\text{mAh/g}) \times 0.73\ (\text{ratio of Si in the mixture}) \times \text{total mass of loading (g)} \tag{5.1}$$

Table 5.1 Sample parameters of Si powder electrodes

Sample name	Mass loading of Si (mg/cm^2)	Current density for initial 2 cycles (mA/g)	Current density for the followed cycles (mA/g)
S1	0.76	75	150
S2	1.22	75	150
S3	1.52	150	150
S4	3.05	150	150

5.3 Results and Discussion

Figure 5.3 shows the SEM photographs of the Si nanopowder after high-energy ball milling under argon atmosphere. It can be seen that the particle sizes are around 100 nm and the Si particles tend to form micron-sized agglomerates.

The surface morphologies of the as-received and the electrochemically modified Cu substrate are shown in Figure 5.4. This confirms the formation of the nanosized needles on the Cu substrate after the electrochemical treatment. During one cycle of the electrochemical roughening, Cu was firstly oxidized as Cu^{2+} and then was reduced to deposit as $Cu(OH)_2$ at the surface. After many cycles, $Cu(OH)_2$ needles were formed because of the minimized energy while depositing along the preferred crystallographic planes.

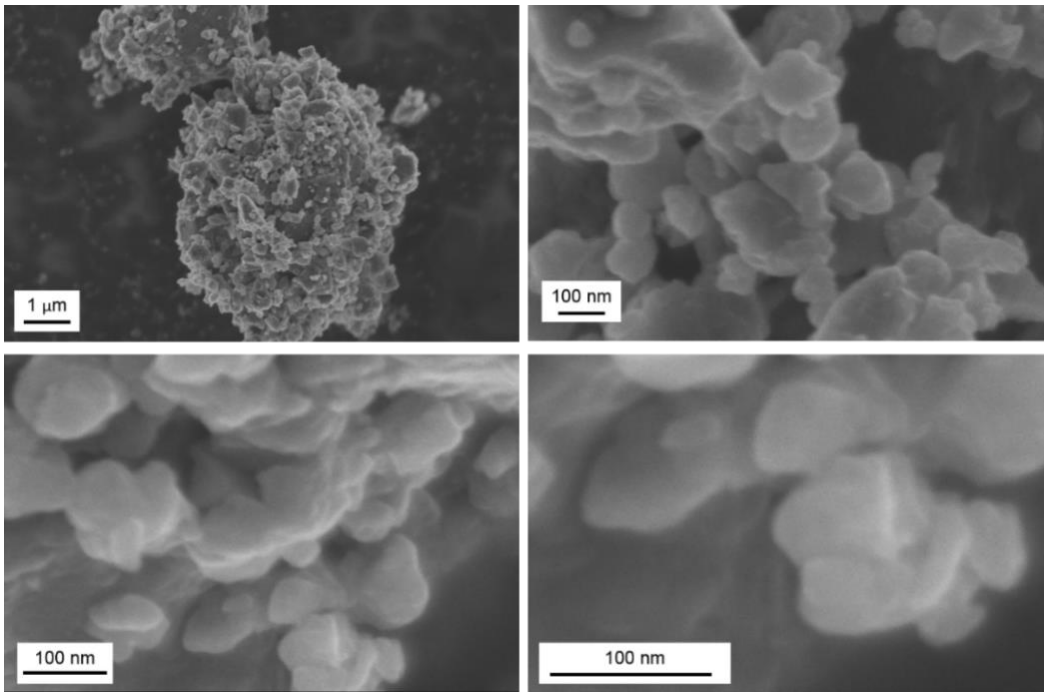

Figure 5.3 SEM photographs of Si powder.

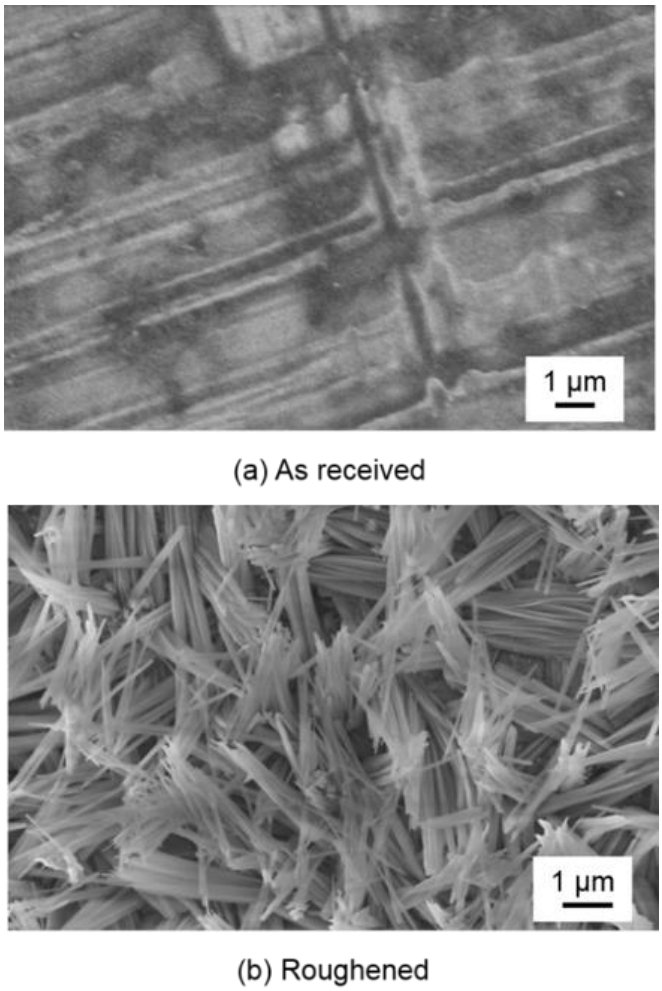

Figure 5.4 SEM photographs of (a) the as-received and (b) the electrochemically roughened Cu substrate.

In order to obtain substrate with only Cu needles, the reduction of $Cu(OH)_2$ was performed in a furnace with Ar/5% H_2 flowing. The morphologies of before and after reduction process have been characterized and shown in Figure 5.5. The energy dispersive analysis of X-rays (EDAX) was also performed to confirm the reduction of $Cu(OH)_2$. The results are shown in Figure 5.6. Thus, the electrochemically roughened substrate with ~2 μm long Cu nanoneedles had been obtained successfully and it was then used to replace the plain Cu foil during the preparation of Si nanopowder electrode.

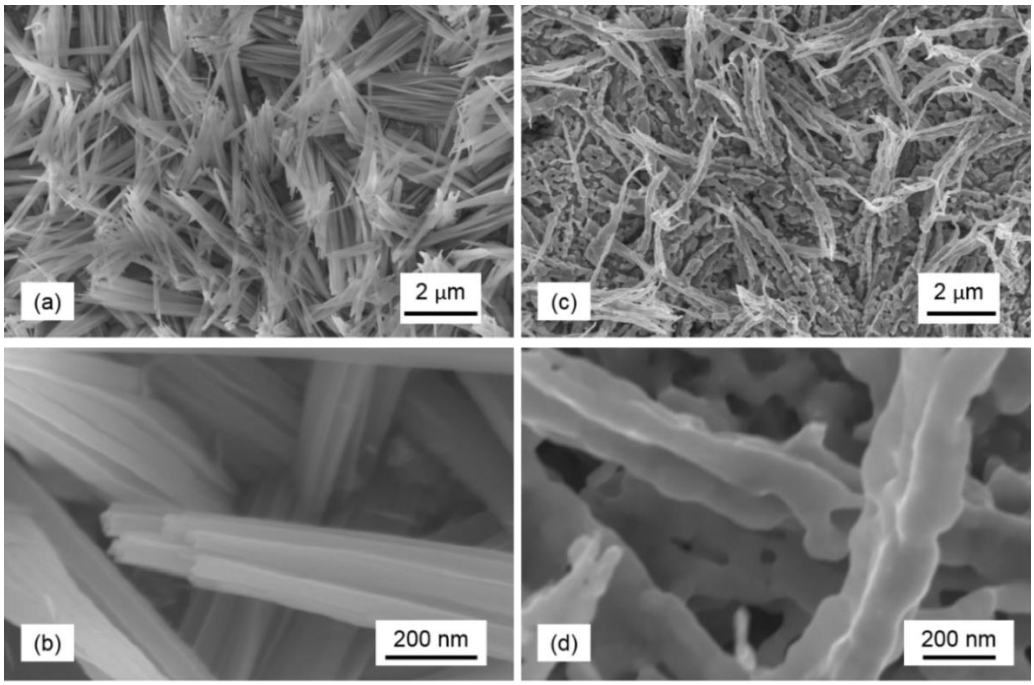

Figure 5.5 SEM photographs of roughened Cu substrate. (a) and (b) show different magnification of Cu substrate surface before annealing. (c) and (d) show different magnification of Cu substrate surface after annealing.

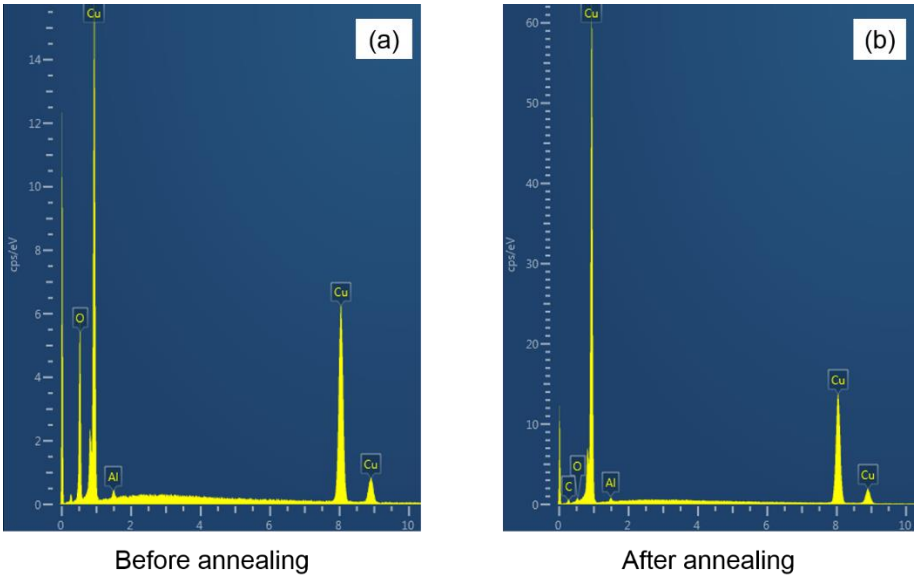

Figure 5.6 EDAX analysis of roughened Cu substrate. (a) Before annealing. (b) After annealing.

In order to study the effects of mass loading and cycling conditions on the performance of a cell, the prepared electrodes, with the parameters as listed in Table 5.1, were tested. The results are presented in the plot of capacity versus cycle number as shown in Figure 5.7. In this plot, the gravimetric capacity is calculated on the basis of Si weight. It can be seen that, by reducing the mass of loading from 3.05 g/cm^2 to 1.53 g/cm^2, the reversible capacity after 25 cycles increased from ~100 mAh/g to ~400 mAh/g. Furthermore, by limiting the current density to the half for only the initial 2 cycles, the capacity of Si was greatly improved to around 1200 mAh/g after 20 cycles.

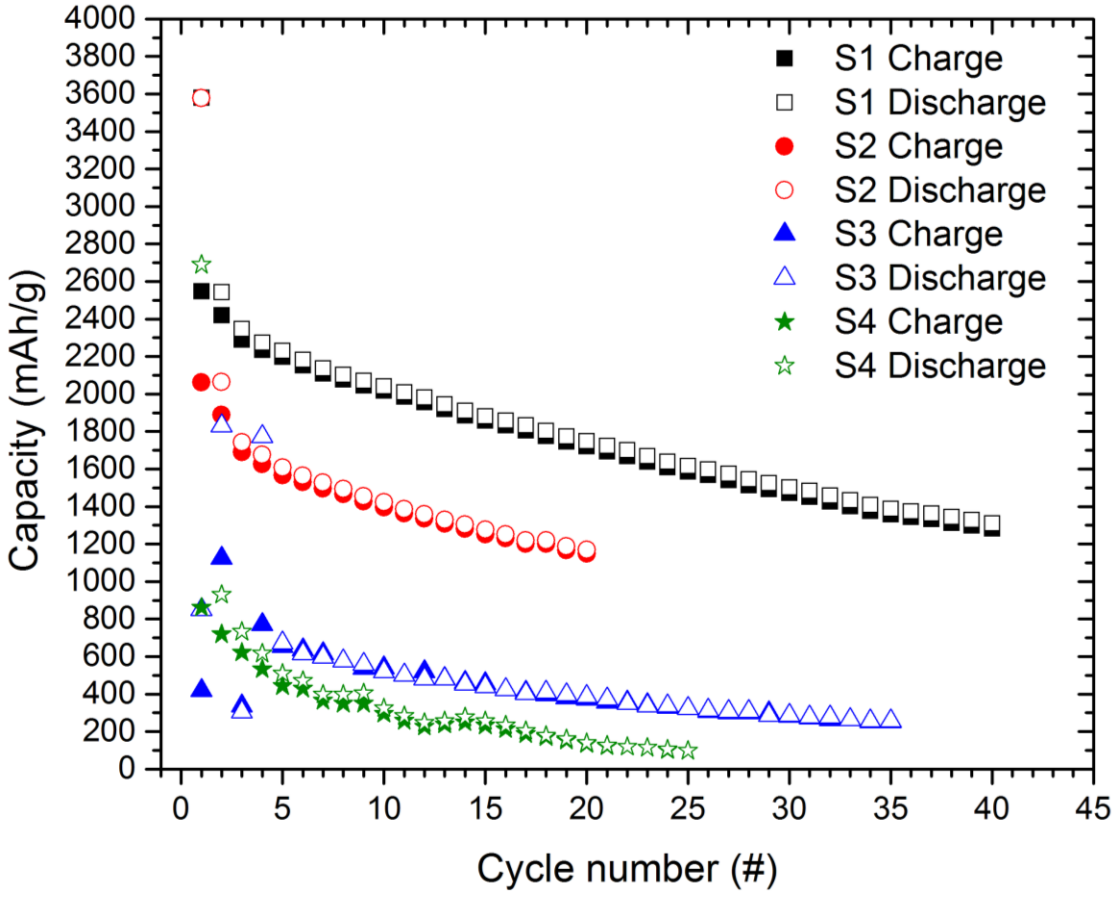

Figure 5.7 Capacity versus cycle number plot. The capacity is calculated based on the mass of active material Si.

A similar cycling condition was also applied for the other sample with less loading mass (0.76 g/cm^2). Very high reversible capacity of ~2500 mAh/g was observed for the initial delithiation cycle. And in the following 40 cycles, the capacity could maintain above 1300 mAh/g in both delithiation and lithiation. Such reversible capacity is a reasonable high value while comparing to the value obtained with similarly slurry casting approach [18]. The result here provides insight into how the loading mass and the initial current density applied will affect the overall performance of Li-ion batteries.

It has been reported in recent studies [19-21] that, during the first lithiation cycle, the crystalline Si gets amorphized into Li_xSi phase. And this a-Li_xSi phase is found to recrystallize into $Li_{15}Si_4$ at the point of reaching full capacity. In the reverse reaction, $Li_{15}Si_4$ will convert into Li_xSi amorphous phase instead of crystalline Si. This phase transition is suspected to be reversible in each following cycle. However, in the typical potential versus capacity curves obtained in this work (see Figure 5.8), an intriguing voltage plateau, which appears to correspond to a two-phase reaction region, was observed only during the first and second delithiation, and the characteristics of the followed delithiation curves change dramatically. This suggests that some unknown phase transitions might be occurring at/after the second delithiation.

Therefore, XRD was performed on the samples which were both cycled to ~0.42 V in different delithiation cycles. The results are shown in Figure 5.9. It can be seen that the crystallinity of Si has been destroyed during the first lithiation cycle of Si as expected. However, due to the low X-ray scattering cross-section of Li, the presence of other phases, such as $Li_{15}Si_4$, was not able to be captured. Also, the possible short range ordering of Li in Si lattice cannot be investigated. Thus the amorphorization needs to be further studied.

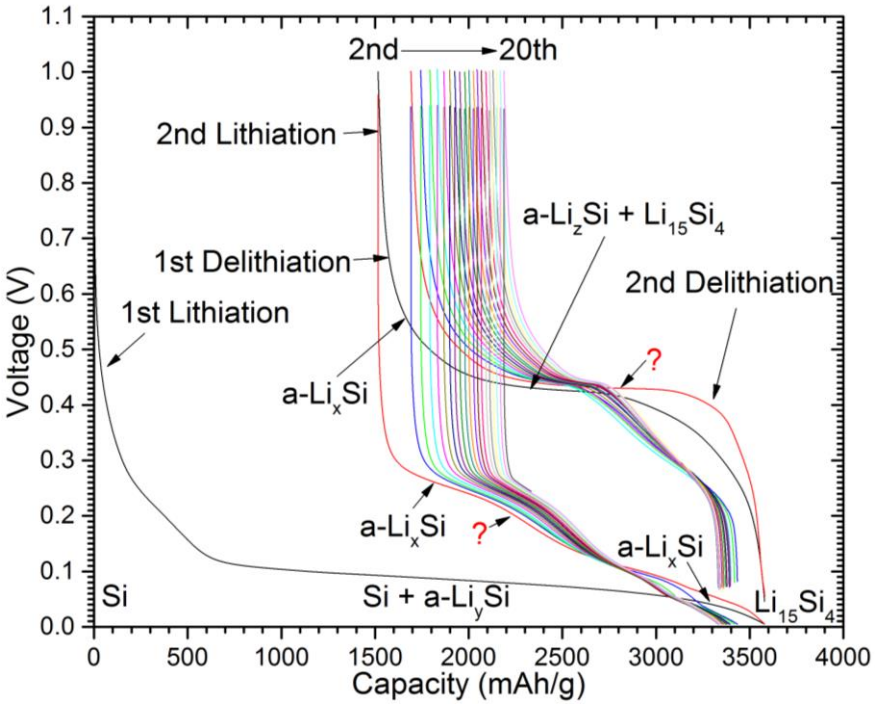

Figure 5.8 Charge/discharge curves of sample S2.

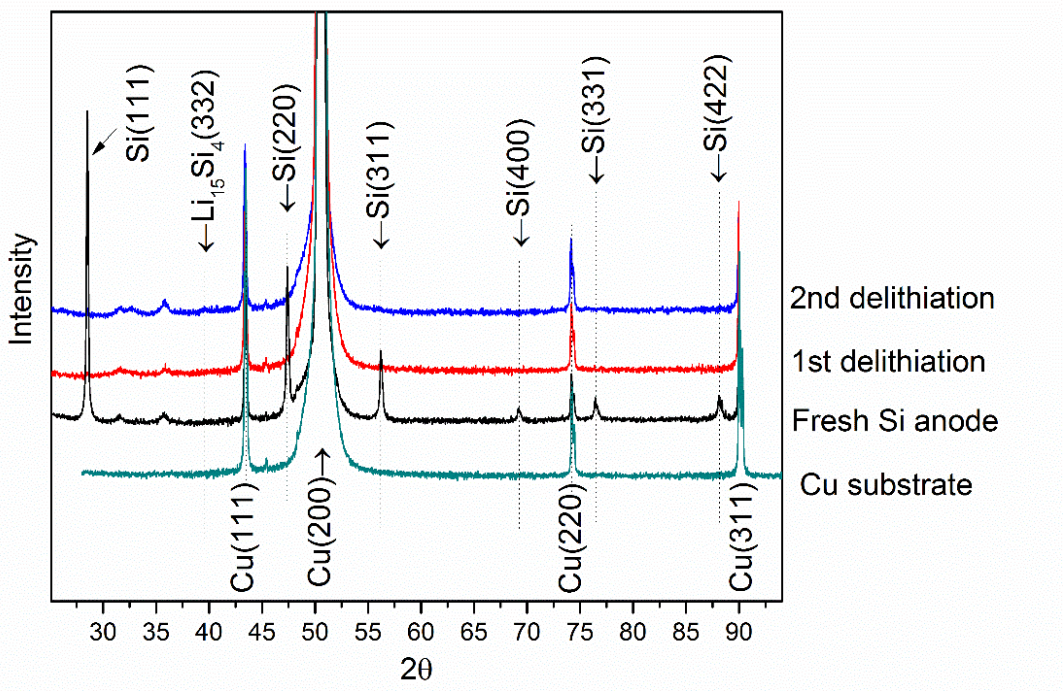

Figure 5.9 XRD patterns of the samples obtained.

5.4 Cell Design for Neutron Diffraction

In order to further study the phase evolutions during the initial cycles of Si anode, in situ neutron diffraction is needed to reveal the unclear phase transitions in the bulk electrode materials/systems that contain crystalline/amorphous structure or phases.

Additionally, the pair distribution function analysis would greatly help to visualize/determine the short range ordering of the amorphous phase upon lithiation or delithiation of Si anode and could help to understand the time-based structure evolution occurring in large, bulk samples that are representative of practical battery electrodes. All these investigations can be facilitated by designing an in situ electrochemical cell which could take advantage of the available neutron diffraction techniques.

Therefore, an in situ electrochemical cell, which can also be used for the study of other battery materials, was designed and fabricated. The assembled cell and the schematic drawing are shown in Figure 5.10. In this design, a cylindrical vanadium can, which have very low coherent scattering cross-section (0.0184 barns) and relatively low incoherent scattering cross-section (5.08 barns), is used as sample holder as well as the cathode current collector to reduce the background noise. A Swagelok tube fitting, which will not expose to neutron beam, is used for both sealing and mounting purposes. By using this design, one can easily avoid the beam interference caused by the electrical connections and greatly simplify the sample mounting inside a neutron powder diffractometer during phase characterization, especially for the instrument setups at NPDF (Los Alamos National Laboratory), NOMAD (Oak Ridge National Laboratory) and POWGEN (Oak Ridge National Laboratory). The logic of this design can also be adopted by in situ tomographic characterization for mapping the bulk distribution of certain elements as a function of time.

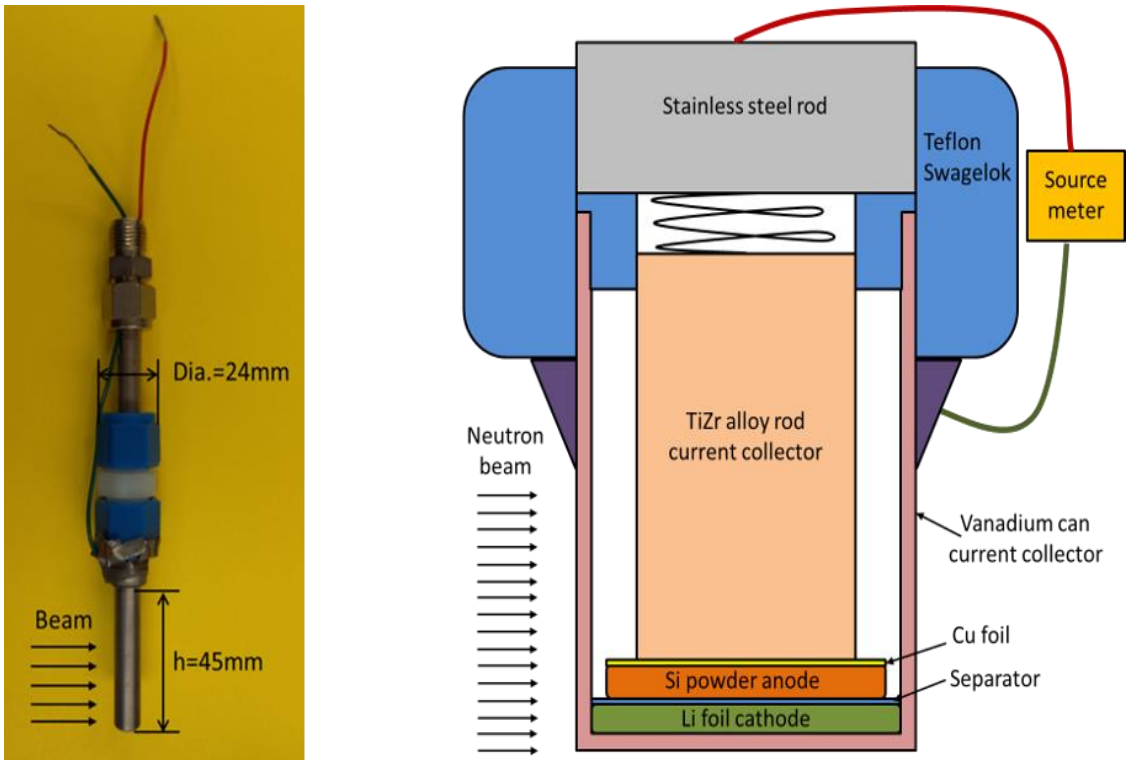

Figure 5.10 Fabricated in situ ND cell and the schematic drawing to show the components.

5.5 Summaries

(1) A nanosized Si electrode with an electrochemically roughened Cu substrate has been prepared and the electrochemical performance has been evaluated.

(2) A Si electrode with mass loading of 0.76 mg/cm^2 shows high initial capacity ~2500 mAh/g and high reversible lithiation/delithiation capacities greater than 1300 mAh/g even after 40 cycles. This is higher than the reported value of most Si composite anodes prepared with the similar approach [16]. The preparation approach used here is considered more economical than other nanofabrication methods.

(3) By reducing the current of initial 2 cycles, it is possible to have more stabilized SEI layers formed. Therefore, the electrochemical performance has been improved dramatically.

(4) An in situ electrochemical cell has been designed and fabricated for neutron diffraction study of phase evolution of Si bulk electrodes.

5.6 References

[1] X.-W. Zhang, P.K. Patil, C. Wang, A.J. Appleby, F.E. Little, D.L. Cocke, Journal of Power Sources, 125 (2004) 206-213.

[2] R.A. Huggins, Lithium alloy anodes, in: Handbook of Battery Materials, Wiley-VCH Verlag GmbH, 2007, pp. 359-381.

[3] J.O. Besenhard, J. Yang, M. Winter, Journal of Power Sources, 68 (1997) 87-90.

[4] C.K. Chan, H. Peng, G. Liu, K. McIlwrath, X.F. Zhang, R.A. Huggins, Y. Cui, Nature Nanotechnology, 3 (2008) 31-35.

[5] T. Song, J. Xia, J.-H. Lee, D.H. Lee, M.-S. Kwon, J.-M. Choi, J. Wu, S.K. Doo, H. Chang, W.I. Park, D.S. Zang, H. Kim, Y. Huang, K.-C. Hwang, J.A. Rogers, U. Paik, Nano Letters, 10 (2010) 1710-1716.

[6] S. Bourderau, T. Brousse, D.M. Schleich, Journal of Power Sources, 81–82 (1999) 233-236.

[7] P. Limthongkul, Y.-I. Jang, N.J. Dudney, Y.-M. Chiang, Journal of Power Sources, 119–121 (2003) 604-609.

[8] P. Limthongkul, Y.-I. Jang, N.J. Dudney, Y.-M. Chiang, Acta Materialia, 51 (2003) 1103-1113.

[9] H. Jung, M. Park, Y.-G. Yoon, G.-B. Kim, S.-K. Joo, Journal of Power Sources, 115 (2003) 346-351.

[10] V. Baranchugov, E. Markevich, E. Pollak, G. Salitra, D. Aurbach, Electrochemistry Communications, 9 (2007) 796-800.

[11] T.L. Kulova, A.M. Skundin, Y.V. Pleskov, E.I. Terukov, O.I. Kon'kov, Journal of Electroanalytical Chemistry, 600 (2007) 217-225.

[12] S. Ohara, J. Suzuki, K. Sekine, T. Takamura, Journal of Power Sources, 136 (2004) 303-306.

[13] N. Dimov, S. Kugino, M. Yoshio, Journal of Power Sources, 136 (2004) 108-114.

[14] H. Li, X. Huang, L. Chen, Z. Wu, Y. Liang, Electrochemical and Solid-State Letters, 2 (1999) 547-549.

[15] N. Hochgatterer, M. Schweiger, S. Koller, P. Raimann, T. Wöhrle, C. Wurm, M. Winter, Electrochemical and Solid-State Letters, 11 (2008) A76-A80.

[16] D. Mazouzi, B. Lestriez, L. Roué, D. Guyomard, Electrochemical and Solid-State Letters, 12 (2009) A215-A218.

[17] M. Gauthier, D. Mazouzi, D. Reyter, B. Lestriez, P. Moreau, D. Guyomard, L. Roué, Energy & Environmental Science, 6 (2013) 2145-2155.

[18] U. Kasavajjula, C. Wang, A.J. Appleby, Journal of Power Sources, 163 (2007) 1003-1039.

[19] J. Li, J.R. Dahn, Journal of the Electrochemical Society, 154 (2007) A156.

[20] M.N. Obrovac, L.J. Krause, Journal of the Electrochemical Society, 154 (2007) A103-A108.

[21] B. Key, M. Morcrette, J.-M. Tarascon, C.P. Grey, Journal of the American Chemical Society, 133 (2011) 503-512.

CHAPTER 6

CONCLUSIONS

(1) Using computed neutron tomography, Li spatial distributions in the bulk Li-Mg alloy electrodes with different depths of delithiation were determined. The variations in Li concentration profiles along the direction of delithiation have been successfully captured. This technique has been proven to be a very powerful tool to noninvasively and quantitatively study bulk distribution of elements that are highly interactive with neutrons, such as Li in Li-ion batteries and H in fuel cells.

(2) An analytical diffusion model for the delithiation of Li-Mg alloy, including the β→α phase transition, has been developed. It considers exactly the β-phase and porous α-phase structure before and after phase transition using appropriate initial and boundary conditions as well as flux-controlled boundary movement. The simulated Li concentration profiles are consistent with the concentration profiles determined from imaging data. The agreement is good within the region where edge effects are not present.

(3) Qualitative Li spatial distribution in the bulk V_2O_5 cathodes, which are charged/discharged under two different c-rates (C/5 and C/10), has been successfully mapped by computed neutron tomography. The attenuation intensity vs. thickness plots obtained from CT data clearly show the effect of applied c-rate on the Li distribution at different locations inside V_2O_5 cathodes. This is in agreement with the established diffusion theory. Thus, computed neutron tomography has been proved to be a very powerful tool to effectively study the effects of charge/discharge rates on Li bulk distribution.

(4) Si electrodes with mass loading of 0.76 g/cm^2 showed high initial capacity ~2500 mAh/g and reversible lithiation/delithiation capacities greater than 1300 mAh/g even after 40 cycles. The effect of mass loading and initial current density on electrochemical performances has been investigated. The preparation approach of Si anode used here is

more economical compared to other nanofabrication methods.

(5) An in situ electrochemical cell has been designed and fabricated for neutron diffraction study of phase evolution of Si bulk electrodes. By using this cell, background noise from the sample holder has been limited by using a cylindrical vanadium can. Also, one can easily avoid the beam interference caused by electrical connections and the can greatly simplify the sample mounting inside the chamber of a neutron powder diffractometer.